Monticellite chemistry as an oxygen barometer for kimberlitic magmas and estimates of primitive kimberlite magma composition

by

Audrey Le Pioufle
B.Sc., Université du Québec à Montréal, 2009

A Thesis Submitted in Partial Fulfillment
of the Requirements for the Degree of

MASTER OF SCIENCE

in the School of Earth and Ocean Sciences

© Audrey Le Pioufle, 2011
University of Victoria

All rights reserved. This thesis may not be reproduced in whole or in part, by photocopy
or other means, without the permission of the author.

Supervisory Committee

Monticellite chemistry as an oxygen barometer for kimberlitic magmas and estimates of primitive kimberlite magma composition

by

Audrey Le Pioufle
B.Sc., Université du Québec à Montréal, 2009

Supervisory Committee

Dr. Dante Canil (School of Earth and Ocean Sciences)
Supervisor

Dr. Laurence Coogan (School of Earth and Ocean Sciences)
Departmental Member

Dr. Stephen Johnston (School of Earth and Ocean Sciences)
Departmental Member

Abstract

Supervisory Committee
Dr. Dante Canil (School of Earth and Ocean Sciences)
Supervisor
Dr. Laurence Coogan (School of Earth and Ocean Sciences)
Departmental Member
Dr. Stephen Johnston (School of Earth and Ocean Sciences)
Departmental Member

The objective of this thesis is to calibrate two oxygen barometers for kimberlite magmas in the system CaO-MgO-Al_2O_3-SiO_2-TiO_2-FeO based on the Fe and V content of monticellite, $CaMgSiO_4$, that may be utilized in cases where oxides in olivine phenocrysts and perovskite are absent from a kimberlite pipe. I first calibrate a new oxygen barometer for kimberlite magmas based on the Fe content of monticellite in equilibrium with kimberlite liquids in experiments at 100kPa from 1230 to 1350°C and at fO_2 from NNO-4.1 to NNO+5.3 (where NNO is the nickel-nickel oxide buffer). The XFe_{Mtc}/XFe_{liq} (where XFe_{Mtc}/XFe_{liq} is the ratio of mole fraction of total Fe in monticellite and Fe in liquid) decreases with increasing fO_2, consistent with only Fe^{2+} entering the monticellite structure. Although the XFe in monticellite varies with temperature and composition, these dependencies are small (±0.03) compared to that with fO_2. The experimental data were fitted by weighted least square regression to the following relationship:

$$\Delta NNO = \frac{\left\{\log\left[0.858(\pm 0.021)\frac{X_{Fe}^{liq}}{X_{Fe}^{Mtc}} - 1\right] - 0.139(\pm 0.022)\right\}}{0.193(\pm 0.004)}$$

(uncertainties at 2σ). I apply this oxygen barometer to natural kimberlites assuming the bulk rock FeO is that of their liquid FeO. Monticellite compositions of five kimberlites from both literature and my own investigations revealed a range in fO_2 from NNO-3.5 to NNO+1.7. I finally use my well-defined monticellite-liquid Kd Fe^{2+}-Mg to derive a range of $Mg/(Mg+Fe^{2+})$ (Mg#) for kimberlite melts of 0.40-0.90. This range in composition is broader than previous estimates of "primary" kimberlites, reflecting the diverse mantle sources and processes that occur during generation and ascent of kimberlites. Second, I calibrate a new oxygen barometer for kimberlite magmas based on the V content of

monticellite in equilibrium with kimberlite liquids doped with 0.5 wt% V_2O_5 at 100kPa at 1280 and 1350°C and at fO_2 from NNO-4.1 to NNO+0.5. The $D_V^{Mtc/liq}$ ($D_V^{Mtc/liq}$ = V (ppm) in monticellite /V (ppm) in liquid) decreases with increasing fO_2. The partitioning data can be fitted to a model consistent with V^{5+} as the dominant species in the melt phase above NNO whereas V^{4+} dominates below those conditions in kimberlitic magmas. The total $D_V^{Mtc/liq}$, which embodies both $D_{V3+}^{Mtc/liq}$ and $D_{V4+}^{Mtc/liq}$, shows a very slight temperature and bulk composition dependence. The experimental data can be fitted by weighted least square regression to the following relationship:

$$\Delta NNO = \frac{\left\{\log\left[0.354(\pm 1.785)\frac{V^{liq}}{V^{Mtc}} - 1\right] - 1.172(\pm 2.302)\right\}}{0.111(\pm 0.071)}$$

(uncertainties at 2σ and V in ppm). In order to apply this oxygen barometer rigorously, the V concentrations of the kimberlite melt coexisting with monticellite need to be constrained. In contrast to the Fe-in-monticellite oxygen barometer for which the concentration of Fe in monticellite was close to that of the whole rock composition, the concentration of V in the bulk rock composition reflects mostly the large accumulation of olivine xenocryts which contain low V concentrations. For that reason, the V-in-monticellite oxygen barometer cannot be applied to natural kimberlites until we find a way to overcome this problem. The vanadium concentrations of kimberlite melts are likely higher than the V concentrations of the whole rock compositions leading to underestimated fO_2 values.

Table of Contents

Supervisory Committee ..... **ii**

Abstract ..... **iii**

Table of Contents ..... **v**

List of Tables ..... **viii**

List of Figures ..... **ix**

List of Appendices ..... **xiii**

Acknowledgments ..... **xiv**

Chapter 1 Introduction **1**

1.1 Mantle oxygen 1

1.2 Kimberlites 2

1.3 Primary magma composition 6

1.4 Kimberlite, fO_2 and diamond oxidation 10

1.5 Thesis Objectives 11

Chapter 2 Iron in monticellite as an oxygen barometer for kimberlite magmas and estimates for primitive magma compositions **14**

2.1 Introduction 14

2.2 Methods 16

2.2.1 Starting materials 16

2.2.2 Experiments 17

2.2.3 Analytical methods 21

2.3 Results 23

2.3.1 Phase equilibria 23

2.3.2 Equilibrium 24

2.3.3 Effect of fO_2, T and bulk composition on XFe of monticellite and liquid and monticellite-melt Kd Fe^{2+}-Mg 28

2.4 Discussion 29

2.4.1 Influence of fO_2 on Fe in Monticellite and Liquid 29

2.5 Application of the Fe-in-monticellite oxybarometer to natural kimberlites 36

2.5.1 Monticellite compositions compiled from the literature 37

2.5.2 Monticellite compositions from detailed study 40

2.5.2.1 Lac De Gras kimberlites 41

2.5.2.2 Somerset Island kimberlite 41

2.6 Using monticellite to estimate kimberlite liquid compositions 46

2.7 Conclusions 58

Chapter 3 Partitioning of Vanadium between monticellite and liquid 62

3.1 Introduction 62

3.2 Methods 64

3.2.1 Analytical methods 64

3.3 Results 65

3.4 Discussion 66

3.4.1 V^{5+} species in the melt phase 66

3.4.2 V Substitution Mechanism in Monticellite 71

3.4.3 Influence of fO_2, T and bulk composition on the vanadium partitioning between monticellite and liquid 76

3.5 Calibration of an oxybarometer for kimberlite magmas 78

Chapter 4 Summary and further work 82

4.1 Fe-in-monticellite oxybarometer 82

4.2 Applications 82

4.3 Kimberlite primitive magma composition 83

4.4 V-in-monticellite oxybarometer 85

4.5 Further work 85

Bibliography 88

Appendix A ..... attached CD

Appendix B ..... attached CD

Appendix C ..... attached CD

List of Tables

Table 2.1. Starting compositions for experiments (wt%) from electron microprobe analyses (EMPA) 19

Table 2.2. Experimental run conditions and phase assemblages 25

Table 2.3. Comparison between the Fe-in-perovskite oxygen barometer (Bellis & Canil, 2007) and the Fe-in-monticellite oxygen barometer for monticellites and perovskites compiled from the literature[c] and from selected kimberlite thin sections[d] 44

Table 2.4. Chemical analyses of monticellites (wt%) and fO_2's calculated..... 47

Table 2.5. Chemical analyses of perovskites (wt%), cations units and fO_2's calculated 54

Table 2.6. Mg# of kimberlite melts calculated from monticellite compositions for different monticellite-melt Kd Fe^{2+}-Mg..... 60

Table 3.1. Parameters obtained by fitting the V partitioning between monticellite and liquid data to Mallmann & O'Neill's equation 15 (2009). 72

Table 3.2. Evaluation of V^{5+} species concentrations in the melt relative to V^{3+} and V^{4+} species in function of the fO_2 from the equilibrium constant, K'_{hom}, derived from Mallmann & O'Neill's regressions for each redox equation. 73

List of Figures

Figure 1.1. Kimberlite'model (right side) after Kjarsgaard (2007). The old terminology (left side) is from Mitchell (1986). 7

Figure 1.2. Estimates of the fO_2 of Kimberlites from the Fe-in-Perovskite (Prv) and olivine-spinel (Ol-Sp) oxygen barometers (Bellis & Canil, 2007; Fedortchouk & Canil, 2004) along with the estimates of the fO_2 of MORB's, OIB's, IAB's (Carmichael, 1991; Christie et al., 1986; Cottrell & Kelley, 2011; Lee et al., 2003; Mallmann & O'Neill, 2009) and cratonic peridotites (McCammon & Kopylova, 2004; Woodland & Koch, 2003). 13

Figure 2.1. Ternary plot showing starting materials (mol%) derived from a worldwide kimberlite database. Fo_{100} was subtracted from the average worldwide kimberlite composition to account for the xenolithic olivine (dash line). Worldwide kimberlites database was compiled in another study (cf., Bellis & Canil, 2007). Cpx= Diopside (White circle); Opx= Orthopyroxene (White rhomb); Fo_{100}= Pure forsterite (White triangle); Mtc= Monticellite (White square). 18

Figure 2.2. Experimental conditions relative to different buffers: QIF (Quartz-Iron-Fayalite); IW (Iron-Wüstite); WM (Wustite-Magnetite); FMQ (Fayalite-Magnetite-Quartz); NNO (Nickel-Nickel Oxide); MH (Magnetite-Hematite) from Frost, 1991. 20

Figure 2.3. Plate detector back-scattered electron (PDBSE) image of a run product (WC3) at 1280°C and NNO-1.2. Prv=Perovskite, Ol=Olivine, Ak=Akermanite, Mtc=Monticellite, Liq=Liquid. 27

Figure 2.4. Time series experiments conducted on WC3, WC and Mon3 compositions at 1280°C and NNO-1.2. XFe_{Mtc} is constant after 12 hours, suggesting that equilibrium is possibly achieved. The converging Fe^{2+}-Mg partitioning coefficient between monticellite and liquid suggests that equilibrium is truly attained after 24 hours. XFe_{Mtc}=molar Fe/(Fe+Ca+Mg). Error bars are ± 1σ. 31

Figure 2.5. Iron oxidation as a function of fO_2 in coexisting liquids at 1350°C, 1325°C, 1300°C, 1280°C and 1230°C calculated using Kress & Carmichael's equation (1988). . 32

Figure 2.6. XFe_{Mtc} as a function of fO_2 expressed relative to the NNO buffer for all compositions at all temperatures. (ΔNNO= fO_2 of experiment-fO_2 of the NNO buffer at the same T). Error bars are ± 1 σ. When not visible, error bar is smaller than the symbol. 33

Figure 2.7. Dependence of XFe_{Mtc} upon temperature at NNO-3.0. Error bars are ± 1 σ. 34

Figure 2.8. a) Covariation of monticellite-liquid Kd Fe^{2+}-Mg and the mole SiO_2 of liquid showing the decreasing trend of the $mSiO_2$ of liquid with the decreasing Fe^{2+}-Mg partitioning coefficient in MON1 and MON3 b) Fe^{2+}-Mg partitioning coefficient between monticellite and coexisting liquid in function of the fO_2 expressed relative to the NNO buffer. Note the decreasing trend of the Fe^{2+}-Mg partitioning coefficient with fO_2 in MON1 and MON3. Error bars are ± 1 σ. 35

Figure 2.9. Covariation between $D_{Fe}^{Mtc/liq}$ and fO_2 relative to the nickel-nickel oxide buffer (ΔNNO= fO_2 of experiment- fO_2 of the NNO buffer at the same T) from Frost (1991). Trend line fitted using equation (2) in text: ΔNNO= {log [0.858*XFe_{liq}/XFe_{Mtc}-1]-0.139}/0.193. Error bars are ± 1 σ. Regression coefficients b, c and d are respectively 0.193 ± 0.004, 0.139 ± 0.022 and 0.858 ± 0.021 and R^2 is 0.973. $D_{Fe}^{Mtc/liq}$ is expressed as XFe_{Mtc}/XFe_{liq} where XFe is the mole fraction of total Fe/Σcations. 38

Figure 2.10. fO_2's calculated with my Fe oxygen barometer vs fO_2's of experiments relative to the NNO buffer. The 1:1 line is shown along with two dash lines constraining ± 1 log fO_2 unit for reference. 39

Figure 2.11. a) XFe of monticellite, b) XFe of the bulk composition and c) fO_2's (relative to the NNO buffer) calculated with equation 3 for monticellite compositions compiled from the literature. Error bars are ± 1 σ. Note that because of the complex zoning in Elwin Bay monticellites, the Fe-in-monticellite oxygen barometer cannot be applied to this kimberlite and gives spurious and non reliable results. 43

Figure 2.12. Plate-detector back-scattered images (PDBSE) of a) Abundant subhedral and anhedral monticellites (along with Fe-Ti-Mg oxides) set in a fine-grained matrix,

Elwin Bay kimberlite. b) Subhedral and anhedral monticellites (along with olivine macrocrysts) set in a fine-grained matrix, Aaron kimberlite. Scale bar represents 800 µm in both images. Mtc= Monticellite; Ox= Fe-Ti-Mg Oxides; Ol= Olivine. 52

Figure 2.13. a) XFe of monticellite, b) XFe of the bulk composition and c) fO_2's (relative to the NNO buffer) calculated with equation 3 for monticellite data from my detail analysis of selected kimberlites. Error bars are ± 1 σ. Note that because of the complex zoning in Elwin Bay monticellites, the Fe-in-monticellite oxygen barometer cannot be applied to this kimberlite and gives spurious and non reliable results. 53

Figure 2.14. a), b) and c) Mg# of kimberlite melts ($Mg/(Mg+Fe^{2+})$) from monticellite compositions for all kimberlite pipes studied calculated with a monticellite-melt Kd Fe^{2+}-Mg of 0.40, 0.30 and 0.20 respectively. Note the wide range of Mg# liquid of kimberlites. The Mg# of kimberlite melts have been averaged for each kimberlite pipe, including rims and cores (Elwin Bay and Wajrakarur pipes). Sources of data for the Mg# of the melts (Mg/(Mg+total Fe)) from the Lac de Gras, Jericho, South African Gp 1, Kimberley, Udachnaya-E and Majuagaa kimberlites: Kjarsgaard et al., 2009; Kopylova et al., 2007; Becker a& Le Roex, 2006; Le Roex et al., 2003; Kamenetsky et al., 2009; Nielsen & Sand, 2008 respectively. 61

Figure 3.1. Comparison between V concentrations in monticellite by LA-ICP-MS and EMP. Note the large error bars on the EMPA. Equation for the linear regression is: $V_{ICP}=0.982(0.081)*V_{EMP}+42.31(6.58)$. $R^2=0.96$. Error bars are ± 1σ. 67

Figure 3.2. Time series experiments on WC and WC3 compositions with respect to the V in monticellite. Equilibrium is suggested after 24 hours according to the $D_V^{Mtc/liq}$. Error bars are ± 1σ. 68

Figure 3.3. Vanadium concentrations in glasses in equilibrium with monticellite. Constant concentrations are observable in MON3 and WC3 (1280°C) compositions but not in WC and Mon1 (at 1280°C and 1350°C respectively). Error bars are ± 1σ. 69

Figure 3.4. Vanadium concentrations in monticellite in function of fO_2 relative to the NNO (ΔNNO = log fO_2 of experiments- log fO_2 of the NNO buffer). Error bars are ± 1σ. 70

Figure 3.5. Non-linear least square regression of all data including NNO+5.0 at 1280°C and 1350°C in function of the log fO_2. The equation of the regression can be found in Mallmann & O'Neill (2009) assuming only V^{3+}, V^{4+} and V^{5+} in the melt phase:..... 74

Figure 3.6. Substitution mechanism in monticellite. a) Correlation between Mg^{2+} and V^{3+} cations (and with fO_2) b) Positive correlation between Fe^{2+} and V^{3+} cations in monticellite c) Tetrahedral substitution of V in WC3, WC and Mon3 only..... 75

Figure 3.7. Variation of $D_V^{Mtc/liq}$ with fO_2 (expressed relative to the Nickel-Nickel Oxide buffer at the temperature of interest). The correlation between $D_V^{Mtc/liq}$ and fO_2 is fitted by weighted least squares linear regression (equation 7). Regression coefficients c, b and d are respectively 0.354± 1.785, 0.111 ± 0.071 and 1.172 ± 2.302. R^2 is 0.75. Error bars are ± 1σ. 80

Figure 3.8. fO_2's calculated from the V-in-monticellite oxygen barometer vs fO_2's of experiments (relative to the NNO buffer). Accuracy of the new oxybarometer is ± 1 log fO_2 unit. 81

Figure 4.1. Estimates of fO_2 of kimberlites from the Fe-in-Perovskite (Prv), Fe-in-Monticellite (Mtc) and Olivine-Spinel (Ol-Sp) oxygen barometers (Bellis & Canil, 2007; this study; Fedortchouk & Canil, 2004) along with other estimates of MORB's, OIB's, IAB's, lamprophyres, andesites (Carmichael, 1991; Christie et al., 1986; Cottrell & Kelley, 2011; Lee et al., 2003; Mallmann & O'Neill, 2009) and cratonic peridotites (McCammon & Kopylova, 2004; Woodland & Koch, 2003). 84

List of Appendices

Appendix A Electron microprobe analyses of liquidus phases and their coexisting glass (wt%) with STDEV (1σ) and run conditions ..... attached CD

Appendix B Monticellite kimberlite compositions ..... attached CD

Appendix C Selected kimberlite whole rock compositions ..... attached CD

Acknowledgments

I would like to first thank my supervisor Dante Canil for his patience and guidance throughout my studies. I also want to thank M. Raudsepp and S. Kuehner, and J. Spence for assistance with the EMP and LA-ICP-MS analyses, respectively. This research was funded by an NSERC of Canada and FQRNT Scholarship to me and an NSERC of Canada Discovery Grant to D.C.

Chapter 1
Introduction

1.1 Mantle oxygen

During the early history of the Earth, the separation of the core and the silicate mantle was the starting point to the chemical differentiation of the planet. Many explanations for the early oxidation state of the mantle during core-mantle segregation have been proposed (e.g., Wood et al., 2009; Galimov, 2005), but the actual mechanism remains obscure. Further differentiation of the mantle, for example, by melt extraction, degassing and subduction, has led to substantial spatial and secular heterogeneities in its composition, including its oxygen content.

The mantle constitutes 80% of the volume and 65% of the mass of the Earth (Bennett, 2003). Understanding processes in the mantle allows constraints on different variables controlling the generation and differentiation of mantle-derived magmas. Amongst the intensive variables relevant to the mantle, the oxygen fugacity is a key variable to describe the origin of different mantle-derived rocks. Mantle redox influences the partitioning of heterovalent elements (e.g., Fe, V, Cr, Eu) between minerals and liquids which in turn affects the products of mantle melting and chemical differentiation of magmas (Borisov et al., 1987; Cicconi et al., 2010; Kress & Carmichael, 1988; Roeder & Reynolds, 1991). Volatiles such as C, H and S may exhibit different oxidation states (CH_4, CO, CO_2; H_2, H_2O, S_2, SO_2) according to the fO_2 in the mantle.

The exact control of the fO_2 in the mantle is unclear. The fO_2 of the mantle may be given by the bulk composition (at T and P of interest) and the buffering capacity of equilibria assuming a system closed to oxygen. Canil et al. (1994) stated, however, that

the upper mantle is not likely buffered by any particular buffer systems, e.g., C, H, S or Fe^{3+}/Fe^{2+}. Subduction processes and metasomatism are thought to affect the fO_2 of the mantle (Ballhaus, 1993; Höfer et al., 2009; Lee et al., 2003; Mattioli et al., 1989; McCammon et al., 2004; Parkinson & Arculus, 1999). The fO_2 is heterogeneous in the Earth's interior and reflects a long evolution since the formation of the mantle (Ballhaus, 1993; Woodland & Koch, 2003).

Mantle xenoliths and igneous rocks, such as mid-ocean ridge basalts (MORB's), ocean island basalts (OIB's) and kimberlites serve as probes of the chemical reservoirs and their temporal and spatial evolution in the mantle. The fO_2 is known to vary with tectonic setting with IAB's (Island Arc Basalts) being more oxidized than MORB's (Mid Ocean Ridge Basalts) and OIB's (Ocean Island Basalts), at least from the Fe^{2+}/Fe^{3+} ratio (Ballhaus, 1993). Recently, studies on the V abundances showed that the fO_2 of IAB's is not distinguishable from that of MORB's and OIB's (Lee et al., 2005; Mallmann & O'Neill, 2009). The present upper mantle fO_2 is believed to be near the FMQ, Fayalite-Magnetite-Quartz, buffer (or ~NNO-1, where NNO is the Nickel-Nickel Oxide buffer) (Ballhaus, 1993; Cottrell & Kelley, 2011). A good understanding of the processes that govern the redox state of the mantle and mantle-derived melts permits an understanding of the evolution of the mantle through time.

1.2 Kimberlites

Kimberlites are rare ultramafic igneous rocks forming pipes in the upper crust. Kimberlites are unique magmas in several aspects: 1) they do not preserve glass as most volcanic rocks do; 2) they are known to form at great depth in the asthenosphere (>150km) and 3) they carry xenocrystic diamonds. Kimberlite magmatism is widespread

over geological time from Proterozoic (>1600Ma, Donnelly et al., 2011) to Eocene-Oligocene ages (52-32 Ma including Mwadui and Lac de Gras kimberlites, Davis & Kjarsgaard, 1997; Heaman et al., 2003; Kjarsgaard, 2007 and Kambeli and Msipashi kimberlites, Batumike et al., 2008), and mostly spatially associated either with Archaean and Palaeoproterozoic cratonic lithosphere and/or basement fractures and crustal lineaments.

Several nomenclatures and terminologies have been elaborated and have either a descriptive and/or genetic connotation. The kimberlite model was first based on the South African kimberlites (Clement et al., 1984; Mitchell, 1986) but further modified by the discoveries of new pipes in North America, South America, China, Russia, Australia and Greenland. Mitchell (1986) defines kimberlites as composed of three different genetic facies: hypabyssal, diatreme and crater facies. Hypabyssal kimberlite is defined as a coherent or magmatic kimberlite, made of olivine macrocrysts set in a fine-grained groundmass, forming irregular bodies in the root zone whereas diatreme and crater facies are defined as volcaniclastic rocks (pyroclastic/tuffisitic and epiclastic/resedimented kimberlites respectively). Volcaniclastic rocks are commonly made of lapilli, olivine phenocrysts and macrocrysts, groundmass minerals, crustal and mantle xenocrysts, megacryst suite minerals and secondary minerals (Mitchell, 1986; Sparks et al., 2009). Additionally, diopside and phlogopite microlites along with serpentine minerals, oxides, sulphides, carbonates and clay minerals are found in the volcaniclastic section and are thought to be derived from magmatic gases, hydrothermal activity and weathering although their origin remains obscure (Sparks et al., 2009). Kimberlites have also been separated into two groups: Group I (olivine-rich) and Group II (micaceous) kimberlites

(cf., Becker & Le Roex, 2006) according to their mineralogy and origin. Kimberlites are classified in three class types: I, II and III. Class I comprises 3 zones which are the hypabyssal, diatreme and crater facies (commonly plus a transitional facies) whereas Class II comprises the hypabyssal and crater-facies (pipe filled with volcaniclastic rocks, cf., Skinner and Marsh, 2004). Class III is characterized mainly by the presence of only pipes with re-sedimented volcaniclastic kimberlites. Kjarsgaard (2007) refined Mitchell's (1986) nomenclature and simplified it by grouping the different rock types in two non-genetic classes: hypabyssal kimberlite (non-fragmental rocks) and volcaniclastic kimberlite (fragmental rocks) because of the ambiguity in the origin of diverse kimberlite rock types (Figure 1.1). His model is based on two different kimberlites, the upper part of the Orapa kimberlite in Botswana and the lower part of a Kimberley kimberlite pipe. Recently, Cas et al. (2008a, 2008b, 2009) highlighted the terminology problems: the mineralogical, genetic and textural schemes, the uniqueness of the nomenclature in comparison to classical volcanology, and the false expectation of the location of a specific facies. Cas et al. produced a pocket guide based on a descriptive classification followed by a genetic classification of kimberlites. Moreover, they propose a new classification of kimberlites based on modern volcanology and sedimentology in order to restrain the colorful terminology of kimberlites and to reconcile kimberlite terminology with mainstream volcanology. Scott Smith et al. (2008) developed and adapted the nomenclature of Cas et al. (2008a), with a special focus on kimberlite exploration and mining, introducing new terms (e.g., Wesselton–type volcaniclastic kimberlite) that render the terminology of kimberlites more confusing and challenging. The kimberlite

nomenclature remains complex and for that reason classification of kimberlite according to one particular model or belief is unsettling.

The process to generate kimberlite magmas is not well-understood. A kimberlite eruption has never been witnessed and impedes the understanding of the formation of kimberlites. Kavanagh & Sparks (2009) elaborated a thermodynamical model during kimberlite ascent to model the temperature variations of kimberlite magmas from depth of 200km and 400km. Their results are consistent with geothermometric studies (1030-1170°C) and showed that the adiabatic expansion, degassing and lithospheric contamination can be responsible for its cooling although the latent heat during crystallization raises the temperature of the magma with decreasing pressure. They also concluded that the composition of the magma is not affected by assimilation of olivine. To model a kimberlite eruption, Sparks et al. (2006) proposed a four-stage model in which magma velocities and supply rates are given. Their model suggests that the ascent of the magma occurs along fissures followed by an explosive eruption near the surface due to overpressure, creating the pipe itself and the crater facies. According to their model, kimberlite forms from the top downwards. The explosive and erosive stage II is then followed by a fluidised bed of volcaniclasts which will form the massive volcaniclastic kimberlite subsequently altered by hydrothermal activity. Note that whether kimberlites form from the bottom up or the top down is controversial. Other studies on kimberlite formation have been undertaken (e.g., the phreatomagmatic model, cf., Lorenz, 1975; Kurszlaukis & Lorenz, 2008) but are not be discussed here because the kimberlite formation is not the main focus of this thesis.

Kimberlite mineralogy is complex, varying according to the facies. Kimberlite is an inequigranular rock containing a variety of xenoliths and xenocrysts. Olivine is the primary phase in kimberlites, present as xenocrysts, macrocrysts and phenocrysts. Other xenocrysts found in kimberlites are: Cr-pyrope garnet or almandine-pyrope garnet, ilmenite, chromian spinels, Cr-diopside, bronzite, amphibole, phlogopite and/or omphacite depending on the nature of the mantle through which kimberlites ascended (Kjarsgaard, 2007). Olivine, spinel and phlogopite are found as microphenocrysts and phenocrysts. Diamonds are present in kimberlites but only as a rare constituent and are thought to be mantle-derived xenocrysts (Clement et al., 1984; Patterson et al., 2009; Stachel & Harris, 2008). The groundmass of kimberlites is generally olivine, spinels, perovskite, monticellite, phlogopite-kinoshitalite, carbonates (calcite and dolomite), and apatite although these minerals are rarely found all together in a same kimberlite (Kjarsgaard, 2007; Mitchell, 1986). Common deuteric alterations are serpentine, calcite, diopside, and magnetite and replace macrocrysts and groundmass phases (Kjarsgaard, 2007). The origin of serpentine and carbonate, as either magmatic or secondary (from metasomatism or meteoritic water) minerals, in kimberlites are controversial (Sparks et al., 2009). The lack of a consensus on the definition of kimberlite olivine impedes the classification of different type of olivines in kimberlites (Arndt et al., 2010) and thus prevents the determination of their origin and a rigorous application of the use of olivine to unveil the composition of the primitive kimberlite magma.

1.3 Primary magma composition

The large number of xenocrysts, the loss of magmatic volatiles during crystallization and emplacement, the lack of constraints on the origin of H_2O (magmatic,

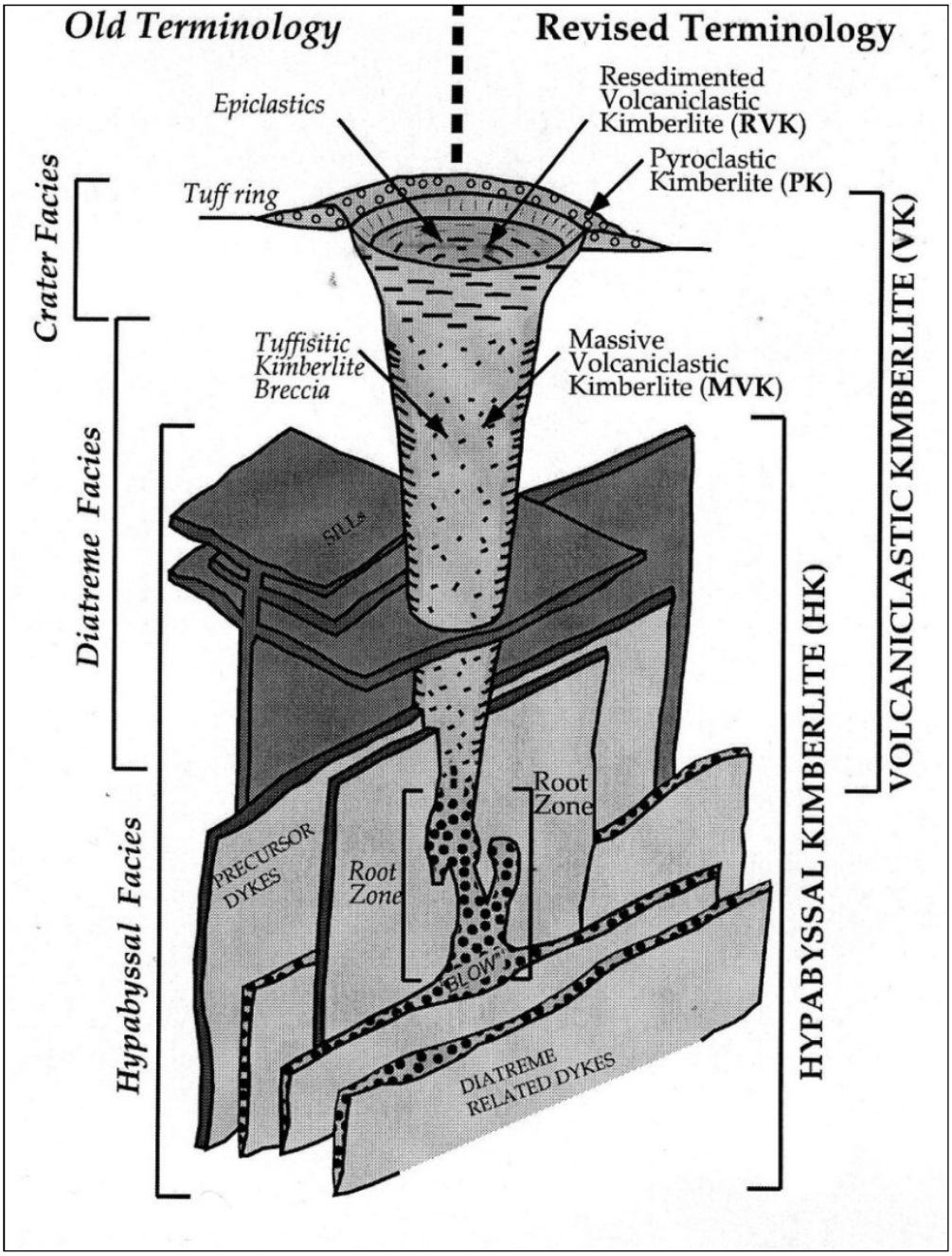

Figure 1.1. Kimberlite'model (right side) after Kjarsgaard (2007). The old terminology (left side) is from Mitchell (1986).

metasomatic or meteoritic), the lack of glass and the extensive alteration, make the study of kimberlite challenging, and hinder our ability to determine the "primary" composition of kimberlite melts. Several studies have, however, attempted to determine the "primary" kimberlite magma composition by a variety of methods.

One way to determine the primitive kimberlite composition is to analyze aphanitic kimberlites (Kopylova et al., 2007; Price et al., 2000). Kopylova et al. (2007) have analyzed the high Ca Jericho aphanitic kimberlite margin using a chemical counting point technique, which consists in the electron microprobe (EMP) analysis of the groundmass bulk composition covering a grid of 100 points, and estimated the Mg# (Mg/(Mg+total Fe)) of melt to be 0.86. Whether high Ca aphanitic kimberlites are either evolved or primitive rocks is debated. Mitchell (2008) stated that such kimberlites cannot trace the primitive kimberlite composition because of extensive differentiation of the rock, citing the work of Edgar and Charbonneau (1993). By subtracting different amounts of xenolithic olivine and/or peridotite from the kimberlite whole rock analysis from Lac de Gras kimberlites, Kjarsgaard et al. (2009) estimated the primitive composition of kimberlites and obtained a Mg# of 0.87. Another technique to calculate the primitive magma composition relies on finding intermediate compositions between the least crustally contaminated and the least mantle contaminated samples. In doing so, Le Roex et al. (2003) and Becker & Le Roex (2006) calculated a Mg# of 0.84-0.86 for the South African kimberlites similar to the estimate of Harris et al. (2004) of 0.84 for the Uintjiesberg kimberlite. Nielsen & Sand (2008) reported a Mg# of 0.80, using a technique similar to that of Kjarsgaard et al. (2009), for the Majuagaa kimberlite in Greenland.

Experimental studies have produced kimberlite magma compositions in melting experiments of mantle peridotites at high pressure and in the presence of H_2O and CO_2. Ellis & Wyllie (1979), in a study on phase diagrams and melting of a peridotite at pressure above 2GPa, concluded that phlogopite and CO_2 (dolomite or magnesite) were required in mantle peridotite to produce a kimberlite because increasing the amount of dissolved CO_2 in a liquid produces silica undersaturated melts. Eggler and Wendlandt (1979) suggested that kimberlites cannot be formed at pressure below 3GPa because the melt would not be in equilibrium with the mantle and thus cannot be primary. This has also been proved by Gudfinnsson & Presnall (2005) who stated that below 2-3GPa the composition of the liquid would shift to nephelinites and melilitites rather than carbonatites and kimberlites and elevated pressure such as 5GPa or higher are required to produce kimberlitic melts. Canil & Scarfe (1990) refined the previous theoretical work by Wyllie's group with experiments at high pressures (4-12 GPa) and suggested that kimberlites are derived from a magnesite peridotite at pressure between 5 and 7 GPa. Primary kimberlite magmas are thought to be derived from a carbonated peridotite from which the first liquid near the solidus would be carbonatitic in composition and with increasing melting would shift towards a kimberlitic composition (Dalton & Presnall, 1998; Gudfinnsson & Presnall, 2005).

Despite all the studies on the "primary" kimberlite magma composition (which is defined as the composition of a magma resulting from the partial melting of the mantle contrarily to the primitive kimberlite magma composition which is defined as the composition of a magma that is not evolved but not necessarily primary), the high Mg# calculated for "primary" kimberlite using natural aphanitic rocks is remarkable because

such melts are not likely to be in equilibrium with typical mantle olivine (Fo_{90}) during the partial melting of a garnet lherzolite, assuming an olivine-melt Kd Fe^{2+}-Mg of 0.35. This makes for a conundrum between "primary" melts deduced from natural rocks, when compared with those produced in experiments.

1.4 Kimberlite, fO_2 and diamond oxidation

Because of their high mantle xenolith content, kimberlites provide useful information on the lithospheric mantle and many studies have focused on that particular aspect of kimberlites. Kimberlites, however, are the main host-rock of diamonds and the fO_2 could have a great impact on their preservation. The fO_2 of kimberlite magmas is of prime importance because of its relationship with the diamond grade and quality of diamonds of a pipe. Natural diamonds exhibit a range of etching and resorption features which have been related to the fO_2, temperature as well as H_2O and CO_2 solubility in melts (Arima & Kozai, 2008; Fedortchouk et al., 2005, 2007; Harris & Vance, 1974; Kozai & Arima, 2005; Sonin et al., 2006). Fedortchouk et al. (2007) demonstrated that the resorption features of diamonds were correlated to the composition of the fluid, whether H_2O-rich and/or CO_2-rich interacting with diamonds. These authors also found that a fluid-undersaturated kimberlite melt would produce graphitization on the diamond surfaces, as well as sharp features and irregular cavities. The etching rate and resorption of diamonds decrease with decreasing fO_2 (Fedortchouk et al., 2005; Sonin et al., 2006). In a study on diamond dissolution forms in Lac de Gras kimberlites, Fedortchouk et al. (2005) showed that the resorbed diamonds found in the Lac de Gras kimberlite field were correlated with oxidizing conditions suggesting that there is indeed a strong relationship between the fO_2 and the diamond grade of kimberlite. A variety of diamond colors has

been observed in kimberlites. Fedortchouk et al. (2005) noticed that, although the degree of resorption is not correlated to the diamond color, brown diamonds show more etch features than the other diamond groups. Finally, Fedortchouk et al. (2009) developed an empirical relationship relating fO_2, T and the diamond oxidation rate, by Ln V = 0.57* log fO_2 +T_{Term} where V is the diamond oxidation rate, allowing one to evaluate the possible oxidation rate of diamonds contained in a given kimberlite pipe of known fO_2 and temperature and T_{Term} is the temperature of the magma.

1.5 Thesis Objectives

The fO_2 of assemblages in many rocks can be easily calculated from redox reactions between components in constituent minerals, for example:

$$3Fe_2SiO_4 + O_2 = 2Fe_3O_4 + 3SiO_2 \quad (1)$$

$$6Fe_2SiO_4 + O_2 = 3Fe_2Si_2O_6 + 2Fe_3O_4 \quad (2)$$

$$2Fe_3Fe^{3+}{}_2Si_3O_{12} = 4Fe_2SiO_4 + 2FeSiO_3 + O_2 \quad (3)$$

$$Fe_2SiO_4 = 2Fe + SiO_2 + O_2 \quad (4)$$

These and similar reactions describe a redox change typically between Fe^{2+} and Fe^{3+} (except equation 4) in phases (Ballhaus et al., 1991; Frost & McCammon, 2008; O'Neill & Wall, 1987; Wood, 1990). The relative abundance of Fe^{2+} and Fe^{3+} in igneous glasses can also be used to estimate the magma's fO_2 where natural glass is preserved (Kilinc et al., 1983; Kress & Carmichael, 1988; Sack et al., 1980). Unfortunately these and several other redox estimates are not applicable to kimberlites because of the lack of suitable igneous (i.e., cognate) minerals in equilibrium or of preserved glass. Fedortchouk & Canil (2004) calculated reduced fO_2's between NNO-2.0 and NNO-3.0 (where NNO is the nickel-nickel oxide buffer) for kimberlite magmas from Lac De Gras using the

olivine-spinel oxygen barometer for olivine – chromite phenocryst pairs (Ballhaus et al., 1991). The accuracy of their results is suspect, however, because of the absence of orthopyroxene and the assumption of the silica activity of kimberlites. Following that work, an oxygen barometer was calibrated for kimberlite magmas based on the Fe content of perovskite (Bellis & Canil, 2007; Canil & Bellis, 2007) and revealed a wide range of fO_2 of kimberlites from NNO-5 to NNO+6 (Figure 1.2). Nonetheless, not all kimberlites contain perovskite and its multitude of textures can be complicated to interpret.

This study aims to constrain the fO_2 of kimberlites that lack fresh olivine and perovskite. To do so, this study focuses on monticellite, $CaMgSiO_4$, which forms euhedral to subhedral crystals (0.005 to 0.08mm) in the groundmass of kimberlites, crystallizing prior to calcite and serpentine (Mitchell, 1986). Monticellite is an olivine group mineral from the kirschteinite–monticellite series and may form a solid solution with kirschteinite ($CaFeSiO_4$) and forsterite (Mg_2SiO_4) (Warner & Luth, 1973).

This thesis has two objectives: 1) to develop two empirical oxygen barometers based on the Fe and V content of monticellite to constrain the fO_2 of kimberlite magmas over a range of fO_2 relevant to terrestrial magmas and 2) to estimate primitive kimberlite magma compositions from monticellite compositions. This study is the first attempt to characterize the primitive magma composition of kimberlites from an “igneous” mineral composition germane to the kimberlite magma, assuming no alteration in its composition, and will contribute to the knowledge of the origin of kimberlites.

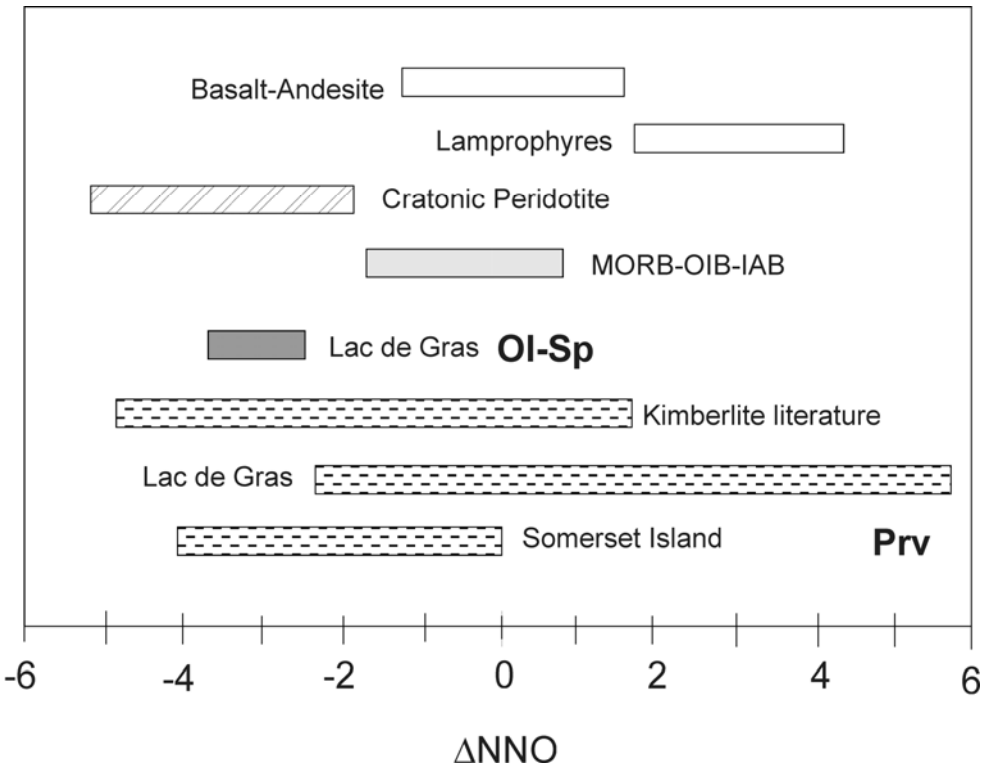

Figure 1.2. Estimates of the fO_2 of Kimberlites from the Fe-in-Perovskite (Prv) and olivine-spinel (Ol-Sp) oxygen barometers (Bellis & Canil, 2007; Fedortchouk & Canil, 2004) along with the estimates of the fO_2 of MORB's, OIB's, IAB's (Carmichael, 1991; Christie et al., 1986; Cottrell & Kelley, 2011; Lee et al., 2003; Mallmann & O'Neill, 2009) and cratonic peridotites (McCammon & Kopylova, 2004; Woodland & Koch, 2003).

Chapter 2
Iron in monticellite as an oxygen barometer for kimberlite magmas and estimates for primitive magma compositions

2.1 Introduction

The fO_2 of magmas shows more variation than any other parameter in igneous rocks (Carmichael, 1991) and plays a major role in the behavior of Fe and other redox sensitive elements in the liquid (Carmichael & Ghiorso, 1986). Decades of study on a range of magmas from basalt to rhyolite have linked fO_2 and the Fe^{2+}-Fe^{3+} partitioning between minerals and melts and their bearing on magmatic differentiation (Fudali, 1965; Kennedy, 1948; Osborn, 1959, 1962; Osborn & Roeder, 1960).

Kimberlite magmas are important because, although they are extremely rare, they are the most deep-seated magmas and the hosts for diamonds. The fO_2 of kimberlites is of interest because it may in part control the quality and presence of diamonds (Fedortchouk & Canil, 2004; Fedortchouk et al., 2005). Although the fO_2 in many igneous rocks can be readily calculated from conventional methods (Kilinc et al., 1983; Kress & Carmichael, 1988; Sack et al., 1980), none of these approaches are usually possible for kimberlites (Bellis & Canil, 2007). Fedortchouk & Canil (2004) estimated the crystallization temperatures and the fO_2 of kimberlite magmas from oxide inclusions in olivine phenocrysts and reported a crystallization range from 1030 to 1170°C at NNO-2 to NNO-3. More recently, Bellis & Canil (2007) studied the partitioning of Fe^{3+} between perovskite and liquid over a range of fO_2 and developed an oxygen barometer for kimberlite magmas. The application of their oxybarometer to natural kimberlites revealed a fO_2 range of many orders of magnitude from NNO-5 to NNO+6, and the

highest known fO_2 conditions for any terrestrial magmas. A possible cause of the oxidized nature of kimberlites is attributed to the presence of deep and oxidized source regions and the carbon-fluid equilibria during the ascent of these carbon-rich magmas (Canil & Bellis, 2007). Nonetheless, not all kimberlites contain perovskite, and fewer contain phenocrysts of fresh olivine with spinel inclusions.

In this chapter I develop an oxygen barometer for kimberlite magmas based on the Fe^{2+} content of monticellite in equilibrium with synthetic kimberlite liquid compositions. Monticellite is a mineral from the kirschteinite–monticellite series ($CaFeSiO_4$-$CaMgSiO_4$) in the olivine quadrilateral. Although olivine is the most common mineral in kimberlites, I focus on monticellite due to the fact that the origin of olivine crystals in kimberlites is dubious (Arndt et al., 2010; Brett et al., 2009; Fedortchouk & Canil, 2004; Patterson et al., 2009) and thus not always suitable for studies on the fO_2 of kimberlitic magmas. Most importantly, monticellite is ubiquitous in kimberlites, constituting up to 80% of the groundmass mineralogy (Mitchell, 1986) and crystallizing at low pressures (< 0.5 GPa) prior to calcite and serpentine (Mitchell, 1986). The wide crystallization range of monticellite and perovskite allows for the examination of the change in kimberlite fO_2 along the liquid line of descent.

Iron is present in terrestrial magmas as Fe^{2+} and Fe^{3+}. In my approach, I assume monticellite accommodates only Fe^{2+} in its structure, based on ^{57}Fe Mössbauer studies of olivine group minerals (Canil & O'Neill, 1996; Dyar, 2003; Pieters et al., 2008; Treiman et al., 2007; Zhang et al., 1999). With increasing fO_2 in kimberlite magmas the redox equilibrium for Fe in the melt:

$$FeO + \tfrac{1}{4} O_2 = FeO_{1.5} \qquad (1)$$

shifts to the right with less Fe^{2+} available in the liquid to partition into monticellite. I thus expect a negative correlation of the Fe^{2+} content of monticellite with the fO_2 of coexisting liquids. I apply my oxygen barometer to natural monticellite compositions compiled from the literature and from selected kimberlites that I have studied in detail. I compare my results, where possible, to a similar oxygen barometer based on the Fe^{3+} content of perovskite (Bellis & Canil, 2007). Furthermore, I refine estimates for possible "primary" kimberlite compositions (Mg# of the primitive melt) based on the monticellite composition and the Fe^{2+}-Mg exchange between monticellite and the coexisting liquid.

2.2 Methods

2.2.1 Starting materials

I prepared several different starting materials (Table 2.1). The MON1 starting material was derived by calculating the average natural kimberlite composition (from a worldwide kimberlite database compiled from the literature (Figure 2.1) and subtracting 40 mol% olivine (Mg_2SiO_4) to account for the xenolithic olivine content of kimberlites. The xenolithic component in natural kimberlites changes Mg and Ca content of the bulk composition, so its removal decreases the Mg and increases the Ca content resulting in: 1) reduction of the mode of olivine and increase of that of liquid at a given temperature, 2) decrease of the crystallization temperature of minerals. I also converted a portion of MgO and SiO_2 into FeO and TiO_2 respectively to add these components in natural kimberlites. The WC starting composition is from previous experiments of Bellis & Canil (2007) and was based on Wesselton aphanitic kimberlites in South Africa, which has a higher Ca and lower Mg content than most kimberlites. Two other starting materials, MON3 and WC3, were synthesized from the glass compositions after > 50% crystallization of MON1 and WC, respectively, in order to increase the amount of liquid

present for better phase identification at lower temperatures (cf., Toplis & Carroll, 1995). In this way, MON3 and WC3 were based on equilibrium crystal fractionation of Mon1 and WC respectively. Natural kimberlites contain between 5 and 20 wt% H_2O and/or CO_2, but I excluded these components from all my starting materials because experiments were done at 100 kPa to accurately control fO_2. Under these experimental conditions, volatiles cannot be maintained in solution. Because all volatiles have been excluded from starting materials, temperatures of crystallization of monticellite are likely higher than in natural kimberlites, estimated to be between 1200 and 700°C (Fedortchouk & Canil, 2004; Kavanagh & Sparks, 2009; Sparks et al., 2009).

Starting materials were synthesized from reagent grade oxides SiO_2, TiO_2, Al_2O_3, Fe_2O_3, MgO, $CaCO_3$ and V_2O_5 which were dried for 24 hours at different temperatures to release the water content (900°C for SiO_2 and MgO, 300°C for $CaCO_3$ and 1000°C for Fe_2O_3 and TiO_2). Reagent oxide mixes were decarbonated in air in a Pt crucible in a box furnace for 2 hours at 900°C, then fused at 1500°C for 24 hours and quenched in water to avoid crystallization. All materials quenched to a glass and were crushed and ground under acetone in an agate mortar to a grain size of 25-50µm.

2.2.2 Experiments

Experiments were performed in gas-mixing vertical tube furnaces over a range of fO_2 from NNO-4.1 to NNO+5.3 at temperature between 1230°C and 1350°C at 100kPa (Table 2.2, Figure 2.2). For each experiment, 50 mg of starting materials was mixed with methanol and sintered to a 0.15mm diameter Pt wire loop. Iron loss to Pt loops was avoided by presaturating the Pt loop with the starting material. Pt loop presaturation

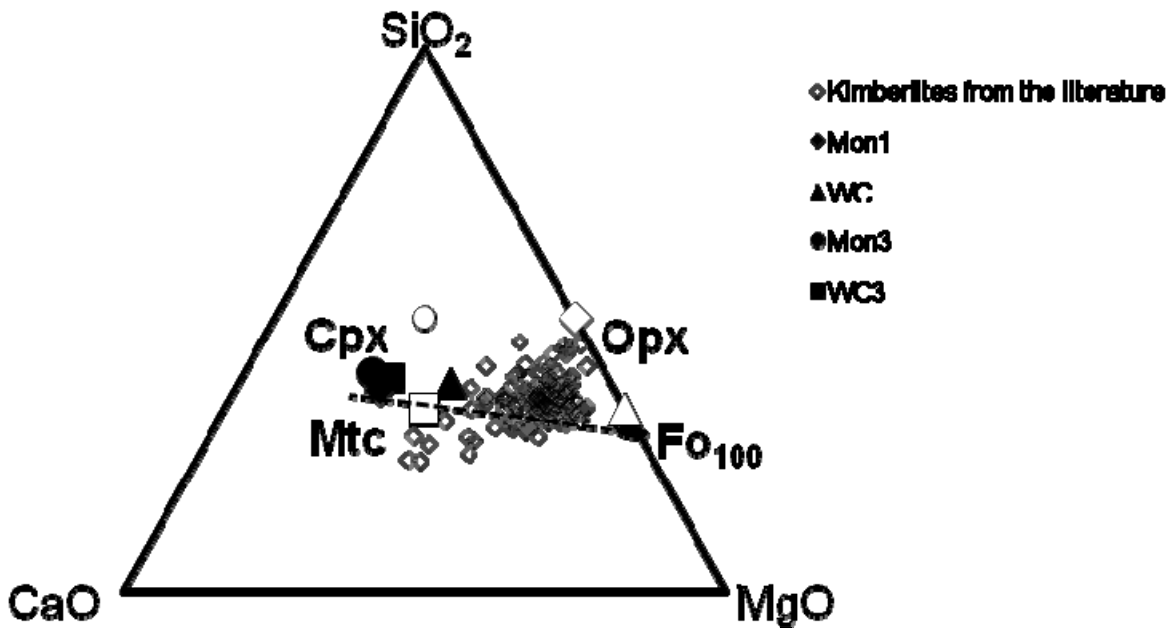

Figure 2.1. Ternary plot showing starting materials (mol%) derived from a worldwide kimberlite database. Fo_{100} was subtracted from the average worldwide kimberlite composition to account for the xenolithic olivine (dash line). Worldwide kimberlites database was compiled in another study (cf., Bellis & Canil, 2007). Cpx= Diopside (White circle); Opx= Orthopyroxene (White rhomb); Fo_{100}= Pure forsterite (White triangle); Mtc= Monticellite (White square).

Table 2.1. Starting compositions for experiments (wt%) from electron microprobe analyses (EMPA)

Oxide	WC	WC3	Mon1	Mon3
SiO_2	33.5	32.1	34.7	30.3
TiO_2	7.7	10.2	3.0	11.4
Al_2O_3	0.5	0.6	0.3	0.5
FeO[a]	12.0	13.0	8.2	14.4
MgO	21.6	13.7	15.6	11.5
CaO	22.4	27.4	35.8	28.6
V_2O_5	0.5	0.5	0.5	0.4
Total	97.8	97.5	98.4	97.0

[a] FeO as FeO total

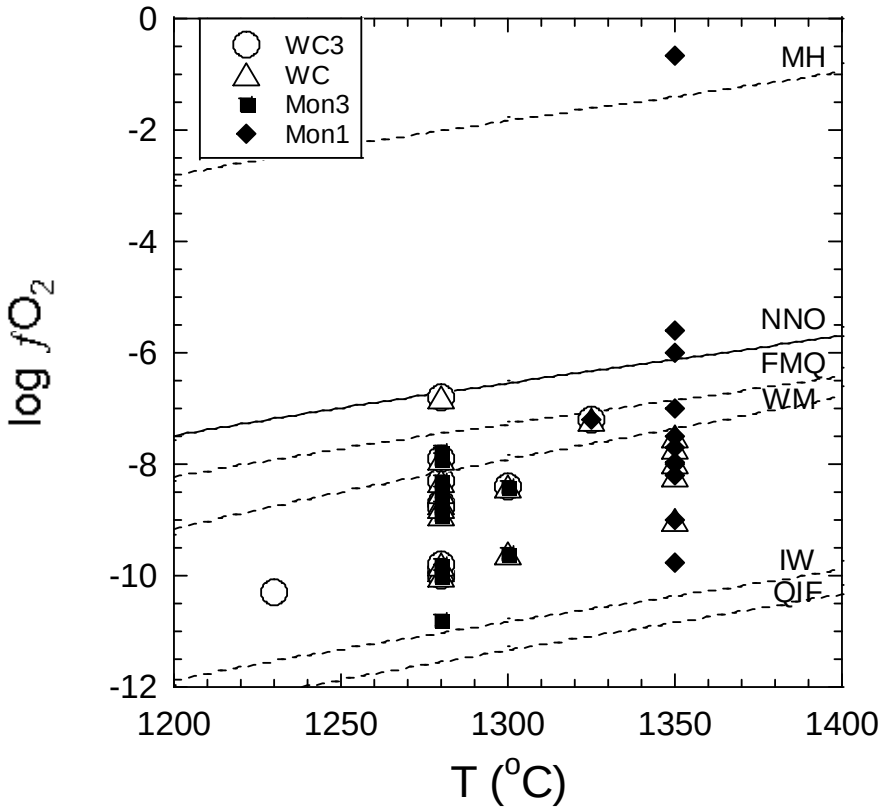

Figure 2.2. Experimental conditions relative to different buffers: QIF (Quartz-Iron-Fayalite); IW (Iron-Wüstite); WM (Wustite-Magnetite); FMQ (Fayalite-Magnetite-Quartz); NNO (Nickel-Nickel Oxide); MH (Magnetite-Hematite) from Frost, 1991.

involved first running an experiment at the desired T-fO_2 conditions (12 hours at 1350°C to 48 hours at 1230°C). The glass bead was then dissolved in HF and a new starting material was sintered to the pre-saturated Pt loop and held at the same T-fO_2 conditions for the final experiment (Table 2.2). Temperature was measured with either a Pt-$Pt_{90}Rh_{10}$ (Type-S) or $PtRh_{30}$-$Pt_{94}Rh_6$ (Type-B) thermocouple located within 1 cm of the Pt loops and calibrated at the melting point of gold (1,064°C). Uncertainty in the measurement of temperature was ±5°C. Oxygen fugacity was controlled by CO-CO_2 gas-mixing (total flow = 200 cm^3/min) and measured with a solid zirconia electrolyte cell. In some experiments large fluctuations in the EMF occurred likely due to loose electrical contacts, but I rejected those EMF values and used the CO-CO_2 gas mixing ratio from tables (Deines, 1974) instead to determine the fO_2 of experiments. For each experiment, samples were introduced to the vertical tube furnace and the desired fO_2 was achieved after about 5 minutes. After 24 hours, samples were removed from the furnace and quenched to a glass within seconds in a stream of air. Each run product was mounted in epoxy and polished for examination under the scanning electron microscope (SEM) for phase identification and the electron microprobe (EMP) for phase compositions.

2.2.3 Analytical methods

SEM examination of run products was done on a Hitachi S-4800 Scanning Electron Microscope at an accelerating voltage of 15kV and at a 20 nA primary beam current to determine the coexisting phases. Chemical compositions of phases were determined on a CAMECA SX50 electron microprobe operating in the wavelength-dispersion mode (University of British Columbia) and by a JEOL 733 Superprobe (University of Washington, Seattle). No inter-laboratory bias was observed in the chemical

compositions between these two instruments. Glasses were analyzed at the University of British Columbia under an excitation voltage of 15 kV and a beam current of 20 nA and with a 10 μm beam. The peak count time was of 20 s (100 s for V) and the background count-time of 10 s (50 s for V). The following standards, X-ray lines and crystals were used: kyanite, Al$K\alpha$, TAP; diopside, Mg$K\alpha$, TAP; diopside, Si$K\alpha$, TAP; diopside, CaKα, PET; rutile, TiKα, PET; V element, VKα, PET (corrected for TiKβ); synthetic rhodonite, Mn$K\alpha$, LIF; synthetic fayalite, Fe$K\alpha$, LIF. Synthetic monticellites were analyzed at the University of British Columbia under an excitation voltage of 15 kV, a beam current of 20 nA and 40 nA and with a 5 μm beam. Standards, X-ray lines and crystals were the same as for the glasses analyses. Data reduction was done using the 'PAP' $\phi(\rho Z)$ method (Pouchou & Pichoir, 1985). Glasses and synthetic monticellites compositions at the University of Washington were determined with a 15.0 kV accelerating voltage, a beam current of 20 nA with a focused beam of less than 1 μm in size. Both natural and synthetic standards were used for calibration: synthetic fayalite, forsterite ($Fo_{90.3}$), plagioclase ($An_{76.4}$), synthetic TiO_2, clinopyroxene ($Wo_{45.9}$, $En_{48.3}$, $Fs_{6.4}$). Data reduction was done using the CITZAF method (Armstrong, 1988). Ten analysis points were analyzed for both monticellite and glass in every run product and were averaged (Appendix A).

Chemical compositions of natural monticellites and perovskites in thin sections of kimberlites in this study were determined by wavelength-dispersive analysis using a CAMECA SX50 electron microprobe at the University of British Columbia. Monticellites and perovskites were analyzed under an excitation voltage of 15kV, a beam current of 20nA and a 1 μm beam. The peak count time and the background count-time

for monticellite were of 20 s and 10 s respectively. For REE, Fe and Nb in perovskites I used a peak and background counting times of 60 and 30 s, respectively. The following standards, X-rays lines and crystals used for the elements considered were: anorthite, AlKα, TAP; synthetic forsterite, MgKα, TAP; synthetic forsterite, SiKα, TAP; diopside, CaKα, PET; rutile, TiKα, LIF; synthetic rhodonite, MnKα, LIF; synthetic fayalite, FeKα, LIF for monticellites and CaKα, PET; rutile, TiKα, LIF; synthetic fayalite, FeKα, LIF; $LaPO_4$, LaLα, LIF; $CePO_4$, LaLα, LIF; $NdPO_4$, LaLα, LIF; columbite, NbLα, PET for perovskites. Data reduction was done using the 'PAP' $\phi(\rho Z)$ method (Pouchou & Pichoir, 1985).

2.3 Results

2.3.1 Phase equilibria

Monticellite is a stable liquidus phase throughout the entire T-fO_2 range in almost all the compositions I investigated (Table 2.2). Monticellite did not crystallize in the WC composition in pure CO_2 (NNO+5.3) at all temperatures limiting the number of analyses at high fO_2. In MON1, the crystallization order was monticellite > akermanite > merwinite, whereas in WC the order was olivine > monticellite > perovskite > (melilite, akermanite, gehlenite) (Bellis and Canil 2007). Grain sizes for phases were typically up to 200μm at 1350°C and greater than 400μm at and below 1280°C. Perovskite and olivine are stable throughout the entire fO_2 studied, but decrease in size with increasing fO_2. Spinel appears as minute grains at NNO > 0 at 1280°C but forms quite large crystals (up to 1000μm) at NNO+5.3. In rare cases, monticellite grew as larger crystals around olivine. In WC, WC3 and MON3, diopside crystallized at 1280°C and at fO_2 above NNO 0. In all run products, minerals concentrated at the bottom of the melt bead as a result of

the low viscosity of the melt (Figure 2.3). High-quality glass analyses were made in the large glass area in all run products except in MON1 at 1325°C and WC at 1280°C in which the melt fraction was small. In that case, I took great care of analyzing a sufficiently large area considering the EMP beam size (which was less than 1 μm) to avoid any contamination. Monticellite and glass were observed to have a homogenous composition in each run.

2.3.2 Equilibrium

Time series experiments were conducted on the WC, WC3 and MON3 compositions (Figure 2.4) at 1280°C. A constant XFe (molar Fe/(Fe+Ca+Mg)) of monticellite is attained after 12 hours, and the monticellite-melt Kd Fe^{2+}-Mg converges towards a constant value (~0.3) by 24 hours, suggesting that equilibrium was most likely achieved in the latter run duration (Figure 2.4). I found the olivine-melt Kd Fe^{2+}-Mg between 0.11 and 0.24 (n=30), which are in agreement with those found by Canil & Bellis (2008) (0.12 to 0.27). If Fe loss occurred, the olivine-melt Kd Fe^{2+}-Mg values would be higher than normal under equilibrium conditions. No reversal experiments have been conducted, but equilibrium is suggested by the convergence of the monticellite-melt Kd Fe^{2+}-Mg and by the lack of zoning in monticellite. Note that several experiments have been conducted above 1300°C of duration of 24 hours or less and demonstrated that equilibrium was achieved (e.g., Ballhaus et al., 1991; Kilinc et al., 1983; Kress & Carmichael, 1998). Other studies showed that 48 hours was required to attain equilibrium at T above 1200°C (e.g., Roeder & Emslie, 1970).

Table 2.2. Experimental run conditions and phase assemblages

Run #		T (°C)	Duration (hrs)	log fO_2	ΔNNO[a]	L	Prv	Ol	Mtc	Ak	Mer
DT583	Mon1	1350	24	-9.8	-3.8	X			X	X	X
DT585	Mon1	1350	24	-9.0	-3.0	X			X	X	X
DT588	Mon1	1350	24	-8.2	-2.2	X			X	X	X
DT662	Mon1	1325	24	-7.2	-1.0	X	X		X	X	X
W187	Mon1	1350	24	-7.0	-1.0	X			X	X	X
W191	Mon1	1350	24	-6.0	0.0	X			X	X	X
W194	Mon1	1350	24	-7.5	-1.5	X			X	X	X
W196	Mon1	1350	24	-0.7	5.3	X			X	X	X
W197	Mon1	1350	24	-5.6	0.4	X			X	X	X
W199	Mon1	1350	24	-8.0	-2.0	X			X	X	X
W210	Mon1	1350	24	-8.0	-2.0	X			X	X	X
W243	Mon1	1350	24	-7.7	-1.7	X			X	X	X
DT585	WC	1350	24	-9.0	-3.0	X		X	X		
DT588	WC	1350	24	-8.2	-2.2	X		X	X		
DT591	WC	1280	24	-9.9	-3.2	X	X	X	X	X	
DT595	WC	1280	24	-6.8	-0.1	X	X	X	X	X	
DT596	WC	1280	24	-8.7	-2.0	X	X	X	X	X	
DT598	WC	1280	24	-10.0	-3.3	X	X	X	X	X	
DT662	WC	1325	24	-7.2	-1.0	X	X	X	X		
DT665	WC	1300	24	-8.4	-2.0	X	X	X	X		
W194	WC	1350	24	-7.5	-1.5	X		X	X		
W204	WC	1300	24	-9.6	-3.1	X	X	X	X		
W206	WC	1280	24	-8.5	-1.8	X	X	X	X	X	
W208	WC	1280	24	-8.9	-2.2	X	X	X	X	X	
W210	WC	1350	24	-8.0	-2.0	X		X	X		
W218	WC	1280	24	-8.3	-1.6	X	X	X	X	X	
W220	WC	1280	24	-9.8	-3.1	X	X	X	X	X	
W223	WC	1280	24	-8.8	-2.1	X	X	X	X	X	
W232[T]	WC	1280	24	-7.9	-1.2	X	X	X	X	X	
W233[T]	WC	1280	12	-7.9	-1.2	X	X	X	X	X	
W243	WC	1350	24	-7.7	-1.7	X		X	X		
DT591	Mon3	1280	24	-9.9	-3.2	X	X		X	X	
DT598	Mon3	1280	24	-10.0	-3.3	X	X	X	X	X	
DT665	Mon3	1300	24	-8.4	-2.0	X	X		X	X	
W206	Mon3	1280	24	-8.5	-1.8	X	X		X	X	
W208	Mon3	1280	24	-8.9	-2.2	X	X		X	X	
W214	Mon3	1280	24	-10.8	-4.1	X	X		X	X	
W218	Mon3	1280	24	-8.3	-1.6	X	X		X	X	
W220	Mon3	1280	24	-9.8	-3.1	X	X		X	X	
W223	Mon3	1280	24	-8.8	-2.1	X	X		X	X	
W233[T]	Mon3	1280	12	-7.9	-1.2	X	X		X	X	
W240	Mon3	1280	24	-7.8	-1.1	X	X	X	X	X	
DT591	WC3	1280	24	-9.9	-3.2	X	X	X	X	X	
DT595	WC3	1280	24	-6.8	-0.1	X	X	X	X	X	
DT596	WC3	1280	24	-8.7	-2.0	X	X	X	X	X	
DT598	WC3	1280	24	-10.0	-3.3	X	X	X	X	X	
DT655	WC3	1230	48	-10.3	-3.1	X	X	X	X	X	
DT662	WC3	1325	24	-7.2	-1.0	X	X		X		
DT665	WC3	1300	24	-8.4	-2.0	X	X	X	X		

Run #		T (°C)	Duration (hrs)	log fO_2	ΔNNO[a]	L	Prv	Ol	Mtc	Ak	Mer
W218	WC3	1280	24	-8.3	-1.6	X	X	X	X	X	
W220	WC3	1280	24	-9.8	-3.1	X	X	X	X	X	
W223	WC3	1280	24	-8.8	-2.1	X	X	X	X	X	
W232[T]	WC3	1280	24	-7.9	-1.2	X	X	X	X	X	
W233[T]	WC3	1280	12	-7.9	-1.2	X	X	X	X	X	

All experiments were made at 100kPa.

[a]T-log fO_2 relation for this buffer given in Frost (1991)

[T]Time series experiments (12 hours, 24 hours)

L: liquid; Prv: Perovskite; Ol: Olivine; Mtc: Monticellite; Ak: Akermanite; Mer: Merwinite.

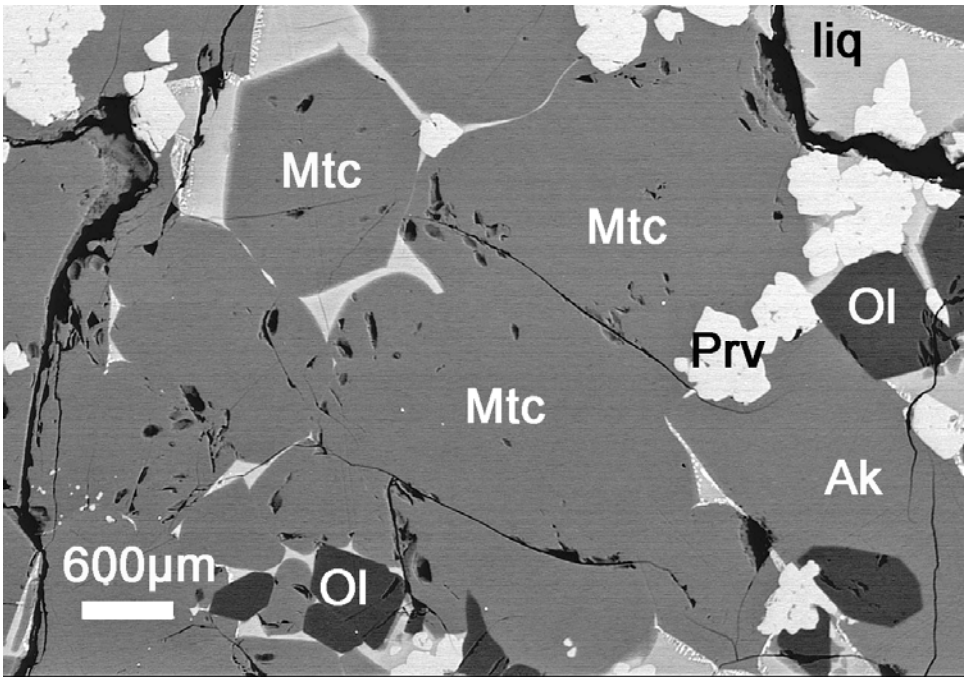

Figure 2.3. Plate detector back-scattered electron (PDBSE) image of a run product (WC3) at 1280°C and NNO-1.2. Prv=Perovskite, Ol=Olivine, Ak=Akermanite, Mtc=Monticellite, Liq=Liquid.

2.3.3 Effect of fO_2, T and bulk composition on XFe of monticellite and liquid and monticellite-melt Kd Fe^{2+}-Mg

The $Fe^{3+}/\Sigma Fe$ ratio of the liquid in equilibrium with monticellite calculated by the method of Kress & Carmichael (1988) changes substantially above NNO-2.0 but less so below NNO-2.0 (Figure 2.5). Because the $Fe^{3+}/\Sigma Fe$ ratio does not change much below NNO-2.0, I expect the XFe of monticellite to show little variation below this fO_2 if only Fe^{2+} partitions into its structure, as observed (Figure 2.6). I observe a constant decrease of silica in the liquid in equilibrium with monticellite with increasing fO_2. In the liquid, no positive correlation was found between TiO_2 and SiO_2 nor between TiO_2 and monticellite-melt Kd Fe^{2+}-Mg. I conclude that the TiO_2 content of the liquid in equilibrium with monticellite does not affect my results.

The XFe of monticellite shows a strong correlation with fO_2 and temperature. At 1350°C XFe_{Mtc} increases from 0.01 at NNO+5.3 to a nearly constant 0.07 below NNO-1.7 (Figure 2.6) reflecting nearly constant Fe^{2+} in the liquid below this fO_2. At lower temperatures, XFe_{Mtc} in all compositions increases from 0.09 to 0.14 over a decrease in fO_2 from NNO to NNO-4. At a given fO_2, XFe_{Mtc} increases from 0.06 to 0.17 over a decrease of 120°C (Figure 2.7). There is only a minor effect of bulk composition (Mg#) (±0.02 units) on XFe_{Mtc} where Mg# = molar MgO/(MgO+FeO*) and FeO* is the total FeO.

In comparison to the XFe_{Mtc} the partitioning of total Fe between monticellite and liquid, $D_{Fe}^{Mtc/liq}$ expressed as XFe_{Mtc}/XFe_{liq}, shows only a slight dependence upon temperature (±0.03 units) and bulk composition (Mg#) (±0.03), but a significant change with fO_2 (Figure 2.9). The monticellite-melt Kd Fe^{2+}-Mg ranges from 0.18 to 0.41 (Figure 2.8). At a given T and fO_2, the monticellite-melt Kd Fe^{2+}-Mg increases from 0.33

to 0.36 as the Mg# of the starting material decreases from 0.76 to 0.59. Note that the monticellite-melt Kd Fe^{2+}-Mg tends to decrease with the molar silica content of the liquid in MON1 and MON3 with increasing fO_2 (Figure 2.8a) and decreases with increasing Mg# (Mg/(Mg+total Fe)) of monticellite, but the latter is believed to reflect the change in the fO_2.

2.4 Discussion

2.4.1 Influence of fO_2 on Fe in Monticellite and Liquid

Temperature and bulk composition are the dominant variables controlling the phase appearance in my experiments, with limited influence of fO_2. For all starting materials, XFe_{Mtc} was found to vary strongly with fO_2 over a temperature range from 1280°C to 1350°C. XFe_{Mtc} in MON1 (and WC at 1350°C) composition shows constant values below NNO-1.7 whereas that trend is not observed in the three other compositions. At 1350°C, the fO_2 has little to no effect on the XFe_{Mtc} in MON1 and WC compositions below NNO-1.7 because there is little change in the $Fe^{3+}/\Sigma Fe$ ratio of the liquid at those conditions. That same relationship is not observed at 1280°C in WC, WC3 and MON3, which show a steady increase of XFe_{Mtc} with decreasing fO_2 below NNO-1.7. The disparities between the two trends (1350°C and 1280°C) could be due to the difference in the phase assemblages. Akermanite takes Fe^{2+} and minor Fe^{3+} (Seifert et al., 1987; Wiedenmann et al., 2009) into its structure, perovskite accepts only Fe^{3+} and both phases are absent in WC composition at 1350°C but present at 1280°C. The competition for Fe^{2+} in the melt between monticellite and akermanite may accentuate the decrease of Fe^{2+} in the liquid with crystallization. Conversely the uptake of Fe^{3+} by perovskite at higher fO_2 may also decrease the bulk Fe in the liquid, and explain the slightly different

trend observed between 1350 and 1280°C. The trend of XFe_{Mtc} in MON3 can be explained by the same mechanism as in WC and WC3. The crystallization of perovskite (and olivine in two runs) and the disappearance of merwinite may affect the partitioning of Fe between monticellite and the coexisting liquid.

I obtained olivine-melt Kd Fe^{2+}-Mg values between 0.11 and 0.24, similar to other studies on analogue kimberlites (Canil & Bellis, 2008) and much lower than those of basaltic rocks at low pressure, likely because of the low silica activity of kimberlites (Canil & Fedortchouk, 2001). The monticellite-melt Kd Fe^{2+}-Mg is found to be independent of temperature and the TiO_2 of liquid, but increases with SiO_2 of the liquid and decreases with fO_2 (Figure 2.8). Note that the low monticellite-melt Kd Fe^{2+}-Mg (0.18) is likely due to non-equilibrium experiments, e.g., MON1 at 1325°C in which the melt fraction is small and is excluded from the calibration. The effect of the bulk composition on the monticellite-melt Kd Fe^{2+}-Mg remains small but one may consider the fO_2 dependence as important.

It is evident from these data that the use of XFe_{Mtc} on its own cannot independently determine temperature or fO_2 of kimberlite liquids. As noted above, the XFe_{Mtc} is clearly dependent on temperature at constant fO_2. On the other hand, a multilinear regression of all data demonstrates that the effect of temperature (T) upon $D_{Fe}^{Mtc/liq}$ is minor ($\Delta NNO = 16.31\ (10) - 0.008\ (0.006) * T - 11.63\ (2.00) * D_{Fe}^{Mtc/liq}$, with a R^2 of 78%. T is in kelvins.) and can be discarded. Thus, one can treat the exchange of total Fe between monticellite and liquid (XFe_{Mtc}/XFe_{liq}) and its relationship with fO_2 at any temperature (as ΔNNO, where ΔNNO = fO_2 of experiment - fO_2 of the NNO buffer at the same T) according to the relationship conceived for the Cr redox in

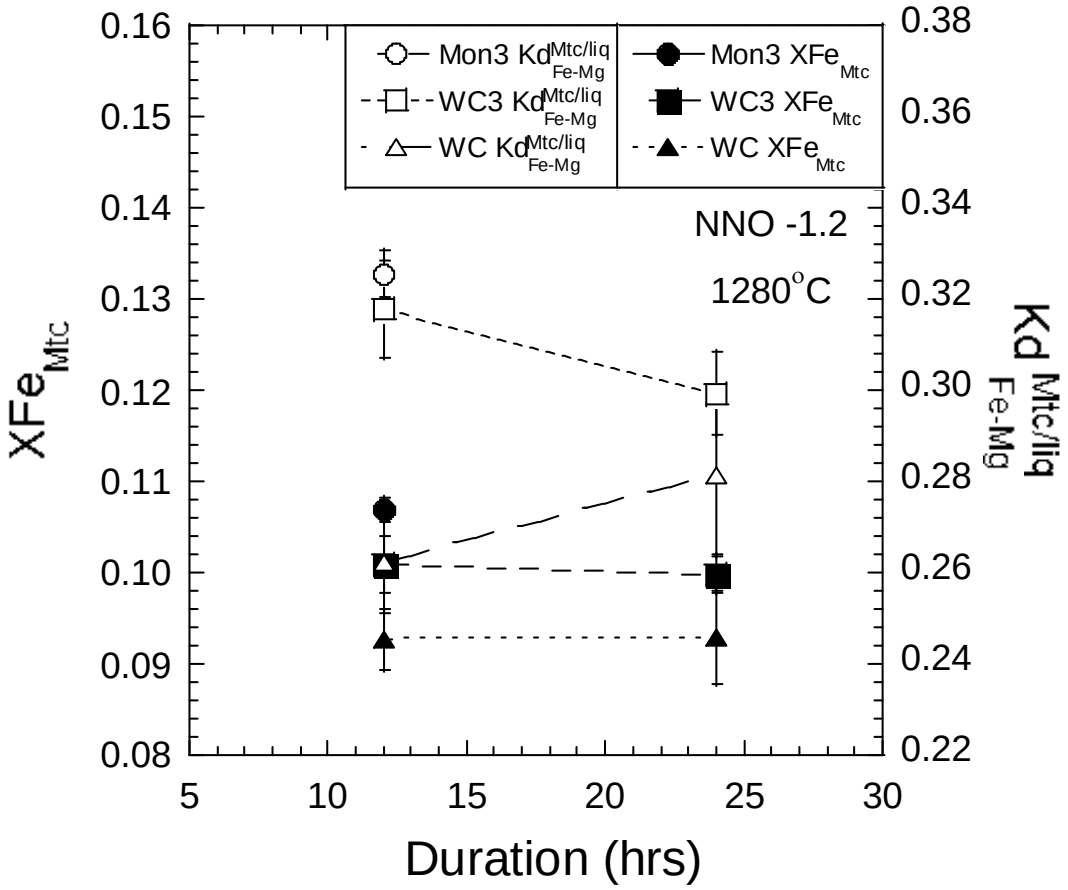

Figure 2.4. Time series experiments conducted on WC3, WC and Mon3 compositions at 1280°C and NNO-1.2. XFe_{Mtc} is constant after 12 hours, suggesting that equilibrium is possibly achieved. The converging Fe^{2+}-Mg partitioning coefficient between monticellite and liquid suggests that equilibrium is truly attained after 24 hours. XFe_{Mtc}=molar Fe/(Fe+Ca+Mg). Error bars are ± 1σ.

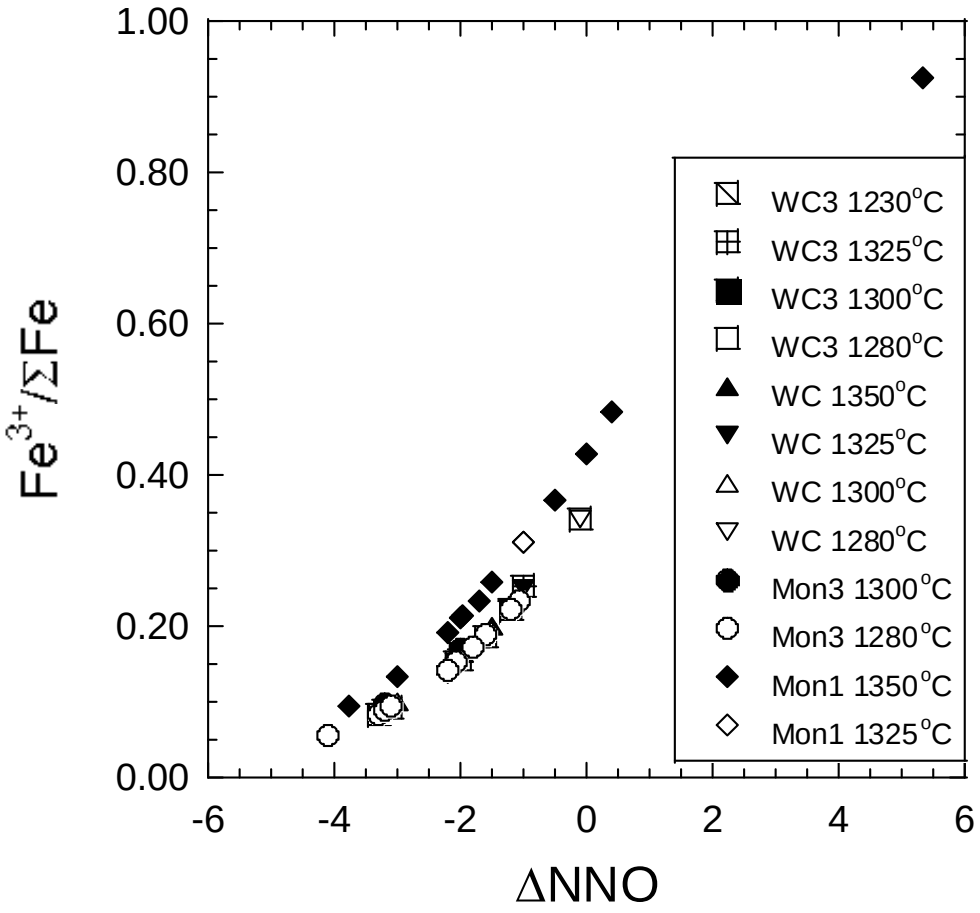

Figure 2.5. Iron oxidation as a function of fO_2 in coexisting liquids at 1350°C, 1325°C, 1300°C, 1280°C and 1230°C calculated using Kress & Carmichael's equation (1988).

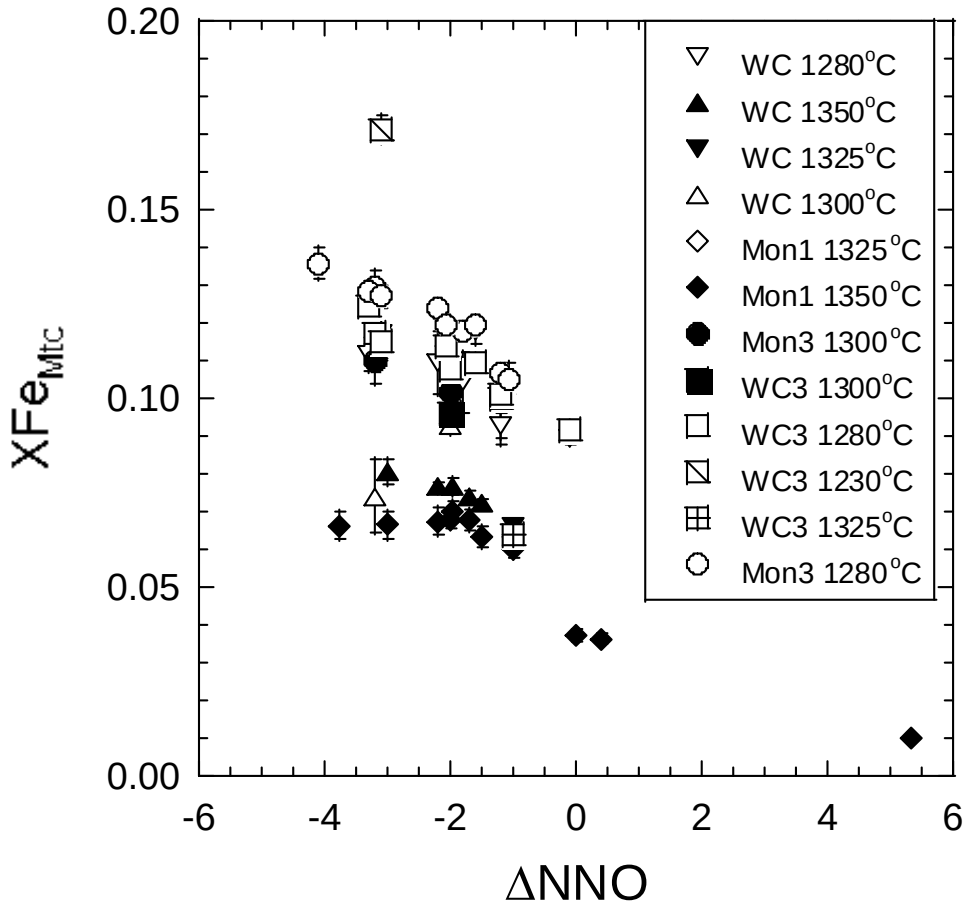

Figure 2.6. XFe_{Mtc} as a function of fO_2 expressed relative to the NNO buffer for all compositions at all temperatures. (ΔNNO= fO_2 of experiment-fO_2 of the NNO buffer at the same T). Error bars are ± 1 σ. When not visible, error bar is smaller than the symbol.

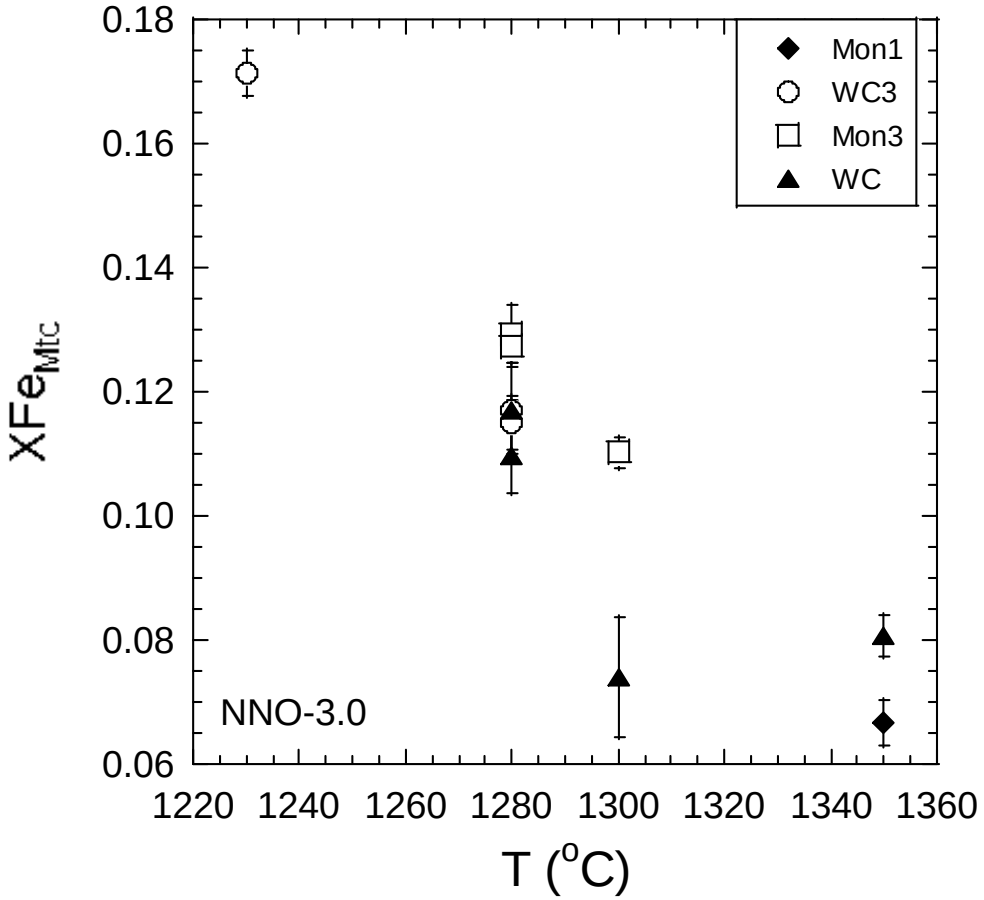

Figure 2.7. Dependence of XFe_{Mtc} upon temperature at NNO-3.0. Error bars are ± 1 σ.

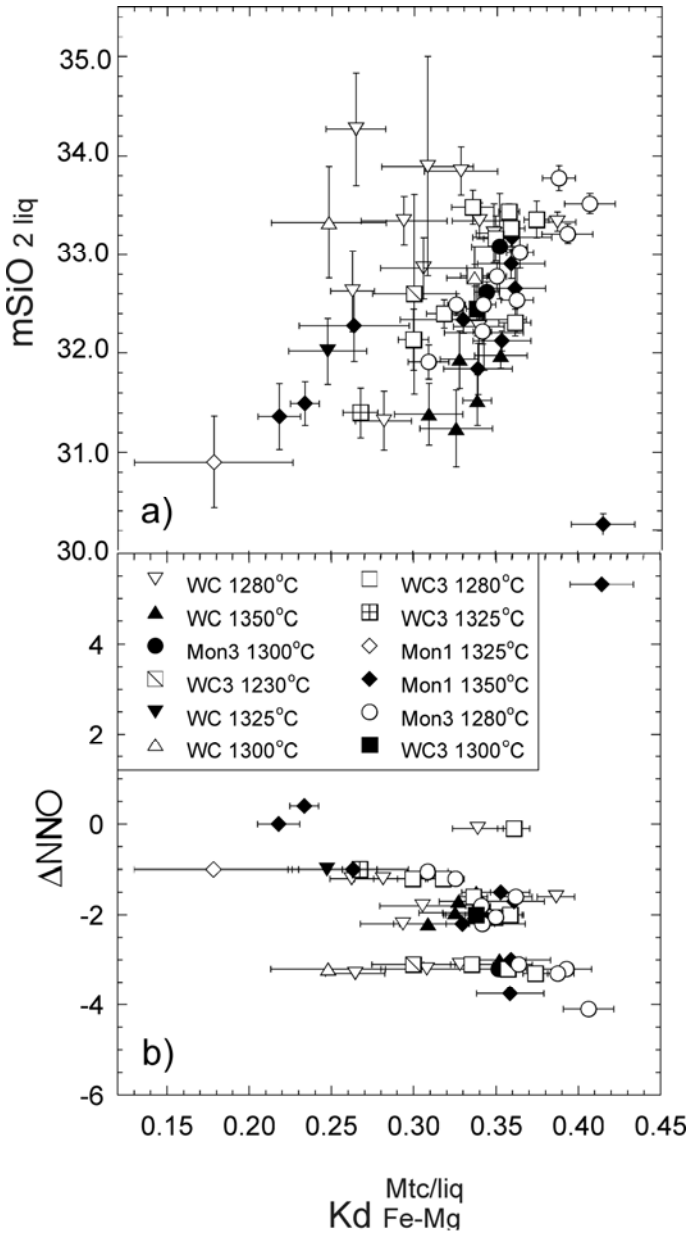

Figure 2.8. a) Covariation of monticellite-liquid Kd Fe^{2+}-Mg and the mole SiO_2 of liquid showing the decreasing trend of the $mSiO_2$ of liquid with the decreasing Fe^{2+}-Mg partitioning coefficient in MON1 and MON3 b) Fe^{2+}-Mg partitioning coefficient between monticellite and coexisting liquid in function of the fO_2 expressed relative to the NNO buffer. Note the decreasing trend of the Fe^{2+}-Mg partitioning coefficient with fO_2 in MON1 and MON3. Error bars are ± 1 σ.

melts (Roeder & Reynolds, 1991), but adapted here for Fe redox:

$$log\left[d\frac{X_{Fe}^{liq}}{X_{Fe}^{Mtc}}-1\right]=b*\Delta NNO+c \qquad (2)$$

where XFe = mole fraction total Fe/(Σcations). In this way, weighted least-square regression of all data between 1230 and 1350°C over a range of fO_2 from NNO-4.1 to NNO +5.3 (Figure 2.9) can be fitted to the relationship:

$$\Delta NNO=\frac{\left\{\log\left[0.858(\pm0.021)\frac{X_{Fe}^{liq}}{X_{Fe}^{Mtc}}-1\right]-0.139(\pm0.022)\right\}}{0.193(\pm0.004)} \qquad (3)$$

I found a fO_2 coefficient (b) of ~ 0.20, as did others for the homogeneous ferric-ferrous equilibrium in basalt and andesite liquids (Fudali, 1965; Kilinc et al., 1983; Kress & Carmichael, 1988; Roeder & Emslie, 1970; Sack et al., 1980), suggesting that Fe exhibits a slightly different valence change than the b=0.25 expected for the reaction $FeO+\frac{1}{4}O_2=FeO_{1.5}$. Equation 3 reproduces 70% of all experimental data (n=39) to within 0.5 log fO_2 unit and 90% of the data (n=50) to within 1.0 log fO_2 unit (Figure 2.10).

2.5 Application of the Fe-in-monticellite oxybarometer to natural kimberlites

I now apply the Fe-in-monticellite oxygen barometer to natural kimberlites and compare results with previous kimberlite oxygen barometers (Bellis & Canil, 2007; Fedortchouk & Canil, 2004). I first apply my calibration to monticellite compositions compiled from the literature and then to my own detailed study of monticellites. I used the Clement contamination index (C.I.) to discriminate non-contaminated kimberlites, and follow the approach of Nowicki et al. (2008) by using only uncontaminated kimberlite (C.I. < 1.0) to avoid any ambiguity in the choice of kimberlites.

2.5.1 Monticellite compositions compiled from the literature

I selected examples of fresh kimberlites from the literature for this exercise: Leslie (Armstrong et al., 2004), Elwin Bay (Mitchell, 1986; Mitchell, 1978), De Beers (Mitchell, 1986) and Dutoitspan (Mitchell, 1986) (Appendix B). These kimberlites are all hypabyssal kimberlites (with Elwin Bay being a hypabyssal-tuffisitic kimberlite). Detailed descriptions of kimberlites and monticellites can be found in the respective publications. Because kimberlites do not contain glass, I assume the total XFe of the melt (coexisting with monticellite) as equal to the total XFe of the whole rock composition (Appendix C). All bulk compositions were recalculated on a volatile-free basis (CO_2 and H_2O). Because the total XFe of the bulk composition and XFe_{Mtc} in a sample were not always reported in the same study, I at times obtained total XFe of the bulk compositions from other studies from the same pipe (Bellis & Canil, 2007; Berg & Carlson, 1998; Clement, 1982; Fedortchouk & Canil, 2004; Le Roex et al., 2003; Nowicki et al., 2008). As the Fe-in-monticellite oxygen barometer was calibrated with kimberlitic compositions, I caution the reader in applications to alnoïtes, aillikites, melilitites, carbonatites and any other rock types that may contain monticellite. My criteria were that monticellite must be fresh and cognate to the kimberlite to obtain reliable fO_2 values.

The range in total XFe_{Mtc} and XFe_{liq} from the compilations varies from 0.014 to 0.044 and from 0.059 to 0.067 respectively (Figures 2.11a and b). Bulk FeO compositions were averaged for each pipe. The averaged fO_2 calculated using equation 3 varies from NNO-1.8 to NNO+1.5 (Figure 2.11c) with the exception of Elwin Bay, which are surprising low, and are discussed further below in my own detailed studies of this pipe.

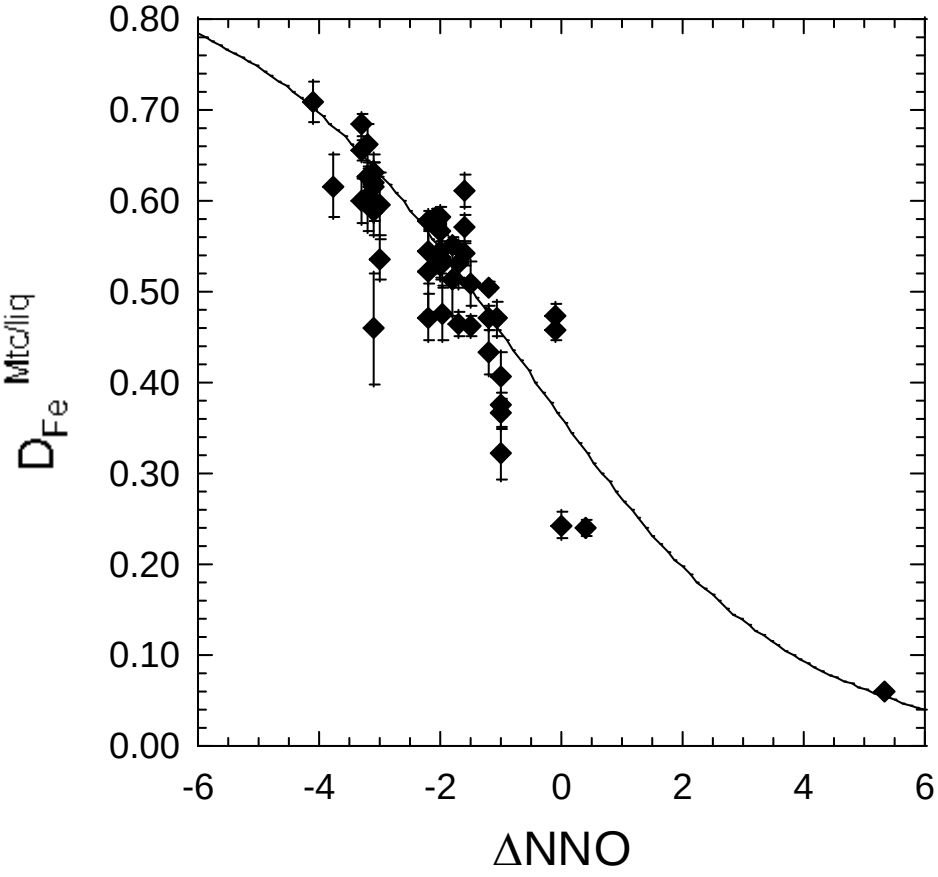

Figure 2.9. Covariation between $D_{Fe}^{Mtc/liq}$ and fO_2 relative to the nickel-nickel oxide buffer (ΔNNO= fO_2 of experiment- fO_2 of the NNO buffer at the same T) from Frost (1991). Trend line fitted using equation (2) in text: ΔNNO= {log [0.858*XFe_{liq}/XFe_{Mtc}-1]-0.139}/0.193. Error bars are ± 1 σ. Regression coefficients b, c and d are respectively 0.193 ± 0.004, 0.139 ± 0.022 and 0.858 ± 0.021 and R^2 is 0.973. $D_{Fe}^{Mtc/liq}$ is expressed as XFe_{Mtc}/XFe_{liq} where XFe is the mole fraction of total Fe/Σcations.

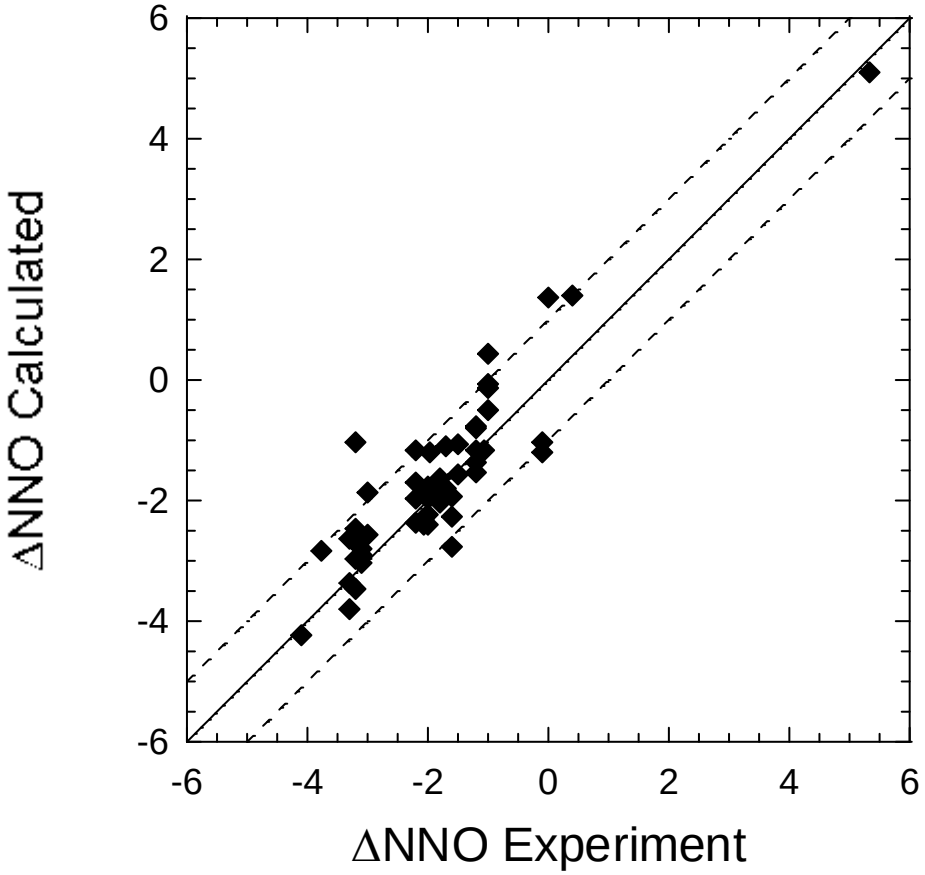

Figure 2.10. fO_2's calculated with my Fe oxygen barometer vs fO_2's of experiments relative to the NNO buffer. The 1:1 line is shown along with two dash lines constraining ± 1 log fO_2 unit for reference.

I compared my oxygen barometer with the Fe-in-perovskite oxygen barometer of Bellis & Canil (2007). Perovskite compositions, containing less than 1 wt% Nb and having crystal size between 10-100µm, were compiled from the Elwin Bay (Bellis & Canil, 2007; Chakhmouradian et al., 2000; Wu et al., 2010), De Beers (Batumike et al., 2008; Nowicki et al., 2009) and Dutoitspan (Nowicki et al., 2009) Group-I kimberlites. The reader is referred to the latter publications for a description of perovskites and kimberlites. The perovskite analyses are not from the identical sample as monticellite, introducing a bias in the determination of fO_2. Euhedral perovskites from Elwin Bay are known to have crystallized from the least contaminated or contamination-free kimberlite magmas, and are described as fresh grains crystallized in the earlier stage of kimberlite crystallization (Wu et al., 2010). Bellis & Canil's (2007) oxygen barometer gives fO_2 values similar to those calculated with the Fe-in-monticellite for De Beers and Dutoitspan kimberlites but not for the Elwin Bay kimberlite (Table 2.3). The discrepancy in fO_2's in the latter case from both oxygen barometers is striking. In order to understand this discrepancy and to apply my oxygen barometer rigorously, I need more detailed mineral compositions and textural information on monticellite and perovskite and to consider analyses from the same sample. To this end, I applied the Fe-in-monticellite oxygen barometer to monticellites I studied in my own thin sections.

2.5.2 Monticellite compositions from detailed study

I examine four different kimberlite pipes, Elwin Bay, Grizzly, Leslie and Aaron, to determine the fO_2 during the crystallization of the groundmass at the time of monticellite and perovskite crystallization in fresh hypabyssal kimberlites from thin sections and then discuss the potential limitations of the Fe-in-monticellite oxygen

barometer. In these samples, analyses of monticellite and bulk compositions of a given pipe come from the same sample.

2.5.2.1 Lac De Gras kimberlites

The Grizzly, Aaron and Leslie kimberlites are Eocene-aged fresh hypabyssal facies kimberlites from the Lac De Gras area, in the Archean Slave Province of Canada (Fedortchouk & Canil, 2004). The Leslie and Aaron kimberlites are macrocrystic hypabyssal monticellite kimberlites whereas the Grizzly pipe is a macrocrystic and heterolithic serpentine-spinel-carbonate-monticellite hypabyssal kimberlite. The Leslie and Aaron kimberlites contain 10-15% of 50-100 µm (rarely up to 800 µm) subhedral to anhedral (rarely euhedral) monticellite whereas the Grizzly kimberlite is made up of tiny anhedral monticellite up to 40µm in size (cf., Table 2.4). Perovskite was found as discrete euhedral and subhedral crystals (less than 50µm in size) only in the Grizzly kimberlite and is commonly of type-II (enriched in Al, Fe, Nb and light REE). Detailed descriptions of each kimberlite studied can be found in Canil & Bellis (2007) and Fedortchouk & Canil (2004).

2.5.2.2 Somerset Island kimberlite

The Elwin Bay kimberlite is a Cretaceous-aged kimberlite from Somerset Island, Canada and is described as a hypabyssal and tuffisitic kimberlite, showing some altered olivines (serpentinisation, chloritization and calcite alteration). The Elwin bay kimberlite is unique in that it contains large amount of monticellite (up to 50%), varying from 50 to 400µm in size, and showing a large (up to 18 mol%) solid solution with kirschteinite ($CaFeSiO_4$) and olivine (Mitchell, 1978). Monticellite occurs as both euhedral and subhedral-anhedral (resorbed?) crystals, and is commonly zoned (cf., Table

2.4). Perovskite is present in the groundmass as oval anhedral, subhedral and euhedral crystals of 70µm and less in size, with rare mineral inclusions. Crystals are commonly unzoned and mantled by Fe-Ti oxides. Detailed description of the Elwin Bay perovskite can be found in Canil & Bellis (2007). Back-scattered electron images of Elwin Bay and Aaron kimberlites are depicted on Figure 2.12.

The total XFe of monticellite and of the bulk composition for each kimberlite pipe are illustrated on Figures 2.13a and 2.13b. The Lac de Gras kimberlites (Leslie, Grizzly and Aaron) give fO_2 values at or slightly above the NNO buffer whereas Elwin Bay kimberlite gives a wide range of fO_2 going from undetermined values to NNO-2.1 (Figure 2.13c; Table 2.4). The latter result was also obtained for Elwin Bay monticellites from the literature (Table 2.3). Elwin Bay monticellites are enriched in Fe and variable in zoning patterns, even within a single thin section. Cores are homogeneous in composition (except in two rare cases; cf., Table 2.4) whereas rims are either Fe-rich or Fe-poor meaning that there are at least two generations of monticellite resulting from either multiple magma intrusions and mixing, fluidization or alteration near the surface during emplacement. Re-equilibration of monticellites with the magma is ruled out because rims would all show a similar composition which is not the case**.** Nonetheless, the zoning and multiple generations of monticellite lead to complications in application of the Fe-in-monticellite oxybarometer for this pipe. In contrast, no zoning was observed for monticellite in the Leslie and Aaron kimberlites. Fresh hypabyssal facies kimberlites (Leslie, Aaron and Grizzly) are not affected by any secondary changes as reflected in their uniform monticellite compositions and fO_2. The fO_2 determined for euhedral monticellite does not differ from that for subhedral-anhedral monticellite in these

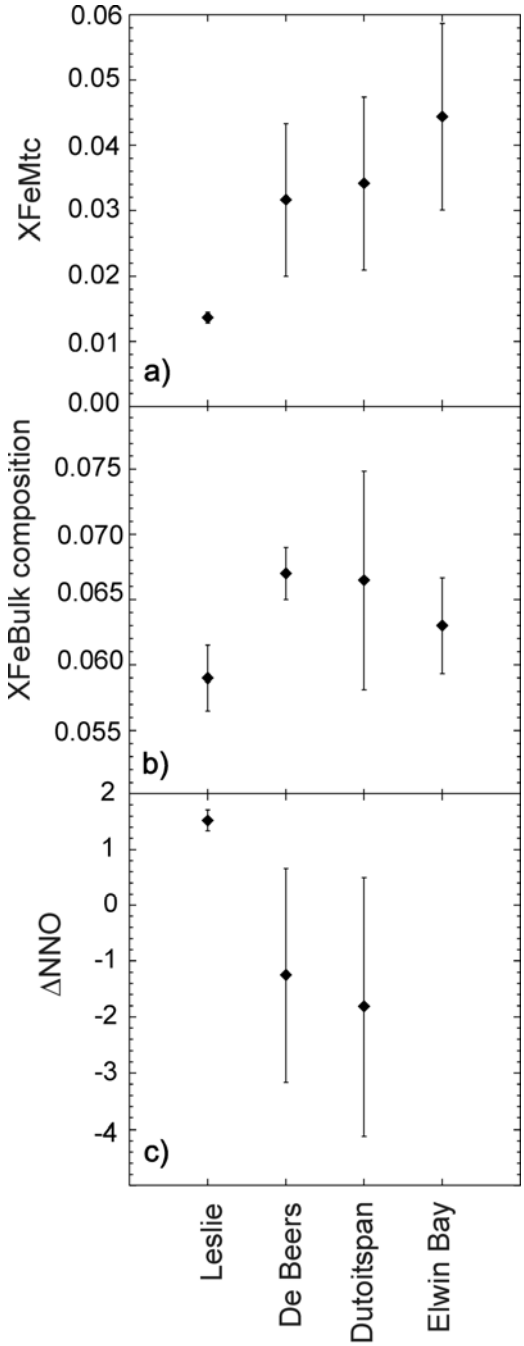

Figure 2.11. a) XFe of monticellite, b) XFe of the bulk composition and c) fO_2's (relative to the NNO buffer) calculated with equation 3 for monticellite compositions compiled from the literature. Error bars are ± 1 σ. Note that because of the complex zoning in Elwin Bay monticellites, the Fe-in-monticellite oxygen barometer cannot be applied to this kimberlite and gives spurious and non reliable results.

Table 2.3. Comparison between the Fe-in-perovskite oxygen barometer (Bellis & Canil, 2007) and the Fe-in-monticellite oxygen barometer for monticellites and perovskites compiled from the literature[c] and from selected kimberlite thin sections[d]

Kimberlite	**ΔNNO_{Mtc}[a]**	**STDEV (1σ)**	**ΔNNO_{Prv}[b]**	**STDEV (1σ)**
De Beers[c]	-1.2	1.9	1.0[e] and -3.5[f]	N.D.
Dutoitspan[c]	-1.8	2.3	-3.4[f]	N.D.
Elwin Bay[c]	N.D. to -2.5	N.D.	-2.0	1.7
Elwin Bay (cores)[d]	N.D. to -2.1	N.D.	-1.9	0.9
Grizzly (cores)[d]	0.02	1.4	0.7	1.1

[a] ΔNNO_{Mtc}: ΔNNO calculated with the Fe-in-monticellite oxygen barometer (equation 3)

[b] ΔNNO_{Prv}: ΔNNO calculated with the Fe-in-perovskite oxygen barometer (Bellis & Canil, 2007)

[c] Monticellites and perovskites from the literature

[d] Monticellites and perovskites from selected thin sections

[e] from Batumike et al. 2008

[f] from Nowicki et al. 2009

kimberlites. Similar fO_2 values are obtained for the Leslie kimberlite from both the literature compilation and in my own detailed study, implying that the choice of XFe_{liq} from different samples does not play a significant role in the determination of the fO_2 of Leslie kimberlites. The results suggest that the Fe-in-monticellite cannot be applied easily to facies other than fresh hypabyssal, or to pipes in which there may be spurious alteration of mineral compositions (e.g., Elwin bay kimberlite).

Both perovskite (cf., Table 2.5) and monticellite oxygen barometers give similar fO_2 for the Grizzly kimberlite within uncertainty (Table 2.3). Using the oxides in olivine phenocrysts Fedortchouk & Canil (2004) reported fO_2 values for the Leslie, Grizzly and Aaron pipes of ~NNO-3.0 after correction for the a_{SiO2} of kimberlite. Those values are not within uncertainties with the fO_2 calculated with the Fe-in-monticellite and Fe-in-perovskite oxygen barometers. Fedortchouk & Canil (2004) may have assumed an incorrect a_{SiO2} or alternatively, chromite-olivine phenocrysts, having precipitated first, captures an fO_2 for crystallization that is earlier and different than monticellite or perovskite, which crystallized later.

The use of the XFe of the whole rock composition to represent the XFe_{liq} in equilibrium with monticellite introduces an uncertainty in the determination of the fO_2 of kimberlites. Several studies have reported estimates of the primitive compositions by several approaches (Arndt et al., 2010; Becker & Le Roex 2006; Brett et al., 2009; Canil & Bellis, 2008; Harris et al., 2004; Kjarsgaard et al., 2009; Kopylova et al., 2007; Le Roex et al., 2003; Patterson et al., 2009; Price et al., 2000; Sparks et al., 2009). There is a consensus in these studies about the difficulties in tracing the primitive composition of kimberlites. Kimberlite liquid estimates are subject to large uncertainties because

different pipes may have different types of xenoliths/xenocrysts (lherzolitic, harzburgitic and MARID suite xenocrysts). The FeO* of the kimberlite liquid composition is possibly affected by both mantle and crustal rock contamination and this can play an important role in the determination of the fO_2 in my approach. I made my best attempt to filter for that effect, and note that the whole rock FeO is narrow for the database of worldwide kimberlites (5 to 11 mol% FeO). The advantage of the present oxygen barometer over oxide-olivine phenocrysts is that the latter assumes the $a_{SiO2\ liq}$ which is not precisely known. I can also apply the Fe-in-monticellite for kimberlite magmas that do not contain perovskite and/or oxides in olivine phenocrysts. Nonetheless, better estimates of the liquid composition of kimberlites are needed in order to pinpoint the exact fO_2 using my Fe-in-monticellite oxygen barometer, as well as to understand the physical nature of kimberlite magmas during emplacement (Sparks et al., 2009). In this respect, monticellite chemistry may play an important role in estimating the composition of kimberlite liquids after ascent and during crystallization.

2.6 Using monticellite to estimate kimberlite liquid compositions

Unlike olivine, monticellite cannot be a mantle xenocryst, and only crystallizes in kimberlite magmas at low pressure (< 0.5 GPa). The monticellite-melt Kd Fe^{2+}-Mg varies between 0.22 and 0.40 (mainly because of the fO_2 dependence) and provides a mean of determining the Mg# of the melt ($Mg/(Mg+Fe^{2+})$) coexisting with monticellite. In this section, I calculate the composition of the primitive kimberlite melt from the monticellite composition and the monticellite-melt Kd Fe^{2+}-Mg determined experimentally in several kimberlites both from literature and from my own work

Table 2.4. Chemical analyses of monticellites (wt%) and fO_2's calculated

Sample	Location	Type	Kimberlite facies[a]	Habit	SiO_2	TiO_2	Al_2O_3	FeO*[c]	MnO	MgO	CaO	Total	ΔNNO[b]
LS1-1	Leslie	Rim	HK	N.D.	37.5	0.07	0.03	2.2	0.5	25.3	33.8	99.4	0.9
LS1-1	Leslie	Core	HK	N.D.	37.4	0.20	0.02	2.1	0.4	25.5	34.1	99.6	1.0
LS1-2	Leslie	Core	HK	N.D.	37.4	0.13	0.02	2.1	0.4	25.8	34.5	100.3	1.2
LS1-3	Leslie	Core	HK	Subhedral	36.9	0.22	0.00	1.9	0.4	25.2	34.1	98.7	1.4
LS1-4	Leslie	Rim	HK	Anhedral	37.4	0.04	0.01	2.0	0.3	25.5	34.3	99.6	1.2
LS1-4	Leslie	Core	HK	Anhedral	37.0	0.10	0.04	2.2	0.3	25.1	34.1	98.7	1.0
LS1-5	Leslie	Rim	HK	Subhedral-euhedral	37.2	0.10	0.04	2.3	0.5	25.5	33.5	99.2	0.8
LS1-5	Leslie	Core	HK	Subhedral-euhedral	37.4	0.21	0.05	2.3	0.6	25.7	33.5	99.6	0.8
LS1-6	Leslie	Core	HK	Subhedral	36.6	0.11	0.03	2.0	0.3	24.9	34.6	98.5	1.2
LS1-7	Leslie	Rim	HK	Subhedral-euhedral	37.5	0.07	0.02	2.0	0.4	25.7	34.1	99.9	1.3
LS1-7	Leslie	Core	HK	Subhedral-euhedral	37.0	0.24	0.06	2.0	0.4	25.3	34.3	99.3	1.3
LS1-8	Leslie	Rim	HK	Euhedral	37.1	0.14	0.03	2.0	0.4	25.8	33.6	99.1	1.2
LS1-8	Leslie	Core	HK	Euhedral	36.5	0.07	0.02	2.2	0.3	25.3	34.0	98.4	0.9
LS1-9	Leslie	Core	HK	Subhedral	37.3	0.15	0.04	2.2	0.4	25.6	33.7	99.3	1.0
LS1-10	Leslie	Core	HK	Subhedral	37.7	0.07	0.04	2.3	0.3	25.2	34.3	100.0	0.7
LS1-11	Leslie	Rim	HK	Subhedral-euhedral	37.5	0.12	0.02	1.9	0.4	25.5	34.2	99.7	1.3
LS1-11	Leslie	Core	HK	Subhedral-euhedral	37.5	0.10	0.05	2.2	0.4	25.6	33.9	99.8	0.9
LS1-12	Leslie	Rim	HK	Subhedral-euhedral	37.7	0.07	0.04	2.0	0.4	25.8	34.0	99.9	1.2
LS1-12	Leslie	Core	HK	Subhedral-euhedral	37.5	0.12	0.03	2.0	0.4	25.9	33.8	99.9	1.2
LS1-13	Leslie	Rim	HK	Subhedral	37.2	0.17	0.01	2.1	0.4	25.3	34.6	99.7	1.1
LS1-13	Leslie	Core	HK	Subhedral	37.6	0.18	0.00	2.0	0.4	25.4	34.1	99.6	1.3
LS1-14	Leslie	Rim	HK	Subhedral-euhedral	37.5	0.16	0.01	2.2	0.4	25.4	33.9	99.7	0.9
LS1-14	Leslie	Core	HK	Subhedral-euhedral	37.3	0.14	0.05	2.2	0.4	25.6	34.0	99.7	0.9
LS1-15	Leslie	Rim	HK	Subhedral-rounded	37.2	0.00	0.02	2.4	0.5	25.2	33.8	99.2	0.5

Sample	Location	Type	Kimberlite facies[a]	Habit	SiO_2	TiO_2	Al_2O_3	FeO*[c]	MnO	MgO	CaO	Total	ΔNNO[b]
LS1-15	Leslie	Core	HK	Subhedral-rounded	37.0	0.11	0.02	2.1	0.4	25.3	34.4	99.4	1.1
LS1-16	Leslie	Rim	HK	Subhedral-anhedral rounded	36.6	0.11	0.04	2.1	0.4	25.3	34.5	99.0	1.0
LS1-16	Leslie	Core	HK	Subhedral-anhedral rounded	36.8	0.08	0.01	1.9	0.4	25.4	34.3	99.0	1.3
LS1-17	Leslie	Rim	HK	Euhedral	36.9	0.10	0.07	2.0	0.4	25.4	34.1	99.0	1.2
LS1-17	Leslie	Core	HK	Euhedral	37.7	0.09	0.03	2.1	0.3	25.4	34.6	100.1	1.2
LS1-18	Leslie	Rim	HK	Euhedral-subhedral	37.7	0.08	0.03	2.0	0.4	26.0	33.9	100.1	1.3
LS1-18	Leslie	Core	HK	Euhedral-subhedral	37.2	0.12	0.01	2.0	0.3	25.4	34.4	99.4	1.2
LS1-19	Leslie	Rim	HK	Subhedral	37.4	0.14	0.04	1.9	0.4	25.5	34.1	99.4	1.4
LS1-19	Leslie	Core	HK	Subhedral	37.2	0.09	0.02	1.9	0.3	25.2	34.4	99.2	1.4
LS1-20	Leslie	Rim	HK	Subhedral-euhedral	36.8	0.12	0.05	2.0	0.4	25.3	34.4	99.1	1.3
LS1-20	Leslie	Core	HK	Subhedral-euhedral	37.4	0.07	0.01	2.2	0.5	25.4	34.2	99.7	1.0
AVG Rim					37.3	0.10	0.03	2.1	0.4	25.5	34.1	99.5	1.1
STDEV					0.32	0.05	0.02	0.2	0.1	0.21	0.31	0.4	0.2
AVG Core					37.2	0.13	0.03	2.1	0.4	25.4	34.2	99.4	1.1
STDEV					0.34	0.05	0.02	0.1	0.1	0.25	0.29	0.5	0.2
AN2-1	Aaron	Core	HK	Anhedral-subhedral	37.5	0.06	0.00	2.4	0.3	25.2	34.4	99.9	0.5
AN2-2	Aaron	Core	HK	Anhedral	37.1	0.05	0.10	2.6	0.4	25.0	34.0	99.2	0.3
AN2-3	Aaron	Core	HK	Anhedral	37.8	0.13	0.04	2.7	0.3	25.3	34.1	100.3	0.2
AN2-4	Aaron	Core	HK	anhedral-subhedral	37.5	0.00	0.00	2.5	0.3	25.4	34.4	100.0	0.5
AN2-5	Aaron	Rim	HK	Subhedral-euhedral	37.2	0.06	0.02	2.4	0.4	25.1	34.2	99.2	0.6
AN2-5	Aaron	Core	HK	Subhedral-euhedral	37.0	0.01	0.00	2.2	0.4	25.1	34.4	99.2	0.8
AN2-6	Aaron	Core	HK	Subhedral-anhedral	37.5	0.10	0.00	2.5	0.3	25.0	34.6	99.8	0.4
AN2-7	Aaron	Core	HK	Subhedral	38.0	0.05	0.01	2.4	0.3	25.3	34.5	100.4	0.6
AN2-8	Aaron	Core	HK	Subhedral	37.9	0.01	0.01	2.4	0.3	25.2	34.3	100.2	0.6

Sample	Location	Type	Kimberlite facies[a]	Habit	SiO_2	TiO_2	Al_2O_3	FeO*[c]	MnO	MgO	CaO	Total	ΔNNO[b]
AN2-9	Aaron	Rim	HK	Subhedral	37.3	0.08	0.03	2.5	0.3	25.2	34.2	99.7	0.4
AN2-9	Aaron	Core	HK	Subhedral	37.5	0.06	0.03	2.4	0.4	25.3	34.1	99.8	0.5
AN2-10	Aaron	Core	HK	Subhedral	37.1	0.12	0.17	3.3	0.4	25.9	33.6	100.4	-0.7
AN2-11	Aaron	Rim	HK	Subhedral-anhedral	37.5	0.04	0.00	2.4	0.2	25.0	34.7	99.8	0.6
AN2-11	Aaron	Core	HK	Subhedral-anhedral	38.1	0.00	0.01	2.5	0.3	25.6	34.3	100.8	0.5
AN2-12	Aaron	Rim	HK	Subhedral-anhedral	37.7	0.01	0.02	2.4	0.2	25.0	34.4	99.8	0.6
AN2-12	Aaron	Core	HK	Subhedral-anhedral	37.9	0.03	0.02	2.4	0.3	25.2	34.4	100.2	0.6
AN2-13	Aaron	Rim	HK	Subhedral	37.4	0.05	0.00	2.4	0.3	25.0	34.3	99.4	0.6
AN2-13	Aaron	Core	HK	Subhedral	37.6	0.08	0.00	2.3	0.3	25.1	34.6	99.0	0.7
AN2-14	Aaron	Rim	HK	N.D.	37.7	0.03	0.01	2.4	0.3	25.4	34.4	100.1	0.6
AN2-14	Aaron	Core	HK	N.D.	38.0	0.00	0.04	2.7	0.3	25.1	34.0	100.1	0.2
AN2-15	Aaron	Rim	HK	Euhedral	37.7	0.08	0.00	2.4	0.3	25.4	34.4	100.2	0.6
AVG Rim					37.5	0.05	0.01	2.4	0.3	25.2	34.3	99.7	0.6
STDEV					0.2	0.02	0.01	0.1	0.0	0.2	0.2	0.4	0.1
AVG Core					37.6	0.05	0.03	2.5	0.3	25.3	34.3	100.0	0.4
STDEV					0.4	0.05	0.05	0.3	0.1	0.2	0.3	0.5	0.4
E-1	Elwin Bay	Rim	HK-TK	Subhedral	37.3	0.05	0.00	5.3	0.3	22.8	33.7	99.4	-3.3
E-1	Elwin Bay	Core	HK-TK	Subhedral	36.9	0.14	0.02	7.5	0.4	23.3	31.0	99.2	N.D.
E-2	Elwin Bay	Core	HK-TK	Subhedral	37.5	0.02	0.01	4.6	0.3	23.6	33.9	99.9	-2.1
E-3	Elwin Bay	Rim	HK-TK	Anhedral	37.5	0.05	0.04	6.0	0.3	23.0	32.7	99.6	-5.0
E-3	Elwin Bay	Core	HK-TK	Anhedral	37.3	0.02	0.03	6.0	0.3	22.8	32.6	99.0	-4.9
E-4	Elwin Bay	Rim	HK-TK	Euhedral	37.5	0.09	0.01	5.7	0.3	23.1	33.1	99.8	-4.1
E-4	Elwin Bay	Core	HK-TK	Euhedral	37.0	0.03	0.01	7.6	0.5	22.1	31.6	98.8	N.D.
E-5	Elwin Bay	Rim	HK-TK	Subhedral	36.5	0.33	0.02	7.8	0.4	21.4	32.6	99.0	N.D.
E-5	Elwin Bay	Core	HK-TK	Subhedral	37.1	0.13	0.04	7.6	0.4	22.5	31.6	99.3	N.D.

Sample	Location	Type	Kimberlite facies[a]	Habit	SiO_2	TiO_2	Al_2O_3	FeO*[c]	MnO	MgO	CaO	Total	ΔNNO[b]
E-6	Elwin Bay	Core	HK-TK	Subhedral-anhedral	36.9	0.10	0.04	7.9	0.4	22.5	31.3	99.1	N.D.
E-7	Elwin Bay	Rim	HK-TK	Anhedral	36.3	0.27	0.59	8.6	0.4	22.5	30.7	99.4	N.D.
E-7	Elwin Bay	Core	HK-TK	Anhedral	36.6	0.14	0.02	8.1	0.5	22.2	31.4	98.9	N.D.
E-8	Elwin Bay	Rim	HK-TK	Subhedral-euhedral	37.2	0.12	0.04	7.6	0.5	23.0	31.3	99.8	N.D.
E-8	Elwin Bay	Core	HK-TK	Subhedral-euhedral	37.1	0.00	0.03	6.7	0.4	22.7	32.4	99.3	-8.3
E-9	Elwin Bay	Rim	HK-TK	N.D.	37.1	0.05	0.04	8.1	0.4	22.5	30.8	99.0	N.D.
E-10	Elwin Bay	Rim	HK-TK	Subhedral	37.0	0.16	0.05	8.3	0.4	22.6	31.2	99.7	N.D.
E-10	Elwin Bay	Core	HK-TK	Subhedral	36.8	0.08	0.00	7.9	0.4	22.6	31.0	98.8	N.D.
E-11	Elwin Bay	Rim	HK-TK	Euhedral	37.5	0.14	0.02	5.9	0.3	23.7	32.1	99.6	-4.6
E-11	Elwin Bay	Core	HK-TK	Euhedral	37.1	0.09	0.02	7.4	0.3	21.8	32.8	99.5	N.D.
AVG Rim					37.1	0.14	0.09	7.0	0.4	22.7	32.0	99.5	
STDEV					0.5	0.10	0.19	1.3	0.1	0.6	1.1	0.29	
AVG Core					37.0	0.08	0.02	7.1	0.4	22.6	32.0	99.2	
STDEV					0.2	0.05	0.01	1.1	0.1	0.6	0.9	0.3	
GR9547-95-1	Grizzly	Core	HK	Anhedral	38.0	0.09	0.08	2.0	0.4	25.9	33.4	99.9	1.2
GR9547-95-2	Grizzly	Core	HK	Anhedral	38.1	0.05	0.01	3.0	0.3	24.2	34.3	100.1	-0.3
GR9547-95-3	Grizzly	Core	HK	Anhedral	37.8	0.07	0.06	2.5	0.4	24.8	33.5	99.1	0.5
GR9547-95-4	Grizzly	Core	HK	Anhedral	37.5	0.07	0.10	1.8	0.3	25.3	34.2	99.2	1.6
GR9547-95-5	Grizzly	Core	HK	Anhedral	37.7	0.05	0.08	1.7	0.4	25.4	34.0	99.4	1.7
GR9547-95-6	Grizzly	Core	HK	Anhedral	37.6	0.02	0.04	4.1	0.6	24.1	33.0	99.5	-1.8
GR9547-95-7	Grizzly	Core	HK	Anhedral	37.6	0.06	0.02	2.6	0.4	25.1	33.5	99.2	0.3
GR9547-95-8	Grizzly	Core	HK	Anhedral	37.4	0.05	0.00	3.4	0.4	24.5	33.3	99.1	-0.9
GR9547-95-9	Grizzly	Core	HK	Anhedral	37.4	0.11	0.03	4.3	0.6	24.1	33.1	99.5	-2.0
AVG Core					37.7	0.06	0.05	2.8	0.4	24.8	33.6	99.4	0.0
STDEV					0.3	0.03	0.04	1.0	0.1	0.7	0.5	0.3	1.4

[a] Kimberlite facies: HK: Hypabyssal kimberlite; HK-TK: Hypabyssal kimberlite-Tuffisitic kimberlite

[b] ΔNNO calculated with equation 3

[c] FeO* as FeO total

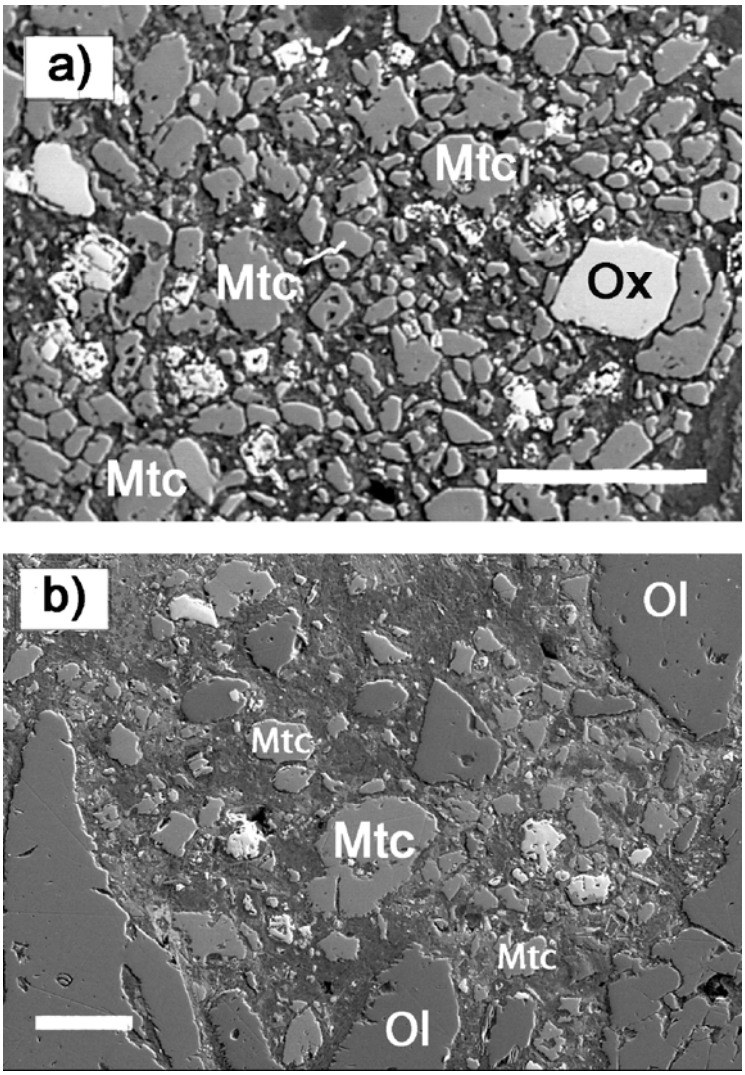

Figure 2.12. Plate-detector back-scattered images (PDBSE) of a) Abundant subhedral and anhedral monticellites (along with Fe-Ti-Mg oxides) set in a fine-grained matrix, Elwin Bay kimberlite. b) Subhedral and anhedral monticellites (along with olivine macrocrysts) set in a fine-grained matrix, Aaron kimberlite. Scale bar represents 800 µm in both images. Mtc= Monticellite; Ox= Fe-Ti-Mg Oxides; Ol= Olivine.

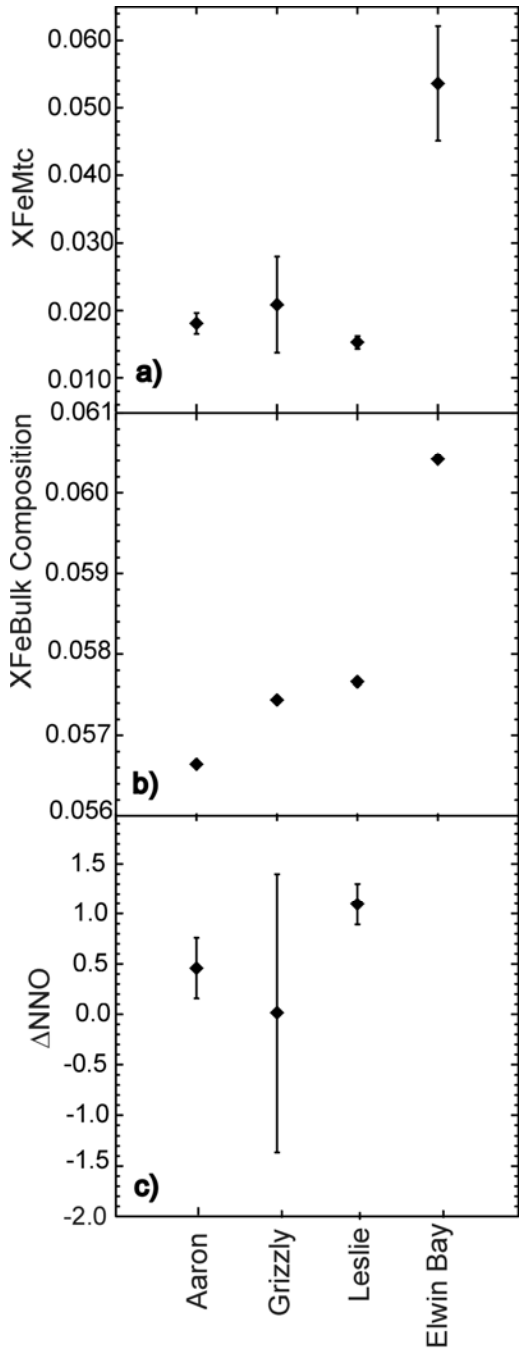

Figure 2.13. a) XFe of monticellite, b) XFe of the bulk composition and c) fO_2's (relative to the NNO buffer) calculated with equation 3 for monticellite data from my detail analysis of selected kimberlites. Error bars are ± 1 σ. Note that because of the complex zoning in Elwin Bay monticellites, the Fe-in-monticellite oxygen barometer cannot be applied to this kimberlite and gives spurious and non reliable results.

Table 2.5. Chemical analyses of perovskites (wt%), cations units and fO_2's calculated

Sample	CaO	TiO_2	FeO*[b]	Nb_2O_5	La_2O_3	Ce_2O_3	Nd_2O_3	Total
E-1	41.7	52.8	2.1	0.9	0.7	0.9	0.3	99.4
E-2	40.9	54.9	1.5	0.8	0.8	1.5	0.7	101.1
E-3	39.3	54.5	1.2	0.7	0.7	2.3	0.9	99.5
E-4	40.1	54.7	1.3	0.7	0.6	2.0	0.9	100.3
E-5	40.7	55.4	1.4	0.8	0.8	1.8	0.5	101.5
E-6	40.6	55.2	1.5	1.0	0.8	1.2	0.4	100.7
E-7	40.1	54.4	1.3	0.8	0.9	2.0	0.6	100.1
E-8	39.8	54.7	1.3	0.7	0.8	2.1	0.7	100.0
E-9	40.9	54.2	1.7	0.8	0.7	1.3	0.4	100.0
E-10	40.8	55.0	1.6	0.9	0.7	1.3	0.5	100.9
E-11	39.5	53.6	1.3	0.8	0.9	2.3	0.9	99.3
E-12-Rim	39.8	54.4	1.3	0.9	0.8	2.1	0.7	100.0
E-12-Core	39.3	54.5	1.2	0.8	0.8	2.3	0.9	99.8
E-13-Rim	39.3	54.3	1.2	0.7	0.9	2.5	0.9	99.7
E-13-Core	39.2	53.9	1.1	0.7	1.0	2.4	0.9	99.1
AVG Cores	39.9	54.3	1.4	0.8	0.8	2.0	0.7	99.9
STDEV Cores	0.7	0.5	0.2	0.1	0.1	0.5	0.2	0.6
GR9547-1	37.1	49.0	2.6	3.7	1.4	3.6	1.1	98.4
GR9547-2	37.2	49.2	2.7	2.7	1.5	3.8	1.1	98.2
GR9547-3	36.6	49.8	2.1	2.1	1.5	3.9	1.3	97.3
GR9547-4	36.3	49.6	2.1	2.3	1.4	4.0	1.2	96.9
GR9547-5	37.0	46.8	3.0	5.7	1.3	4.0	1.2	98.8
AVG	36.8	48.9	2.5	3.3	1.4	3.9	1.2	97.9
STDEV	0.4	1.2	0.4	1.4	0.1	0.1	0.1	0.8

Sample	Ca2+	Ti4+	Fe3+	Nb5+	La3+	Ce3+	Nd3+	Total cations	ΔNNO[a]
E-1	1.04	0.93	0.04	0.009	0.006	0.008	0.003	2.03	1.6
E-2	1.01	0.95	0.03	0.009	0.006	0.013	0.005	2.01	-1.5
E-3	0.98	0.96	0.02	0.007	0.006	0.020	0.007	2.01	-2.6
E-4	0.99	0.95	0.03	0.008	0.005	0.017	0.007	2.01	-2.0
E-5	1.00	0.95	0.03	0.009	0.007	0.015	0.004	2.01	-1.7
E-6	1.00	0.95	0.03	0.011	0.007	0.010	0.003	2.01	-1.5
E-7	1.00	0.95	0.03	0.008	0.008	0.017	0.005	2.01	-2.4
E-8	0.99	0.96	0.03	0.007	0.007	0.018	0.006	2.01	-2.1
E-9	1.01	0.94	0.03	0.009	0.006	0.011	0.003	2.02	-0.4
E-10	1.00	0.95	0.03	0.010	0.006	0.011	0.004	2.01	-1.1
E-11	0.99	0.95	0.03	0.008	0.008	0.020	0.008	2.01	-2.0
E-12-Rim	0.99	0.95	0.03	0.009	0.007	0.018	0.006	2.01	-2.2
E-12-Core	0.98	0.96	0.02	0.008	0.007	0.020	0.007	2.00	-2.8
E-13-Rim	0.98	0.96	0.02	0.007	0.008	0.021	0.008	2.01	-2.6
E-13-Core	0.99	0.95	0.02	0.008	0.008	0.021	0.007	2.01	-2.9
AVG Cores	1.00	0.95	0.03	0.008	0.007	0.017	0.006	2.01	-1.9
STDEV Cores	0.01	0.01	0.00	0.001	0.001	0.004	0.002	0.01	0.9
GR9547-1	0.96	0.89	0.05	0.040	0.012	0.032	0.010	2.00	0.5
GR9547-2	0.97	0.90	0.06	0.029	0.013	0.034	0.010	2.00	2.6
GR9547-3	0.96	0.91	0.04	0.023	0.013	0.035	0.011	2.00	0.5
GR9547-4	0.95	0.92	0.04	0.026	0.013	0.036	0.011	2.00	0.1
GR9547-5	0.96	0.85	0.06	0.063	0.012	0.035	0.010	1.99	-0.3
AVG	0.96	0.89	0.05	0.036	0.013	0.034	0.010	2.00	0.7
STDEV	0.01	0.03	0.01	0.016	0.001	0.001	0.000	0.00	1.1

[a] ΔNNO calculated with the Fe-in-perovskite (Bellis & Canil, 2007)

[b] FeO* as FeO total

(Lattavaram in Akella et al., 1979; Leslie in Armstrong et al., 2004; Kandalaksha in Beard et al., 1998; Gahcho Kué in Caro & Kopylova, 2004; Wajrakarur, Muligiripalle and Kotadonda in Chalapathi et al., 2004; De Beers, Dutoitspan and Mukorob in Mitchell, 1986; Elwin Bay in Mitchell, 1978; Churchill in Zurevinski, 2009). I assume a range of monticellite-melt Kd Fe^{2+}-Mg from 0.20 to 0.40.

The Mg# of primitive kimberlite melts in equilibrium with monticellite is large (Figure 2.14) although the Mg# of liquid within a given pipe is narrow (except for the Kotakonda kimberlite; cf., Table 2.6). Assuming a monticellite-melt Kd Fe^{2+}-Mg of 0.40, Lac de Gras kimberlites exhibit the highest Mg# of the melt (0.87-0.89) in this study. Amongst the Canadian kimberlites Elwin Bay and Gahcho Kué kimberlites show lower Mg# liquid in comparison to Churchill and Lac de Gras kimberlites. Indian kimberlites have a surprising low Mg# liquid in comparison to Lac de Gras and South African kimberlites. The lowest Mg# liquid is the Kotakonda kimberlite and reflects the very high Fe content of monticellite (20 wt%) trending toward kirschteinite. Note that the Kotakonda kimberlite contains kirschteinite in the groundmass which is not a common kimberlite mineral.

It is difficult to compare the estimates obtained in this study with previous estimates because the majority of the studies have expressed the Mg# of kimberlite melts as Mg/(Mg+total Fe). Nonetheless, if one can assume very little Fe^{3+} in melts, previous estimates for Lac de Gras kimberlites (0.86 – 0.88) are similar to my estimates (Kjarsgaard et al., 2009; Kopylova et al., 2007) whereas South African kimberlite (De Beers and Dutoitspan) estimates are slightly higher (0.82-0.87) than those calculated from monticellite compositions (Becker & Le Roex, 2006; Harris et al., 2004; Le Roex et

al., 2003. I also show on Figure 2.14a the estimates of the Mg# (Mg/(Mg+total Fe) of Majuagaa and Udachnaya-E kimberlite melts (Nielsen & Sand, 2008; Kamenetsky et al., 2009).

As noted by Kopylova et al. (2007) it is unlikely that very magnesian melts such as those from Lac de Gras or Churchill (Table 2.6) could be in equilibrium with a typical mantle with Fo_{90} olivine. Either such magmas were derived from an ultra-refractory mantle, or the olivine-liquid Kd Fe-Mg during melting is higher than hitherto assumed (Girnis et al., 2005). On the other hand, South African (De Beers and Dutoitspan), Elwin Bay, Kandalaksha and Indian kimberlites are likely in equilibrium with typical mantle olivine.

The large variation in the Mg# of kimberlitic melts suggests that the mode of generation or differentiation of kimberlites differs from region to region. Kimberlites can be generated at different depths (asthenosphere to subcontinental lithospheric mantle), from different sources, and can reflect different degrees of melting and variable oxygen fugacity. Melting at higher fO_2 could lower the Mg# (Mg/(Mg+Fe*) of the liquid because most mantle minerals (orthopyroxene and olivine) accommodate mainly Fe^{2+} in their structure and thus melting would enrich the melt with respect to Fe. Kimberlites are thought to be derived from a small degree melting in the asthenospheric mantle but other models invoke heterogeneous sub-continental lithospheric mantle (Chalapathi et al., 2004, 2009) or even subducted ocean crust (Paton et al., 2009), for the source of kimberlite melt.

Evolved kimberlites have been recognized, such as Wemindji (Zurevinski & Mitchell, 2011), Wesselton (Le Roex et al., 2003) and the Benfontein sills (Dawson &

Hawthorne, 1973), but do not contain monticellite in the groundmass. Assimilation of mantle and crustal xenoliths by the magma (which can be difficult to distinguish because of the opposing effect on the magma composition) can also modify the composition of the primary magma during ascent. Consequently, monticellites crystallized at low pressure would display compositions that have been affected by chemical changes of the magma.

I note that both Proterozoic and Cambrian kimberlites from India and Canada exhibit a low Mg# of the melt whereas Jurassic, Cretaceous and Eocene kimberlites have a higher Mg#, suggesting some broad possible geographic and/or temporal changes in the formation or differentiation of kimberlite liquids. More studies of well-preserved, 'uncontaminated' monticellite-bearing kimberlites on a pipe, field and province wide scale may reveal more specific explanations of the variations of Mg# of kimberlite melts associated with each region.

2.7 Conclusions

I calibrated a new oxygen barometer using Fe in monticellite. Weighted least-squares regression of data from monticellite crystallized between 1230 and 1350°C and from NNO -4.1 to +5.3 gives the relationship

$$\Delta NNO = \frac{\left\{\log\left[0.858(\pm 0.021)\frac{X_{Fe}^{liq}}{X_{Fe}^{Mtc}} - 1\right] - 0.139(\pm 0.022)\right\}}{0.193(\pm 0.004)}$$

Application to five kimberlites from several localities revealed a wide fO_2 range from NNO-3.5 to NNO+1.7. The fO_2 values determined with the Fe-in-monticellite are within uncertainties with those determined with the Fe-in-perovskite suggesting that the Fe-in-monticellite can be used as a reliable oxygen barometer when perovskite is absent from a

kimberlite. I recommend using the Fe-in-monticellite only in fresh hypabyssal kimberlites. Estimations of the primitive kimberlite compositions from monticellite compositions suggest a wide range of Mg# liquid reflecting that kimberlite magmas are generated under different conditions and/or from different sources.

Table 2.6. Mg# of kimberlite melts calculated from monticellite compositions for different monticellite-melt Kd Fe^{2+}-Mg

Kimberlite pipe	n	Kd=0.4	STDEV (1σ)	Kd=0.3	STDEV (1σ)	Kd=0.2	STDEV (1σ)
Kotakonda	2	0.50	0.22	0.44	0.21	0.35	0.20
Muligiripalle	3	0.59	0.10	0.52	0.10	0.42	0.10
Wajrakarur-4/PR2[a]	2	0.62	0.05	0.55	0.05	0.45	0.05
Wajrakarur-7/PR2[a]	2	0.70	0.03	0.64	0.03	0.54	0.03
Lattavaram	1	0.66	N.D.	0.59	N.D.	0.49	N.D.
Gahcho Kué	1	0.62	N.D.	0.55	N.D.	0.45	N.D.
Kandalaksha	2	0.66	0.00	0.59	0.00	0.49	0.00
Elwin Bay[a]	28	0.71	0.05	0.65	0.06	0.56	0.07
Dutoitspan	2	0.78	0.07	0.73	0.09	0.64	0.10
De Beers	2	0.80	0.07	0.75	0.08	0.67	0.09
Mukorob	2	0.83	0.03	0.79	0.03	0.71	0.04
Churchill-CD20-24	27	0.84	0.04	0.80	0.04	0.73	0.05
Churchill-JBP16	41	0.87	0.01	0.83	0.02	0.77	0.02
Grizzly	9	0.86	0.04	0.83	0.05	0.76	0.07
Aaron	21	0.88	0.01	0.85	0.01	0.78	0.01
Leslie	42	0.90	0.01	0.87	0.01	0.82	0.01

[a] Mg# of kimberlite melts ($Mg/(Mg+Fe^{2+})$) represents an average including rims and cores

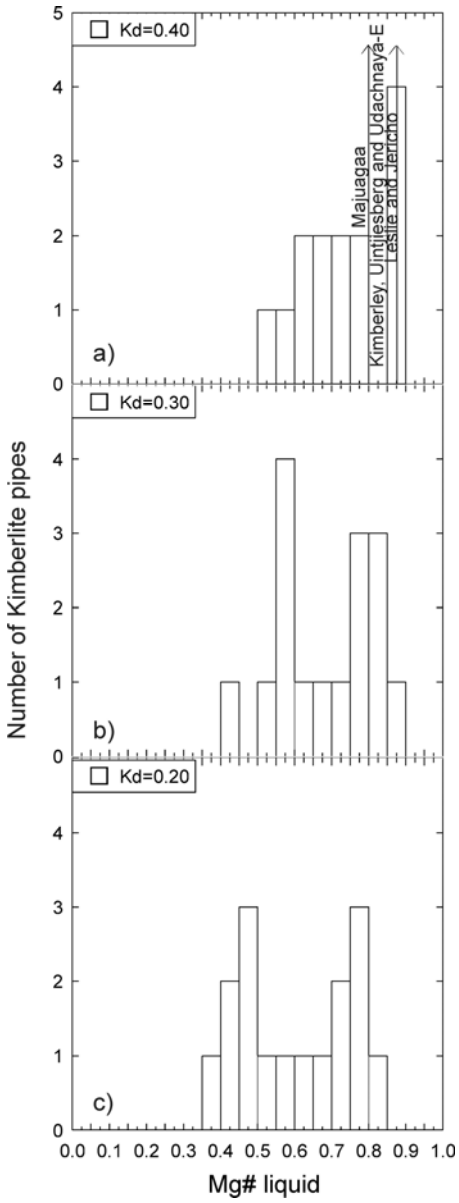

Figure 2.14. a), b) and c) Mg# of kimberlite melts (Mg/(Mg+Fe^{2+})) from monticellite compositions for all kimberlite pipes studied calculated with a monticellite-melt Kd Fe^{2+}-Mg of 0.40, 0.30 and 0.20 respectively. Note the wide range of Mg# liquid of kimberlites. The Mg# of kimberlite melts have been averaged for each kimberlite pipe, including rims and cores (Elwin Bay and Wajrakarur pipes). Sources of data for the Mg# of the melts (Mg/(Mg+total Fe)) from the Lac de Gras, Jericho, South African Gp 1, Kimberley, Udachnaya-E and Majuagaa kimberlites: Kjarsgaard et al., 2009; Kopylova et al., 2007; Becker a& Le Roex, 2006; Le Roex et al., 2003; Kamenetsky et al., 2009; Nielsen & Sand, 2008 respectively.

Chapter 3
Partitioning of Vanadium between monticellite and liquid

3.1 Introduction

The partitioning of V between crystals and liquids is of great interest because of the potential of V to constrain the redox state of mantle-derived magmas (Canil, 1997, 1999, 2002; Lee et al., 2003, 2005; Mallmann & O'Neill, 2009). The interest in modeling the behavior of V between silicate minerals and liquids is that V is immune to post-igneous changes because of its low mobility during alteration and metamorphism (Canil, 2002) and thus serves as an incredibly useful tool to describe fO_2 of magmas. An understanding of the behavior of V in terrestrial magmas allows the calculation of the fO_2 of magmas for which conventional methods using the Fe redox (Kilinc et al., 1983; Kress & Carmichael, 1988; Sack et al., 1980) or oxide phenocrysts (Carmichael, 1991) would be impossible to apply.

The oxidation state of V in terrestrial melts have been constrained previously in a series of partitioning experiments on mafic and ultramafic compositions and found to be of several different valence states including V^{3+}, V^{4+} and V^{5+} (Borisov et al., 1987; Canil, 1997, 1999; Mallmann & O'Neill, 2009; Sutton et al., 2005; Toplis & Corgne, 2002). The oxidation of V in melts can be described by two redox equations:

$$V^{3+}O_{1.5} + \tfrac{1}{4}\, O_2 = V^{4+}O_2 \qquad (1)$$

$$V^{4+}O_2 + \tfrac{1}{4}\, O_2 = V^{5+}O_{2.5} \qquad (2)$$

with the respective equilibrium constants:

$$K_{(1)} = [V^{4+}O_2]/([V^{3+}O_{1.5}]*(fO_2)^{0.25}) \qquad (3)$$

and

$$K_{(2)} = [V^{5+}O_{2.5}]/([V^{4+}O_2]*(fO_2)^{0.25}) \qquad (4)$$

where [ ] is the activity of the given V species. The increase in V^{4+} species in melts above NNO-3 is responsible for the decreasing $D_V^{crystal/liquid}$ because most minerals prefer V^{3+} in their crystal structure, although little V^{4+} can enter into the clinopyroxene and titanomagnetite structure at high fO_2 (cf., Toplis & Corgne, 2002; Mallmann & O'Neill, 2009). Furthermore, Toplis & Corgne (2002) demonstrated that V^{5+} increases significantly above NNO-3 and becomes dominant at fO_2 above NNO+2.

The partitioning of V between crystal and liquid (e.g., olivine, clinopyroxene, orthopyroxene, spinel and garnet) in mafic and ultramafic compositions has been applied to peridotites and mafic and ultramafic rocks such as picrites and komatiites in order to model the fO_2 during partial melting of the mantle to form magmas (Canil & Fedortchouk, 2000, 2001; Canil, 1997, 1999). Canil (1997) used the $D_V^{Ol/liq}$ to show that Achaean komatiite flows are as oxidized as present day ocean basalts. Toplis & Corgne (2002) used V oxygen barometry to investigate the V concentrations in magnetite in the Bushveld intrusion at 100kPa and found that economic V concentrations in magnetite (> 1.5 wt% V_2O_5) can be observed between NNO and NNO-1.5. Mallmann & O'Neill (2009) modeled the change in the partitioning coefficients of all V species (namely D_{V2+}, D_{V3+}, D_{V4+}, D_{V5+}) covering the entire range of fO_2 in the solar system (NNO-12.5 to NNO +12.2) at 1300°C and 100kPa as well as at 1315-1450°C and 1-3 GPa, and calculated the fO_2 of mantle-derived magmas such as MORB's (Mid-Ocean-Ridge Basalts), OIB's (Ocean Island Basalts) and IAB's (Island Arc Basalts). The results of their study showed that the fO_2 of MORBs, OIBs and IABs are indistinguishable from

one another. They attributed the more oxidized nature of IAB's calculated from the Fe^{3+}/Fe^{2+} ratio to subsequent alterations changing the bulk composition of the rock.

V-based oxygen barometry has never been applied to kimberlite magmas but could provide information on their fO_2 and its petrological relevance for these complex and often altered magmas. This approach could be used when other methods to study the fO_2 of kimberlite magmas, such as oxide phenocrysts (Carmichael, 1991), the Fe-in-perovskite (Bellis & Canil, 2007) and/or the Fe-in-monticellite oxygen barometers cannot be used due to the lack of oxides, perovskite or to alteration processes that change the bulk composition of kimberlites.

Although olivine is the most common mineral in kimberlite, its origin as a phenocryst or xenocryst in this rock type is still a subject of debate (Arndt et al., 2010; Brett et al., 2009; Patterson et al., 2009) and thus the application of the $D_V^{Ol/liq}$ is dubious. In contrast, monticellite is a common liquidus mineral and is germane to the kimberlite magma, crystallizing at low pressure. To this end, I investigate the V partitioning between monticellite and synthetic kimberlite liquid at fO_2 between NNO-4 and NNO+5 (where NNO is the Nickel-Nickel-Oxide buffer) at 100 kPa, at 1280 and 1350°C and calibrate a new oxygen barometer. I assume that monticellite accommodates only V^{3+} in its structure, like the majority of minerals, because V^{4+} and V^{5+} are incompatible. It is then expected that $D_V^{Mtc/liq}$ will decrease with fO_2 if the melt is composed of variable V oxidation states.

3.2 Methods

3.2.1 Analytical methods

Vanadium in both monticellite and glass in experimental run products was analyzed by laser ablation inductively coupled plasma mass spectrometry (LA-ICP-MS)

using a NewWave Geolase™ UP-213 (Nd-YAG UV laser) at the University of Victoria in order to compare the results by EMP. Calibration was performed using NIST 611 and 613 glass standards. External standards (NIST 611 and NIST613) were measured every 8 to 10 analyses. ^{43}Ca was used as an internal standard, based on the EMP measurements of CaO. Analyses were made in gated Q-switch mode for optimum stability with a pulse rate of 10Hz. I acquired 30-s of background signal followed by 45-s ablation signal. Laser ablation was done in a rastered mode at a speed 10-12µm/sec along three passes, using a spot diameter of 25 µm for monticellite and 30µm for glass. Data reduction was performed offline in Excel. For each run product, three to four rastered areas were analyzed both on monticellite and glass. Uncertainties at 1 σ for V in monticellite are less than 15% except for one case reaching 30%. The uncertainties may represent either contamination from mineral inclusions (rare) or crystal thickness. I ruled out the possibility of glass contamination by looking at the laser traces under the polarized microscope. Because of the small crystal size at 1350°C, I only measured the concentrations of V in the margins of monticellite crystals at 1280°C more likely in equilibrium with the melt at the time of quenching. The concentrations of V in monticellites and glasses are presented in Appendix A.

3.3 Results

Comparison of the V concentrations of monticellite obtained by EMP and LA-ICP-MS for run products of the MON1 composition (Figure 3.1) showed that the V concentrations determined by EMP are consistently higher (by about 40 ppm) and have larger uncertainties than those by LA-ICP-MS. I used the more precise V concentrations determined by LA-ICP-MS for the $D_V^{Mtc/liq}$ calculations. In contrast, I used the

concentrations of V in glasses by EMP because the V levels in NIST standards used in the LA-ICP-MS calibration were a factor of ten lower than in my run product glasses making the extrapolation of the glass calibration difficult.

The $D_V^{Mtc/liq}$ is constant after 24 hours (Figure 3.2), suggesting that equilibrium is achieved in this run duration. The vanadium concentrations in glasses for all starting materials in function of fO_2 are illustrated on Figure 3.3. The concentrations of MON3 and WC3 are constant and similar along the fO_2 range studied. The V concentrations in MON1 and WC decrease above NNO-2.0 and will be discussed in the next section. Both V in monticellite and $D_V^{Mtc/liq}$ decrease with fO_2 as depicted on Figures 3.4 and 3.7.

3.4 Discussion

3.4.1 V^{5+} species in the melt phase

I estimated the concentration of V^{5+} species relative to those of V^{4+} and V^{3+} in the melt phase at each temperature as a function of the fO_2 using the approach of Mallmann & O'Neill (2009). I regressed all my experimental data according to their equation 15 with a non-linear weighted least square regression and assumed that no V^{2+} is present in the melt at the fO_2 range investigated in this study (Figure 3.5). I assume a constant K'_{hom} at both 1280 and 1350°C, implying that the equilibrium constant does not vary with the melt composition over the fO_2 range studied. Parameters obtained from the regressions (equilibrium constants and D_{V3+}, D_{V4+} and D_{V5+} between monticellite and coexisting melt) are presented in Table 3.1. The concentrations of the V^{5+} species relative to those of V^{4+} and V^{3+} are calculated from the equilibrium constants (including the activity coefficients) of each redox equation obtained from the two regressions (Table 3.2).

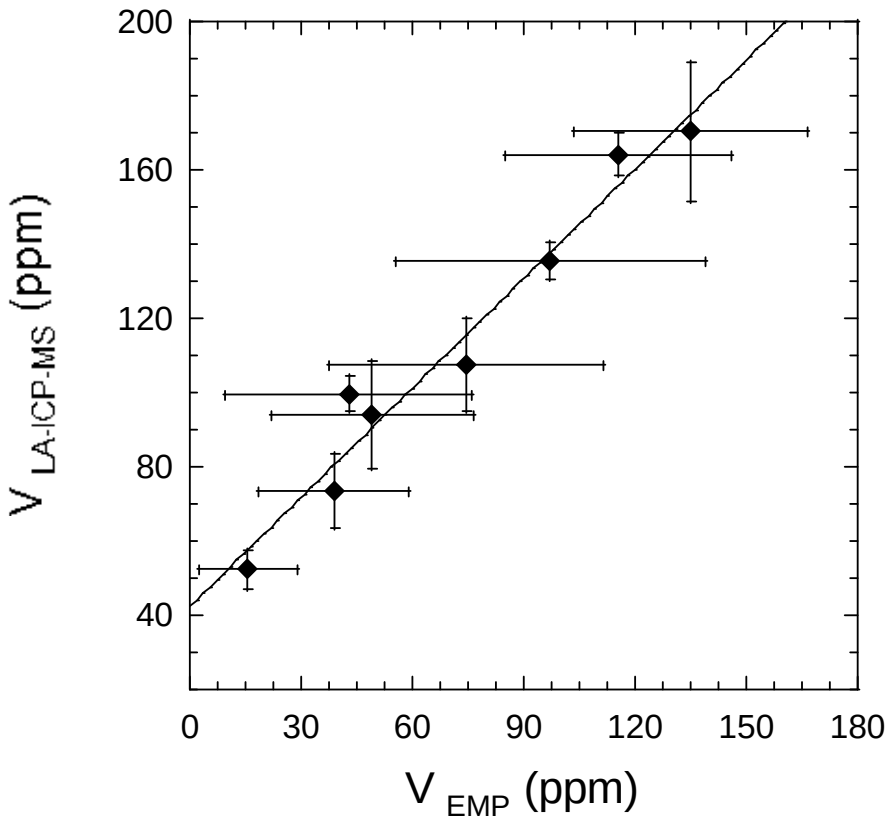

Figure 3.1. Comparison between V concentrations in monticellite by LA-ICP-MS and EMP. Note the large error bars on the EMPA. Equation for the linear regression is: V_{ICP}=0.982(0.081)*V_{EMP}+42.31(6.58). R^2=0.96. Error bars are ± 1σ.

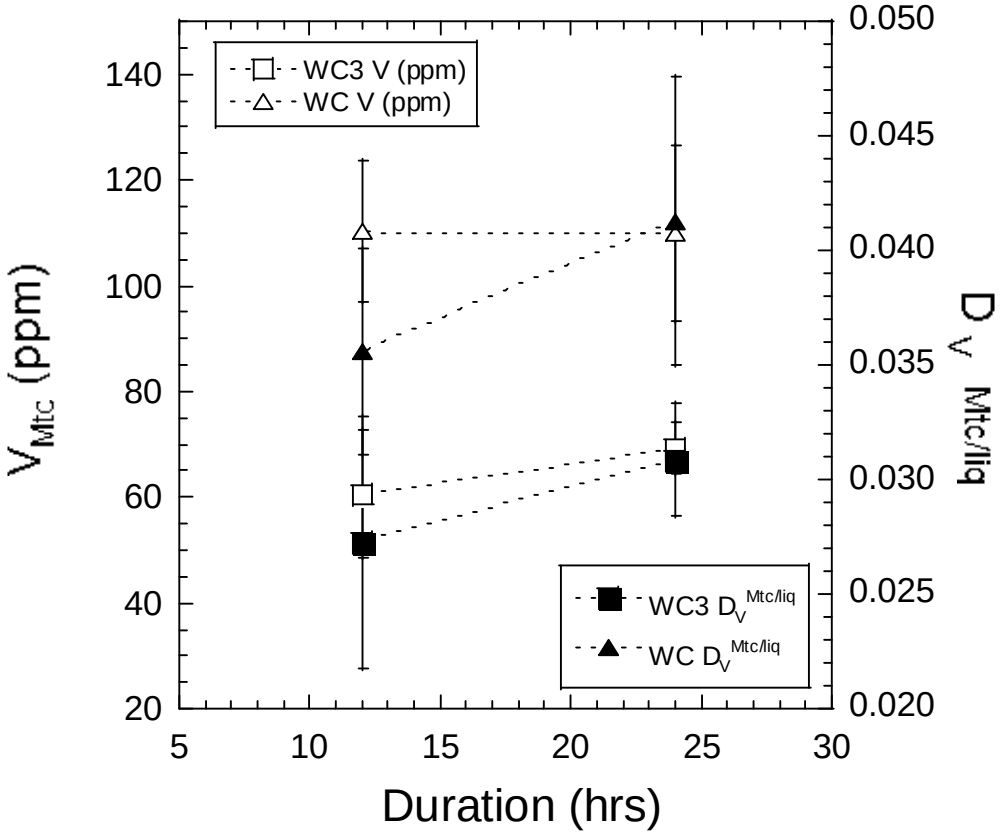

Figure 3.2. Time series experiments on WC and WC3 compositions with respect to the V in monticellite. Equilibrium is suggested after 24 hours according to the $D_V^{Mtc/liq}$. Error bars are ± 1σ.

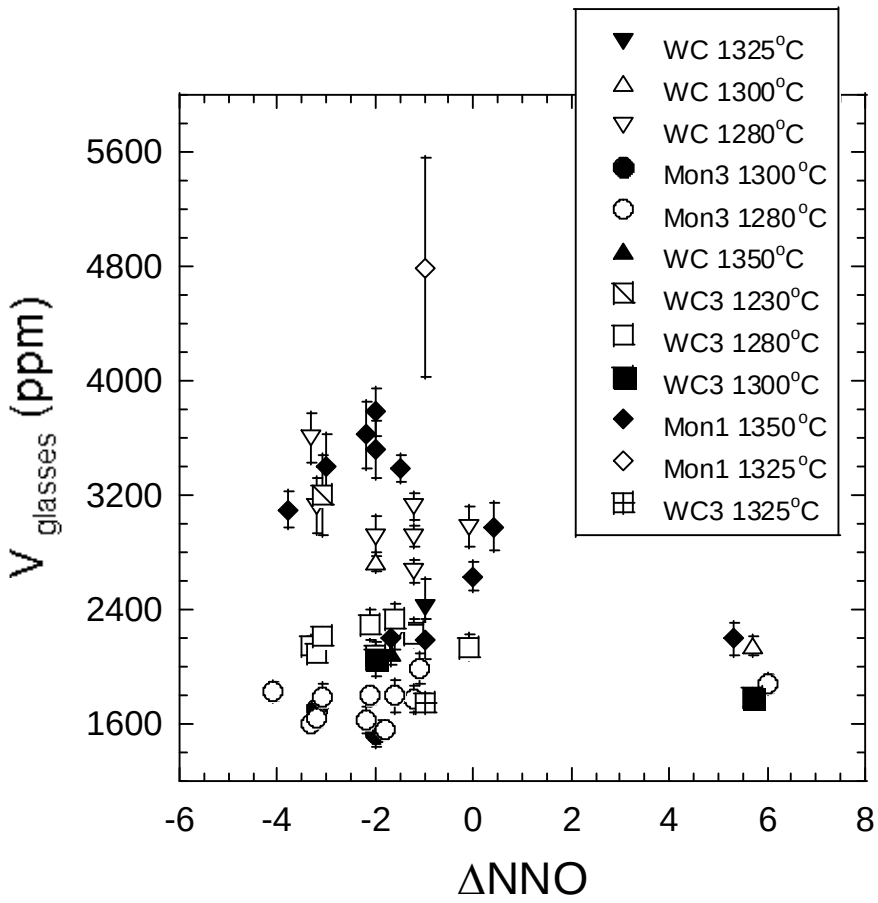

Figure 3.3. Vanadium concentrations in glasses in equilibrium with monticellite. Constant concentrations are observable in MON3 and WC3 (1280°C) compositions but not in WC and Mon1 (at 1280°C and 1350°C respectively). Error bars are ± 1σ.

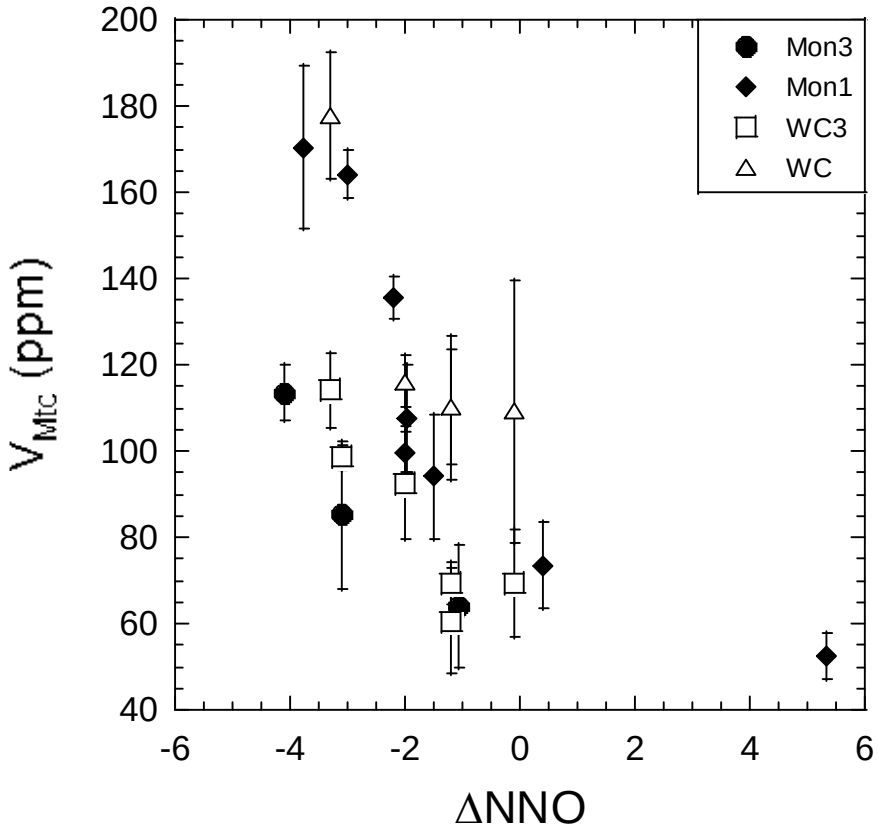

Figure 3.4. Vanadium concentrations in monticellite in function of fO_2 relative to the NNO (ΔNNO = log fO_2 of experiments- log fO_2 of the NNO buffer). Error bars are ± 1σ.

The proportion of V^{5+} and V^{4+} species at both temperatures are nearly identical at log fO_2 of -6.0 (i.e., NNO 0 at 1350°C and NNO+0.7 at 1280°C) whereas above that fO_2 V^{5+} dominates in my experimental liquids. The proportions of V^{4+} and V^{3+} species at 1280°C and 1350°C are identical at log fO_2 of -12.0 and -9.0 respectively corresponding to NNO-5.3 at 1280°C and NNO-3.0 at 1350°C. These results are in agreement with Toplis & Corgne (2002) who found that V^{4+} species dominate above NNO-6.0. My results however suggest that V^{5+} dominates at NNO 0 at both temperatures contrarily to Toplis & Corgne (2002) whose experiments on a ferrobasaltic composition at 1068°C suggested that V^{5+} species dominates at NNO above +2.0. This divergence can be due either to temperature, bulk composition effect or differences in the two methods used to calculate the different oxidation states of V in melts. Based on my analysis of V speciation, I do not further consider the D_V of the experiment at NNO+5.3 because the concentrations of V^{5+} in the melt at this high fO_2 are significant and can lead to important errors in the regression of D_V if I only assume V^{3+} and V^{4+} in the melt phase.

3.4.2 V Substitution Mechanism in Monticellite

The V substitution in monticellite structure is complex. V cations show a weak correlation with Mg^{2+} and the proportion of tetrahedral (1-Si^{4+}) cations (Figure 3.6). This suggests a possible substitution of V on the M1 octahedral site and tetrahedral site (the tetrahedral substitution is observed in only MON3, WC3 and WC at 1280°C) according to either:

$$V^{3+}\,(M1) + V^{3+}(Tet) == Mg^{2+}\,(M1) + Si^{4+}\,(Tet) \quad (5)$$

for V^{3+} alone, or:

$$V^{2+}\,(M1) + V^{4+}\,(Tet) == Mg^{2+}\,(M1) + Si^{4+}\,(Tet) \quad (6)$$

Table 3.1. Parameters obtained by fitting the V partitioning between monticellite and liquid data to Mallmann & O'Neill's equation 15 (2009).

Experiments at 1280°C		
Equilibrium Constants		
$[K'hom(a)]^{-1}$	3.2×10^{-5}	9.9×10^{-4}
$[K'hom(b)]^{-1}$	3.0×10^{-2}	1.1
Monticellite (MON3, WC3, WC)		
D_{V3+}	1.3×10^{-1}	4.6×10^{-1}
D_{V4+}	2.1×10^{-2}	2.5×10^{-2}
D_{V5+}	4.0×10^{-2}	3.5×10^{-1}
R^2	0.9	
Experiments at 1350°C		
Equilibrium Constants		
$[K'hom(a)]^{-1}$	1.5×10^{-4}	2.4×10^{-4}
$[K'hom(b)]^{-1}$	2.7×10^{-2}	1.5×10^{-1}
Monticellite (MON1)		
D_{V3+}	8.9×10^{-2}	1.1×10^{-1}
D_{V4+}	1.3×10^{-3}	6.8×10^{-2}
D_{V5+}	2.6×10^{-2}	4.0×10^{-3}
R^2	0.9	

Table 3.2. Evaluation of V^{5+} species concentrations in the melt relative to V^{3+} and V^{4+} species in function of the fO_2 from the equilibrium constant, K'_{hom}, derived from Mallmann & O'Neill's regressions for each redox equation.

log fO_2	$[V^{5+}/V^{3+}]_{1280°C}$	$[V^{5+}/V^{4+}]_{1280°C}$	$[V^{4+}/V^{3+}]_{1280°C}$	$[V^{5+}/V^{3+}]_{1350°C}$	$[V^{5+}/V^{4+}]_{1350°C}$	$[V^{4+}/V^{3+}]_{1350°C}$
-12	0.03	0.03	0.93	0.01	0.04	0.18
-11	0.10	0.06	1.66	0.02	0.07	0.32
-10	0.31	0.11	2.95	0.07	0.12	0.58
-9	0.99	0.19	5.25	0.21	0.21	1.02
-8	3.15	0.34	9.34	0.67	0.37	1.82
-7	9.95	0.60	16.60	2.12	0.66	3.24
-6	31.46	1.07	29.52	6.72	1.17	5.76
-5	99.47	1.89	52.50	21.24	2.07	10.25
-4	314.56	3.37	93.37	67.16	3.69	18.22
-3	994.74	5.99	166.03	212.38	6.55	32.41
-2	3145.64	10.65	295.25	671.59	11.65	57.63
-1	9947.40	18.95	525.03	2123.76	20.72	102.48
0	31456.43	33.69	933.66	6715.92	36.85	182.23

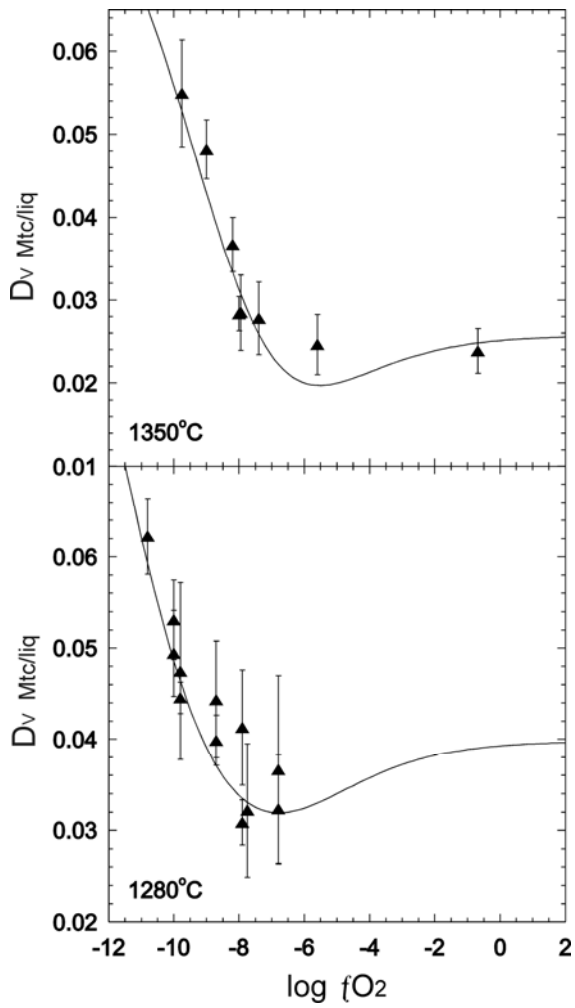

Figure 3.5. Non-linear least square regression of all data including NNO+5.0 at 1280°C and 1350°C in function of the log fO_2. The equation of the regression can be found in Mallmann & O'Neill (2009) assuming only V^{3+}, V^{4+} and V^{5+} in the melt phase:

$$D_{\Sigma V}^{c/m} = \frac{\left[D_{V^{3+}} * fO_2^{-1/2} * k'^{-1}_{\text{hom }(b)}\right] + \left[D_{V^{4+}} * fO_2^{-1/4} * k'^{-1}_{\text{hom }(c)}\right] + \left[D_{V^{5+}}\right]_{crystal}}{\left[fO_2^{-1/2} * k'^{-1}_{\text{hom }(b)}\right] + \left[fO_2^{-1/4} * k'^{-1}_{\text{hom }(c)}\right] + 1}$$

The $[V^{5+}/V^{3+}]$, $[V^{5+}/V^{4+}]$, and $[V^{4+}/V^{3+}]$ ratios are calculated from $K'_{hom(a)}$= $([V^{5+}O_{2.5}]/[V^{3+}O_{1.5}])*(fO_2)^{-1/2}$ and $K'_{hom(b)}$= $([V^{5+}O_{2.5}]/[V^{4+}O_2])*(fO_2)^{-1/4}$. Parameters obtained from the V partitioning regression and $[V^{5+}]$ relative to $[V^{4+}]$ and $[V^{3+}]$, where [ ] is the concentration of a given species, can be found in Table 3.1 and Table 3.2 respectively. Error bars are ± 1σ.

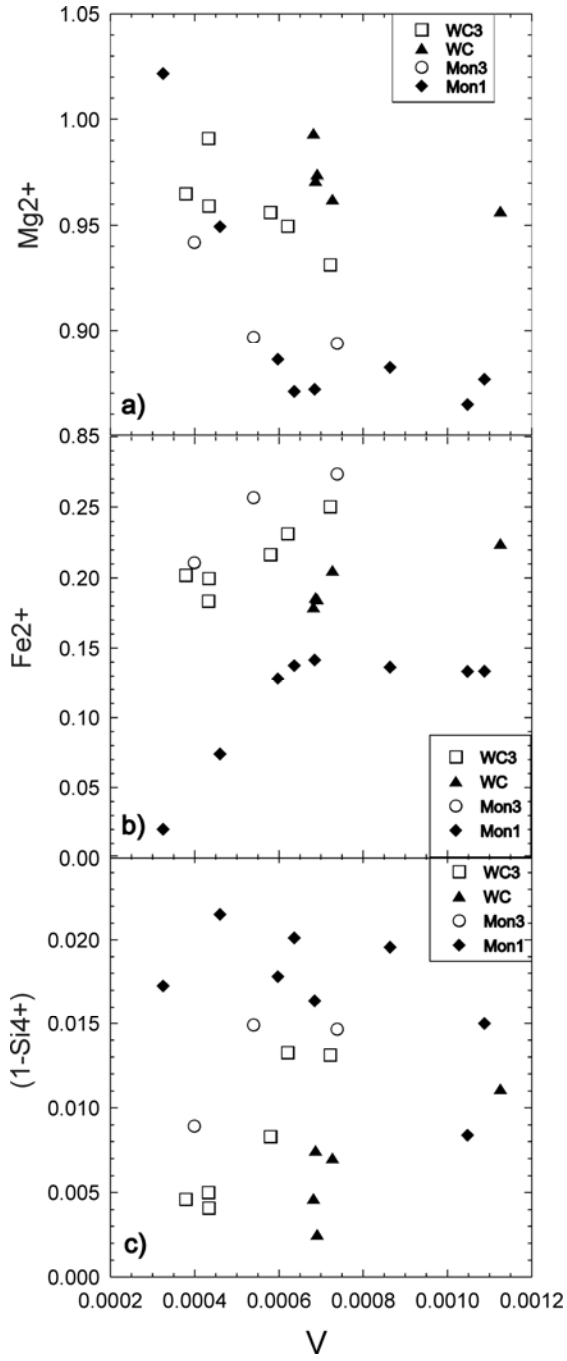

Figure 3.6. Substitution mechanism in monticellite. a) Correlation between Mg^{2+} and V^{3+} cations (and with fO_2) b) Positive correlation between Fe^{2+} and V^{3+} cations in monticellite c) Tetrahedral substitution of V in WC3, WC and Mon3 only.

for a mixture of V^{2+} and V^{4+} in the monticellite structure. Note that I assume that little to no V^{2+} is present in my experimental melts at the fO_2 range studied. Any simple substitution to maintain charge balance (e.g., $3Mg^{2+}$ - $2V^{3+}$) would require a site vacancy and/or the creation of a crystal defect. The partitioning of V into monticellite might be a defect and/or a site vacancy mechanism. The vanadium cations in monticellite structure are positively correlated to the total excess cations (based on 3 cations in olivine) in MON3, WC3 and WC (except in MON1). No relationship between V and Ca^{2+} were observed and thereby no V enters the M2 octahedral site. Fe^{2+} cations and V cations are positively correlated in all compositions, and this relationship is related to changes in fO_2 which is consistent with the V^{3+} and V^{4+} exchange. With increasing fO_2, V^{4+} and Fe^{3+} increase in the melt at the expense of V^{3+} and Fe^{2+}.

3.4.3 Influence of fO_2, T and bulk composition on the vanadium partitioning between monticellite and liquid

The oxygen fugacity is the strongest intensive variable in controlling $D_V^{Mtc/liq}$. The different trends in the V concentrations of glasses are due to variations in the phase assemblage of different compositions with fO_2 and T although, as mentioned above, fO_2 does not play a major role in the phase assemblage except at high fO_2. The decreasing V concentrations in MON1 and WC glasses with increasing fO_2 reflect the increase in the amount of FeTi oxides on the liquidus with fO_2. The V concentrations in glasses are slightly affected by the V concentrations in the bulk composition; for example, the lower V concentrations in MON3 in comparison to WC3 at the same temperature. The higher V concentrations in WC in comparison to WC3 and MON3 at 1280°C reflect the small melt fraction in WC and the incompatible character of V. It is assumed that vanadium

concentrations are sufficiently diluted in monticellite and glass to obey Henry's law (cf., Canil, 1997; Canil & Fedortchouk, 2000).

For all compositions, the V concentrations in monticellite and the $D_V^{Mtc/liq}$ decrease with increasing fO_2 (Figures 3.4. and 3.7). This implies that if V^{4+} and V^{5+} are present in the melt they do not substitute into monticellite and do not influence the value of $D_V^{Mtc/liq}$ over the fO_2 range studied. Olivines prefer V^{3+} in their structure (Canil & Fedortchouk, 2001) and as a consequence V_{Mtc} and $D_V^{Mtc/liq}$ decrease as fO_2 increases. Note that $D_V^{Mtc/liq}$ includes $D_{V3+}^{Mtc/liq}$, $D_{V4+}^{Mtc/liq}$ and $D_{V5+}^{Mtc/liq}$. I do not consider any V^{5+} partitioning into monticellite because the higher-charged cations are less compatible than lower-charged cations. Because of the differences in the phase assemblage and temperature of experiments (and thus in the V concentrations of glasses), the V concentrations in monticellite from different compositions differ with one another at constant fO_2. The $D_V^{Mtc/liq}$ are, however, within uncertainty of each other at identical fO_2. Note that V_{Mtc} and $D_V^{Mtc/liq}$ show little variation above NNO-2.0 in all compositions suggesting a change in the V oxidation state in the melt, as reflected in the Mallmann & O'Neill's regression coefficients. That is, the proportion of V^{3+} and V^{4+} are nearly the same at NNO-3.0 (Table 3.2) and above NNO-2 less V^{3+} is available in the melt to partition into monticellite.

Bulk composition and temperature have a minor to no influence on the variance of $D_V^{Mtc/liq}$ as observed by the constancy of the V partitioning coefficient at NNO-3.0 in all starting materials. More analyses are, however, required at constant composition and lower T (below 1280°C) and at constant fO_2 and T to confirm a temperature and bulk composition dependence over the fO_2 range studied.

3.5 Calibration of an oxybarometer for kimberlite magmas

I fitted an weighted least squares linear regression to all monticellite saturated compositions (n=21) synthesized in all starting materials (MON1, WC, MON3, WC3) between 1280 and 1350°C over a range of fO_2 from NNO-4.1 to NNO+0.5 where V^{3+} and V^{4+} are the inferred dominant V redox states. I excluded the experiment at NNO+5.3 due to evidence for a high V^{5+} concentration in the melt (see discussion above). The least square linear regression follows that of Roeder & Reynolds (1991) originally conceived for the Cr^{2+}-Cr^{3+} redox but adapted here for the V redox (Figure 3.7) and gives the following empirical relationship:

$$\Delta NNO = \frac{\left\{\log\left[0.354(\pm 1.785)\frac{V^{liq}}{V^{Mtc}} - 1\right] - 1.172(\pm 2.302)\right\}}{0.111(\pm 0.071)} \qquad (7)$$

I obtain a b value of 0.11, which is lower than the 0.25 expected for the V^{3+} and V^{4+} change in magmas and lower than previously determined by others (Canil 1999, Roeder & Reynolds, 1991, Toplis & Corgne 2002), and suggest that the V behaviour in kimberlitic melts could be different from that in basaltic, picritic and komatiitic melts although more analyses are required in order to better constrain the change in the $D_V^{Mtc/liq}$ with fO_2 at different T and compositions. The "b" value could possibly reflect the minor scatter in the $D_V^{Mtc/liq}$ values obtained above NNO-2.0. Evidently, further studies on the effect of fO_2 on the V oxidation states in melt are required in order to unravel the discrepancies between the b values. At all fO_2 studied, my equation reproduces 57 % of all experimental data from all compositions (n=12) to within 0.5 log fO_2 unit and 86 % of all experimental data (n=18) to within 1.0 log fO_2 units. Figure 3.8 illustrates the accuracy of the V-in-monticellite oxygen barometer.

Because of the lack of knowledge on the V concentrations in kimberlite liquids, the V-in-monticellite oxygen barometer cannot be applied to natural kimberlites until we find a way to overcome this problem. The vanadium concentrations of the whole rock composition is affected negatively by the large amount of olivine which incorporates little V into its structure and therefore drive the fO_2 determination towards very low values. Further studies are needed in order to either find the primitive kimberlite magma composition or develop another method based on V oxygen barometry in monticellite to be able to quantify the fO_2 of altered rocks such as kimberlites.

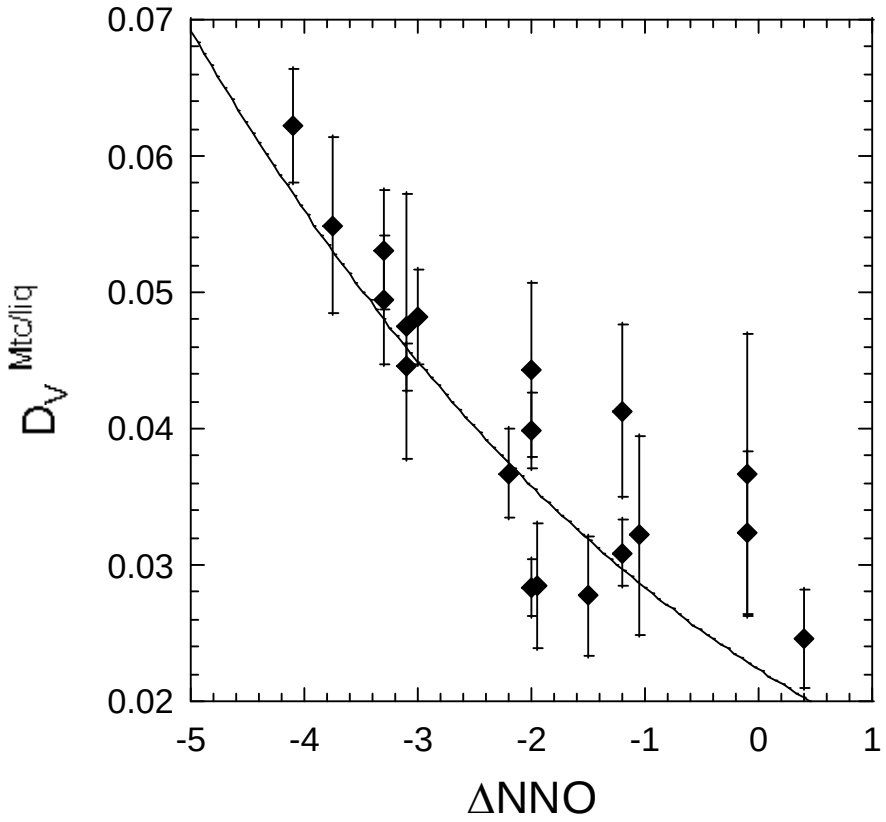

Figure 3.7. Variation of $D_V^{Mtc/liq}$ with fO_2 (expressed relative to the Nickel-Nickel Oxide buffer at the temperature of interest). The correlation between $D_V^{Mtc/liq}$ and fO_2 is fitted by weighted least squares linear regression (equation 7). Regression coefficients c, b and d are respectively 0.354± 1.785, 0.111 ± 0.071 and 1.172 ± 2.302. R^2 is 0.75. Error bars are ± 1σ.

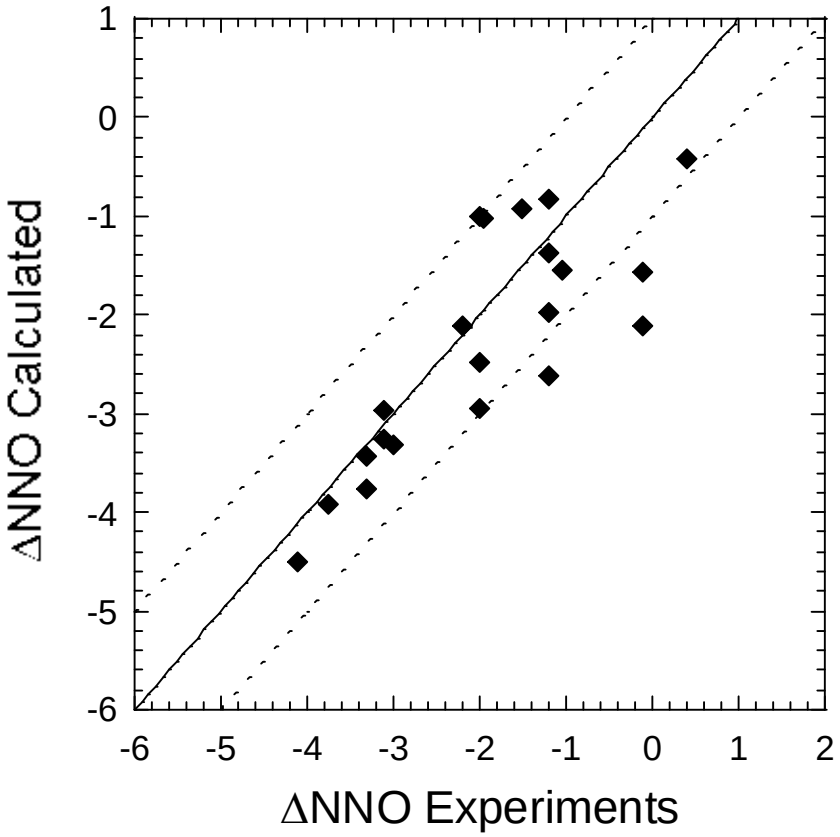

Figure 3.8. fO_2's calculated from the V-in-monticellite oxygen barometer vs fO_2's of experiments (relative to the NNO buffer). Accuracy of the new oxybarometer is ± 1 log fO_2 unit.

Chapter 4
Summary and further work

4.1 Fe-in-monticellite oxybarometer

Because perovskite and oxides in olivine phenocrysts are not always present in a kimberlite pipe, the fO_2 cannot be determined for some kimberlite pipes. This study aimed to calibrate a new oxygen barometer for kimberlite magmas based on the chemistry of monticellite for monticellite-bearing kimberlites in order to permit the evaluation of the quality and the diamond grade of pipe. Experiments were carried out over a temperature range of 120°C from 1230°C to 1350°C and at fO_2 from NNO-4.1 to NNO+5.3. The saturation of kimberlite with monticellite is mainly a function of temperature and bulk composition with a minor effect of fO_2 under high oxidized conditions. I showed that the partitioning of Fe between monticellite and liquid is strongly dependent upon fO_2 (expressed as ΔNNO) and exhibits a minor dependence upon temperature and bulk composition. The monticellite-melt Kd Fe-Mg varies between 0.20 and 0.40 and is clearly dependent upon fO_2 and slightly upon bulk composition. Nonetheless, the monticellite-melt Kd Fe-Mg may be used to calculate the Mg# of the melt in equilibrium with monticellite. The Fe-in-monticellite oxygen barometer was calibrated by weighted least-square regression and reproduces the experimental fO_2 within 1 log fO_2 unit.

4.2 Applications

The application of the Fe-in-monticellite oxygen barometer to natural kimberlites revealed a range of fO_2 from NNO-3.5 to NNO+1.7. The Fe-in-monticellite is only applicable to fresh hypabyssal kimberlites because the alteration of the rock changes the

FeO of the bulk composition affecting significantly the results. The comparison with previous oxygen barometers showed that the Fe-in-monticellite oxygen barometer gives similar fO_2 values to the Fe-in-perovskite (for De Beers, Dutoitspan and Grizzly pipes) but more oxidized values than the Ol-Sp oxygen barometer (Figure 4.1). The discrepancies between the Ol-Sp and Fe-in-monticellite oxygen barometers are due to the assumptions of both oxygen barometers, e.g., $a_{SiO2\ liq}$ and FeO of the liquid, leading to biases in the determination of fO_2 values.

4.3 Kimberlite primitive magma composition

The primitive kimberlite magma composition was previously calculated from a variety of methods, but the extremely high Mg# of the melt obtained from all those methods is at odds with the composition of the mantle, i.e., kimberlite melts would not be in equilibrium with the mantle. The primitive kimberlite magma composition of 16 pipes was calculated from the monticellite composition and the monticellite-melt Kd Fe-Mg determined experimentally, assuming a range of monticellite Kd Fe-Mg between 0.20 and 0.40, and revealed a wide range of Mg# of kimberlite melts from 0.40 to 0.90. Despite the small effect of fO_2 and bulk composition on the monticellite-melt Kd Fe-Mg, the range of Mg# liquid is larger than the uncertainties related to these dependences (±0.1) and reflects the various processes and sources generating kimberlites. The estimates of the kimberlite melts from Lac de Gras and South Africa are in agreement with those by previous workers (e.g., Becker & Le Roex, 2006; Kopylova et al., 2007; Kjarsgaard et al., 2009; Le Roex et al., 2003). The Mg# of the melt may be related to the age of kimberlites and to the diamond grade but further investigations need to be undertaken.

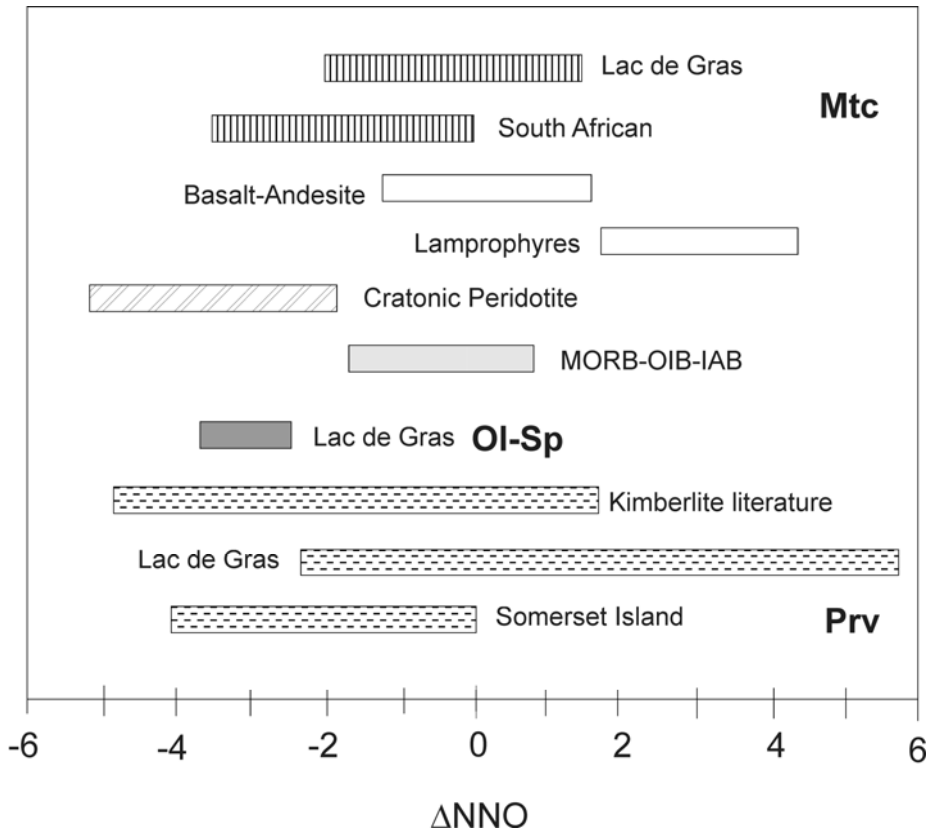

Figure 4.1. Estimates of fO_2 of kimberlites from the Fe-in-Perovskite (Prv), Fe-in-Monticellite (Mtc) and Olivine-Spinel (Ol-Sp) oxygen barometers (Bellis & Canil, 2007; this study; Fedortchouk & Canil, 2004) along with other estimates of MORB's, OIB's, IAB's, lamprophyres, andesites (Carmichael, 1991; Christie et al., 1986; Cottrell & Kelley, 2011; Lee et al., 2003; Mallmann & O'Neill, 2009) and cratonic peridotites (McCammon & Kopylova, 2004; Woodland & Koch, 2003).

4.4 V-in-monticellite oxybarometer

This study aimed also to calibrate a second oxygen barometer based on the vanadium content of monticellite. Vanadium is immobile to subsequent alteration of the rock and this makes the V-in-monticellite oxygen barometer very attractive because of the extensive alteration of kimberlites. The $D_V^{Mtc/liq}$ was found to be strongly dependent upon fO_2 over a fO_2 range from NNO-4.1 to NNO+5.3. The bulk composition and temperature dependencies are minor in comparison to that of fO_2. The estimation of the V^{5+} species in the melt phase at different fO_2's showed that V^{5+} is the dominant species above NNO at all temperatures whereas V^{4+} is dominant above NNO-5 at 1280°C and above NNO-3 at 1350°C. Because of the large amount of V^{5+} in the melt phase above NNO and the assumption of only V^{3+} and V^{4+} in the melt phase, the V-in-monticellite oxygen barometer was calibrated on a smaller fO_2 range from NNO-4.1 to NNO+0.5. The V-in-monticellite oxybarometer reproduces the experimental fO_2 within 1 log fO_2 unit. Unfortunately, its application cannot be done in this study because of the unknown concentrations of V in kimberlite melts. The whole rock composition of kimberlites is biased with respect to V because olivine is the dominant phase and accommodates very little V decreasing the V concentration of the whole rock composition. Either further study on the V content of kimberlite melts must be undertaken or this method to model the V behaviour in kimberlite melt is not appropriate and must be improved.

4.5 Further work

The true nature of kimberlite melts and its evolution throughout its ascent to the surface is not well constrained. The unknown origin of carbonates and serpentine in kimberlites hinders the determination of the origin of H_2O and CO_2. Kimberlites may contain an important amount of primitive volatiles (e.g., H_2O and CO_2), and these may

affect the liquidus temperature and possibly the partitioning of Fe and V into monticellite. The Fe, Fe-Mg and V partitioning between monticellite and liquid were studied under anhydrous conditions and could likely change in other systems such as in carbonate-rich melts as observed for the olivine-melt Kd Fe-Mg partitioning. I propose as further studies to constrain the variation of $D_{Fe}^{Mtc/liq}$, monticellite-melt Kd Fe-Mg and $D_V^{Mtc/liq}$ in systems containing CO_2 (and H_2O) at low pressure (≤ 5 kbars) to better estimate the fO_2 of kimberlites because fO_2 may change during degassing. The likely monticellite-melt Kd Fe-Mg dependence on the volatiles (mostly CO_2) solubility in kimberlitic melts would have a direct impact on the Mg# of the melt calculated from the monticellite composition. Because the Fe^{2+}/Fe^{3+} ratio in the melt was calculated by the Kress & Carmichael's equation (1988), which was calibrated with basalt and andesite compositions, the monticellite-melt Kd Fe^{2+}-Mg might not be accurate. Therefore, I suggest testing the Kress & Carmichael's equation on kimberlite compositions to refine the results and to better constrain the Mg# of the primitive kimberlite melt. Finally, it would be interesting to constrain the effect of fO_2 calculated with the Fe-in-monticellite oxygen barometer on the diamond grade and the resorption features of diamonds for the kimberlite pipes analyzed in this study like Canil & Bellis (2007) and Fedortchouk et al. (2005) did. Regarding the V-in-monticellite oxybarometer, because the determination of the V concentrations of kimberlite melts would be very challenging, verily an impossible task, the V-in-monticellite oxygen barometer needs to be improved by other means (e.g., V/Sc systematics?). This thesis proved that the origin of kimberlite and its fO_2 remain extremely difficult to constrain because of the extensive alteration and the lack of glass of this rock type although this work brought a significant contribution to the primitive kimberlite composition knowledge. I hope this study will encourage discussion and

further refinement of the oxygen barometers developed in this thesis and refinement of the estimates of Mg# of kimberlite melts by better constraining the enigmatic nature of kimberlites.

Bibliography

Akella, J., Satyanarayana Rao, P., McCallister, R.H., Boyd, F.R., Meyer, H.O.A., 1979. Mineralogical studies on the diamondiferous kimberlite of the Wajrakharur Area, Southern India. *In*, Kimberlites, Diatremes, and Diamonds: Their Geology, Petrology, and Geochemistry (*eds.*, F.R. Boyd and H.O.A. Meyer), American Geophysical Union, Washington, D. C., 172-177.

Arima, M., Kozai, Y., 2008. Diamond dissolution rates in kimberlitic melts at 1300–1500°C in the graphite stability field. Abstract. European Journal of Mineralogy, 20, 357–364.

Armstrong, J.P., Wilson, M., Barnett, R.L., Nowicki, T., Kjarsgaard, B.A., 2004. Mineralogy of primary carbonate-bearing hypabyssal kimberlite, Lac de Gras, Slave Province, Northwest Territories, Canada. Lithos, 76, 415-433.

Armstrong, J.T., 1988. Quantitative analysis of silicates and oxide minerals: comparison of Monte Carlo, ZAF and Φ (ρz) procedures. In: D.E. Newbury, Ed., Microbeam Analysis, 239-246.

Armstrong, J.T., 1988. Bence-Albee after 20 years: review of the accuracy of a-factor correction procedures for oxide and silicate minerals. In Newbury D.E., Ed., Microbeam Analysis, 469-476.

Arndt, N.T., Guitreau, M., Boullier, A.-M., Le Roex, A., Tommasi, A., Cordier, P., Sobolev, A., 2010. Olivine, and the origin of kimberlite. Journal of Petrology, 51, 573-602.

Ballhaus, C. Berry, R.F., Green, D.H., 1991. High pressure experimental calibration of the olivine-orthopyroxene-spinel oxygen geobarometer: implications for the oxidation state of the upper mantle. Contributions to Mineralogy and Petrology, 107, 27-40.

Ballhaus, C., 1993 Redox states of lithospheric and asthenospheric upper mantle. Contributions to Mineralogy and Petrology, 114, 331-348.

Batumike, J.M., Griffin, W.L., Belousova, E.A., Pearson, N.J., O'Reilly, S.Y., Shee, S.R., 2008. LAM-ICPMS U-Pb dating of kimberlitic perovskite: Eocene-Oligocene kimberlites

from the Kundelungu Plateau, D.R. Congo. Earth and Planetary Science Letters, 267, 609-619.

Beard, A.D., Downes, H., Hegner, E., Sablukov, S.M., 1998. Mineralogy and geochemistry of Devonian ultramafic minor intrusions of the southern Kola Peninsula, Russia: implications for the petrogenesis of kimberlites and melilites. Contributions to Mineralogy and Petrology, 130, 228-303.

Becker, M., Le Roex, A.P., 2006. Geochemistry of South African On- and – Off craton, Group I and Group II kimberlites: Petrogenesis and Source region evolution. Journal of Petrology, 47, 673-703.

Bellis, A.J., Canil, D., 2007. Ferric Iron in $CaTiO_3$ Perovskite as an oxygen barometer for kimberlitic magmas I: Experimental Calibration. Journal of Petrology, 48, 219-230.

Bennett, V.C., 2003. Compositional Evolution of the Mantle. Treatise on Geochemistry, Vol. 2. Editor: Richard W. Carlson. Executive Editors: Heinrich D. Holland and Karl K. Turekian. pp. 568, 493-519.

Berg, G.W., Carlson, J.A., 1998. The Leslie kimberlite pipe of Lac de Gras, Northwest Territories, Canada: evidence of near surface hypabyssal emplacement. In: Gurney, J. (ed.) Extended Abstracts, 7th International Kimberlite Conference. Cape Town. University of Cape Town, 81-83.

Borisov, A.A., Kadik, A.A., Zharkova, Y.V. & Kalinichenko, N.V., 1987. Effects of oxygen fugacity on the ratio between valency forms of vanadium in magmas. Geochemistry International, 24, 15-20.

Brett, R.C., Russell, J.K., Moss, S., 2009. Origin of olivine in kimberlite: Phenocryst or impostor? Lithos, 112S, 201-212.

Canil, D., Scarfe, C.M., 1990. Phase Relations in Peridotite + CO_2 Systems to 12GPa: Implications for the Origin of Kimberlite and Carbonate Stability in the Earth's Upper Mantle. Journal of Geophysical Research, 95, 15805-15816.

Canil, D., 1997. Vanadium partitioning and the oxidation state of Archean komatiite magmas. Nature, 389, 842-845.

Canil, D., 1999. Vanadium partitioning between orthopyroxene, spinel and silicate melt and the redox states of mantle source regions for primary magmas. Geochimica et Cosmochimica Acta, 63, 557-572.

Canil, D., 2002. Vanadium in peridotites, mantle redox and tectonic environments: Archean to present. Earth and Planetary Science Letters, 195, 75-90.

Canil, D., Bellis, A.J., 2007. Ferric Iron in $CaTiO_3$ Perovskite as an Oxygen Barometer for kimberlite Magmas II: Applications. Journal of Petrology, 48, 231-252.

Canil, D., Bellis, A.J., 2008. Phase equilibria in a volatile-free kimberlite at 0.1 MPa and the search for primary kimberlite magma. Lithos, 105, 111-117.

Canil, D., Fedortchouk, Y., 2000. Clinopyroxene-liquid partitioning for vanadium and the oxygen fugacity during formation of cratonic and oceanic mantle lithosphere. Journal of Geophysical Research, 105, 26003-26016.

Canil, D., Fedortchouk, Y., 2001. Olivine-liquid partitioning of vanadium and other trace elements, with applications to modern and ancient picrites. Canadian Mineralogist, 39, 319-330.

Canil, D., O'Neill, H.S.C., 1996. Distribution of ferric iron in some upper-mantle assemblages. Journal of Petrology, 37, 609-635.

Carmichael, I.S.E., 1991. The redox states of basic and silicic magmas: a reflection of their source regions? Contributions to Mineralogy and Petrology, 106, 129-141.

Carmichael, I.S.E., Ghiorso, M.S., 1986. Oxidation-reduction relations in basic magma: a case for homogeneous equilibria. Earth and Planetary Science Letters, 78, 200-210.

Caro, G., Kopylova, M.G., 2004. The hypabyssal 5034 kimberlite of the Gahcho Kué cluster, Southeastern Salve Craton, Northwest Territories, Canada: A granite-contaminated Group-I kimberlite. Canadian Mineralogist, 42, 183-207.

Cas, R.A.F., Porritt, L., Pittari, A., Hayman, P.C., 2009. A practical guide to terminology for kimberlite facies: A systematic progression from descriptive to genetic, including a pocket guide. Lithos, 112S, 183–190.

Cas, R., Porritt, L., Pittari, A., Hayman, P., 2008a. A new approach to kimberlite facies terminology using a revised general approach to the nomenclature of all volcanic rocks and deposits: Descriptive to genetic. Journal of Volcanology and Geothermal Research, 174, 226–240.

Cas, R.A.F., Hayman, P., Pittari, A., Porritt, L., 2008b. Some major problems with existing models and terminology associated with kimberlite pipes from a volcanological perspective, and some suggestions. Journal of Volcanology and Geothermal Research, 174, 209–225.

Chakhmouradian, A.R., Mitchell, R.H., 2000. Occurrence, alteration patterns and compositional variation of perovskite in kimberlites. Canadian Mineralogist, 38, 975-994.

Chalapathi Rao, N.V., Gibson, S.A., Pyle, D.M., Dickin, A.P., 2004. Petrogenesis of Proterozoic lamproites and kimberlites from the Cuddapah Basin and Dharwar Craton, Southern India. Journal of Petrology, 45, 907-948.

Chalapathi Rao, N.V., Srivastava, R.K., 2009. Petrology and geochemistry of diamandiferous Mesoproterozoic kimberlites from Wajrakarur kimberlite field, Eastern Dharwar craton, southern India: genesis and constraints on mantle source regions. Contributions to Mineralogy and Petrology, 157, 245-265.

Cicconi, M.R., Giuli, G., Paris, E., Ertel-Ingrisch, W., Ulmer, P., Dingwell, D.B., (2010) Europium in silicate glasses at different oxygen fugacity. Geophysical Research Abstracts, Vol. 12, EGU2010-574.

Clement, C.R., 1982. A comparative geological study of some major kimberlite pipes in the Northern Cape and Orange Free State. Ph.D. thesis. University of Cape Town.

Clement, C.R., Skinner, E.M.W., Scott Smith, B.H., 1984. Kimberlite Redefined. Journal of Geology, 92, 223-228.

Christie, D. M., Carmichael, I. S. E. & Langmuir, C. H., 1986. Oxidation states of mid-ocean ridge basalt glasses. Earth and Planetary Science Letters, 79, 397-411.

Cottrell, E., Kelley, K.A., 2011. The oxidation state of Fe in MORB glasses and the oxygen fugacity of the upper mantle. Earth and Planetary Science Letters, 305, 270–282.

Dalton, J.A. and Presnall, D.C., 1998. The continuum of primary carbonatitic-kimberlitic melt compositions in equilibrium with lherzolite: Data from the system CaO-MgO-Al_2O_3-SiO_2-CO_2 at 6 GPa. Journal of Petrology, 39, 1953-1964.

Davis, W.J., Kjarsgaard, B.A., 1997. A Rb-Sr Isochron Age for a Kimberlite from the Recently Discovered Lac de Gras Field, Slave Province, Northwest Canada. The Journal of Geology, 105, 503-510.

Dawson, J.B., Hawthorne, J.B., 1973. Magmatic sedimentation and carbonatitic differentiation in kimberlite sills at Benfontein, South Africa. Journal of the Geological Society of London, 129, 61–85.

Deines, P., Nafziger, R.H., Ulmer, G.C., Woermann, E., 1974. T-fO_2 tables for selected gas mixtures in the C-H-O system. In: College Earth Mineralogy Science Bulletin Exp. Station 88, The Pennsylvania State Univ.

Donnelly, C.L., Griffin, W.L., O'Reilly, S.Y., Pearson, N.J., Shee, S.R., 2011. The Kimberlites and related rocks of the Kuruman Kimberlite Province, Kaapvaal Craton, South Africa, Contributions to Mineralogy and Petrology, 161, 351–371.

Dyar, M., 2003. Ferric iron in SNC meteorites as determined by Mössbauer spectroscopy: Implications for Martian Landers and Martians oxygen fugacity, Meteorites and Planetary Science, 38, 1733-1752.

Edgar, A.D., Charbonneau, H.E., 1993. Melting experiments on a SiO_2-poor, CaO-rich aphanitic kimberlite from 5-10 GPa and their bearing on sources of kimberlite magmas American Mineralogist, 78, 132-142.

Ellis, D.E., Wyllie, P.J., 1979. A model of phase relations in the system MgO-SiO_2-H_2O-CO_2 and prediction of the compositions of liquids coexisting with forsterite and enstatite: *In*, Kimberlites, Diatremes, and Diamonds: Their Geology, Petrology, and Geochemistry

(*eds.*, F.R. Boyd and H.O.A. Meyer), American Geophysical Union, Washington, D. C., 313-318.

Eggler, D.H., Wendlandt, R.F., 1979. Experimental studies on the relationship between kimberlite magmas and partial melting of peridotite. *In*, Kimberlites, Diatremes, and Diamonds: Their Geology, Petrology, and Geochemistry (*eds.*, F.R. Boyd and H.O.A. Meyer), American Geophysical Union, Washington, D. C., 330-338.

Fedortchouk, Y., Canil, D., 2004. Intensive variables in kimberlite Magmas, Lac de Gras, Canada and implications for diamonds survival. Journal of Petrology, 45, 1725-1745.

Fedortchouk, Y., Canil, D., Carlson, J.A., 2005. Dissolution forms in Lac de Gras diamonds and their relationship to the temperature and redox state of kimberlite magma. Contributions to Mineralogy and Petrology, 150, 54-69.

Fedortchouk, Y., Canil, D., 2009. Diamond oxidation at atmospheric pressure: development of surface features and the effect of oxygen fugacity. European Journal of Mineralogy, 21, 623–635.

Fedortchouk, Y., Canil, D., Semenets, E., 2007. Mechanisms of diamond oxidation and their bearing on the fluid composition in kimberlite magmas. American Mineralogist, 92, 1200-1212.

Frost, B.R., 1991. Introduction to oxygen fugacity and its petrologic significance. In: Oxide Minerals: petrologic and magnetic significance (ed Lindsley, D.H.) Mineralogical Society of America, Washington, D.C., 1-10.

Frost, D.J., McCammon, C.A., 2008. The Redox State of Earth's Mantle. Annual Review Earth Planetary Science, 36, 389–420.

Fudali, R.F., 1965. Oxygen fugacities of basaltic and andesitic magmas. Geochimica et Cosmochimica Acta, 29, 1063-1075.

Galimov, E.M., 2005. Redox evolution of the Earth caused by a multi-stage formation of its core. Earth and Planetary Science Letters, 233, 263–276.

Girnis, A.V., Bulatov, V.K., Brey, G.P., 2005. Transition from Kimberlite to Carbonatite Melt under Mantle Parameters: An Experimental Study. Petrology, 13, 1–15.

Gudfinnsson, G.H., Presnall, D.C., 2005. Continuous Gradations among Primary Carbonatitic, Kimberlitic, Melilititic, Basaltic, Picritic, and Komatiitic Melts in Equilibrium with Garnet Lherzolite at 3–8 GPa. Journal of Petrology, 1645-1659. doi:10.1093/petrology/egi029.

Harris, M., Le Roex, A., Class, C., 2004. Geochemistry of the Uintjiesberg kimberlite, South Africa: petrogenesis of an off-craton, group I, kimberlite. Lithos, 74, 149-165.

Harris, J.W., Vance, E.R., 1974. Studies of the Reaction between Diamond and Heated Kimberlite. Contributions to Mineralogy and Petrology, 47, 237-244.

Heaman, L.M., Kjarsgaard, B.A., Creaser, R.A., 2003. The timing of kimberlite magmatism in North America: implications for global kimberlite genesis and diamond exploration. Lithos, 71, 153– 184.

Höfer, H.E., Lazarov, M., Brey,G.P., Woodland, A.B., 2009. Oxygen fugacity of the metasomatizing melt in a polymict peridotite from Kimberley. Lithos, 112S, 1150–1154.

Kamenetsky, V.S., Kamenetsky, M.B., Weiss, Y., Navon, O., Nielsen, T.F.D., Mernagh, T.P., 2009. How unique is the Udachnaya-East kimberlite? Comparison with kimberlites from the Slave Craton (Canada) and SW Greenland. Lithos, 112S, 334–346.

Kavanagh, J.L., Sparks, R.S.J., 2009. Temperature changes in ascending kimberlite magma. Earth and Planetary Science Letters, 286, 404–413.

Kennedy, G.C., 1948. Equilibrium between volatiles and iron oxides in igneous rocks. American Journal of Science, 110, 529-549.

Kilinc, A., Carmichael, I.S.E., Rivers, M.L., Sack, R.O., 1983. The Ferric-Ferrous ratio of natural silicate liquids equilibrated in air. Contributions to Mineralogy and Petrology 83, 136-140.

Kjarsgaard, B.A., 2007. Kimberlite diamond deposits, in Goodfellow, W.D., ed., Mineral Deposits of Canada: A Synthesis of Major Deposit Types, District Metallogeny, the Evolution of Geological Provinces, and Exploration Methods: Geological Association of Canada, Mineral Deposits Division, Special Publication, 5, 245-272.

Kjarsgaard, B.A., Pearson, D.G., Tappe, S., Nowell, G.M., Dowall, D.P., 2009. Geochemistry of hypabyssal kimberlites from Lac de Gras, Canada: Comparisons to a global database and applications to the parent magma problem. Lithos, 112S, 236-248.

Kopylova, M.G., Matveev, S., Raudsepp, M., 2007. Searching for the parental kimberlite melt. Geochimica et Cosmochimica Acta, 71, 3616-3629.

Kozai, Y., Arima, M., 2005. Experimental study on diamond dissolution in kimberlitic and lamproitic melts at 1300-1420 °C and 1 GPa with controlled oxygen partial pressure. Abstract. American Mineralogist, 90, 1759-1766.

Kress, V.C., Carmichael, I.S.E., 1988. Stoichiometry of the iron oxidation reaction in silicates melts. American Mineralogist, 73, 1267-1274.

Kurszlaukis, S., Lorenz, V., 2008. Formation of "Tuffisitic Kimberlites" by phreatomagmatic processes. Journal of Volcanology and Geothermal Research, 174, 68–80.

Lee, C.T.A., Brandon, A.D. & Norman, M., 2003. Vanadium in peridotites as a proxy for paleo-fO_2 during partial melting: Prospects, limitations, and implications. Geochimica et Cosmochimica Acta, 67, 3045-3064.

Lee, C.T.A., Leeman, W.P., Canil, D. & Li, Z.X.A., 2005. Similar V/Sc Systematics in MORB and Arc Basalts: Implications for the oxygen fugacities of their mantle source regions. Journal of Petrology, 46, 2313-2336.

Le Roex, A.P., Bell, D.R., Davis, P., 2003. Petrogenesis of Group 1 Kimberlites from Kimberley, South Africa: Evidence from Bulk-rock Geochemistry. Journal of Petrology, 44, 2261-2286.

Lorenz, V., 1975. Formation of phreatomagmatic maar-diatreme volcanoes and its relevance to kimberlite diatremes. Physics and Chemistry of The Earth, 9, 17-27.

Mallmann, G. & O'Neill, H.S.C., 2009. The crystal/Melt partitioning of V during mantle melting as a function of oxygen fugacity compared with some other elements (Al, P, Ca, Sc, Ti, Cr, Fe, Ga, Y, Zr and Nb). Journal of Petrology, 50, 1765-1794.

Mattioli, G.S, Baker, M.B., Rutter, M.J., Stolper, E.M., 1989. Upper Mantle Oxygen Fugacity and Its Relationship to Metasomatism. The Journal of Geology, 97, 521-536.

McCammon, C.A., Frost, D.J., Smyth, J.R., Laustsen, H.M.S., Kawamoto, T., Ross, N.L., van Aken, P.A., 2004. Oxidation state of iron in hydrous mantle phases: implications for subduction and mantle oxygen fugacity. Physics of the Earth and Planetary Interiors, 143–144, 157–169.

McCammon, C., Kopylova, M.G., 2004. A redox profile of the Slave mantle and oxygen fugacity control in the cratonic mantle. Contributions to Mineralogy and Petrology, 148, 55–68.

Mitchell, R.H., 2008. Petrology of hypabyssal kimberlites: Relevance to primary magma compositions. Journal of Volcanology and Geothermal Research 174, 1–8.

Mitchell, R.H., 1986. Kimberlites: Mineralogy, Geochemistry, and Petrology. Plenum Press, New York and London.

Mitchell, R.H., 1978. Mineralogy of the Elwin Bay kimberlite, Somerset Island, N.W.T., Canada. American Mineralogist, 63, 47-57.

Nielsen, T.F.D., Sand, K.K., 2008. The Majuagaa kimberlite dyke, Maniitsoq, region, West Greenland: constraints on a Mg-rich silicocarbonatitic melt composition from groundmass mineralogy and bulk compositions. Canadian Mineralogist, 46, 1043–1061.

Nowicki, T., Porritt, L., Crawford, B., Kjarsgaard, B., 2008. Geochemical trends in kimberlites of the Ekati property, Northwest Territories, Canada: Insights on volcanic and resedimentation processes. Journal of Volcanology and Geothermal Research, 174, 117-127.

Nowicki, T., Galloway, M., Le Roex, A., Gurney, J., Smith, C., Canil, D., 2009. Iron-in-perovskite oxygen barometry and diamond resorption in kimberlites and lamproites from

southern Africa, Russia and Australia. Poster. 9th International Kimberlite Conference. Frankfurt, Germany, 2008.

O'Neill, H.S.C., Wall, V.J.,1987. The Olivine-Orthopyroxene-Spinel Oxygen Geobarometer, the Nickel Precipitation Curve, and the Oxygen Fugacity of the Earth's Upper Mantle. Journal of Petrology, 28, 1169-1191.

Osborn, E.F., 1959. Role of oxygen pressure in the crystallization and differentiation of basaltic magmas. American Journal of Science, 257, 609-647.

Osborn, E.F., Roeder, P.L., 1960. Effect of oxygen pressure on crystallization in simplified basalt systems: Internat. Geol. Cong., 21st Copenhagen, Proc., sec. 13, pt. 13, 147-155.

Osborn, E.F., 1962. Reaction series for subalkaline igneous rocks based on different oxygen pressure conditions, American Mineralogist, 47, 211-266.

Parkinson, I.J., Arculus, R.J., 1999. The redox state of subduction zones: insights from arc-peridotites. Chemical Geology, 160, 409–423.

Paton, C., Hergt, J.M., Woodhead, J.D., Phillips, D., Shee, S.R., 2009. Identifying the asthenospheric component of kimberlite magmas from the Dharwar Craton, India. Lithos, 112S, 296–310.

Patterson, M., Francis, D., McCandless, T., 2009. Kimberlites: Magmas or mixtures? Lithos, 112S, 191-200.

Pieters, C.M., Klima, R.L., Hiroi, T., Dyar, M.D., Lane, M.D., Treiman, A.H., Noble, S.K., Sunshine, J.M., Bishop, J.L., 2008. Martian dunite NWA 2737: Integrated spectroscopic analyses of brown olivine. Journal of Geophysical Research, 113, E06004.

Pouchou, J.L., Pichoir, F., 1985. PAP $\phi(\rho Z)$ procedure for improved quantitative microanalysis. Microbeam Analysis, 104-106.

Price, S.E., Russell, J.K., Kopylova, M.D., 2000. Primitive Magma from the Jericho Pipe, N.W.T., Canada: Constraints on primary kimberlite melt chemistry. Journal of Petrology, 41, 789-808.

Roeder, P.L., Emslie, R.F., 1970. Olivine-liquid equilibrium. Contributions to Mineralogy and Petrology, 29, 275-289.

Roeder, P.L., Reynolds, I., 1991. Crystallization of Chromite and Chromium solubility in Basaltic melts. Journal of Petrology, 32, 909-934.

Sack, R.O., Carmichael, I.S.E., Rivers, M., Ghiorso, M.S., 1980. Ferric-Ferrous Equilibria in Natural Silicate Liquids at 1 bar. Contributions to Mineralogy and Petrology, 75, 369-376.

Scott Smith, B.H.,Nowicki, T.E., Russell, J.K., Webb, K.J., Hetman, C.M., Harder, M., Mitchell, R.H., 2008. Kimberlites: Descriptive Geological Nomenclature and Classification. 9th International Kimberlite Conference, Extended Abstract, No. 9IKC-A-00124.

Seifert, F., Czank, M., Simons, B., Schmahl, W., 1987. A commensurate-Incommensurate phase transition in iron-bearing åkermanites. Physics and Chemistry of Minerals, 14, 26-35.

Skinner, E.M.W., Marsh, J.S., 2004. Distinct kimberlite pipe classes with contrasting eruption processes. Lithos, 76, 183–200.

Sonin, V.M., Zhimulev, E.I., Fedorov, I.I., Chepurov, A.I., 2006. Effect of Oxygen Fugacity on the Etching Rate of Diamond Crystals in Silicate Melt. Geology of Ore Deposits, 48, 499–501.

Sparks, R.S.J., Baker, L., Brown, R.J., Field, M., Schumacher, J., Stripp, G., Walters, A., 2006. Dynamical constraints on kimberlite volcanism. Journal of Volcanology and Geothermal Research, 155, 18–48.

Sparks, R.S.J., Brooker, R.A., Field, M., Kavanagh, J., Schumacher, J.C., Walter, M.J., White, J., 2009. The nature of erupting kimberlite melts. Lithos, 112S, 429-438.

Stachel, T., Harris, J.W., 2008. The origin of cratonic diamonds — Constraints from mineral inclusions. Ore Geology Reviews, 34, 5–32.

Sutton, S.R., Karner, J., Papike, J., Delaney, J.S., Shearer, C., Newville, M., Eng, P., Rivers, M. & Dyar, M.D., 2005. Vanadium K edge Xanes of synthetic and natural basaltic glasses and application to microscale oxygen barometry. Geochimica et Cosmochimica Acta, 69, 2333-2348.

Toplis, M.J., Carroll, M.R., 1995. An experimental Study of the Influence of oxygen fugacity on Fe-Ti Oxide Stability, phase relations, and Mineral-melt equilibria in Ferro-basaltic Systems. Journal of Petrology, 36, 1137-1170.

Toplis, M.J. & Corgne, A., 2002. An experimental study of element partitioning between magnetite, clinopyroxene and iron-bearing silicate liquids with particular emphasis on vanadium. Contributions to Mineralogy and Petrology, 144, 22-37.

Treiman, A.H., Dyar, M.D., McCanta, M., Noble, S.K., Pieters, C.M., 2007. Martian dunite NWA 2737: Petrographic constraints on geological history, shock events, and olivine color. Journal of Geophysical Research, 112, E04002.

Warner R.D., Luth, W.C., 1973. Two-Phase Data for the Join Monticellite ($CaMgSiO_4$)-Forsterite (Mg_2SiO_4): Experimental results and Numerical Analysis. American Mineralogist, 58, 998-1008.

Wiedenmann, D., Zaitsev, A.N., Britvin, S.N., Krivovichev, S.V., Keller, J., 2009. Alumoåkermanite, $(Ca,Na)_2(Al,Mg,Fe^{2+})(Si_2O_7)$, a new mineral from the active carbonatite-nephelinite-phonolite volcano Oldoinyo Lengai, northern Tanzania. Mineralogical Magazine, 73, 373-384.

Wood, B.J., 1990. An Experimental test of the Spinel peridotite oxygen barometer. Journal of Geophysical Research, 95, B10, 15845-15851.

Wood, B.J., Wade J., Kilburn, M.R., 2009. Core formation and the oxidation state of the Earth: Additional constraints from Nb, V and Cr partitioning. Geochimica et Cosmochimica Acta, 72, 1415–1426.

Woodland, A.B., Koch, M., 2003. Variation in oxygen fugacity with depth in the upper mantle beneath the Kaapvaal craton, Southern Africa. Earth and Planetary Science Letters, 214, 295-310.

Wu, F.Y., Yang, Y.-H., Mitchell, R.H., Li ,Q.-L., Yang, J.-H., Zhang ,Y.-B., 2010. In situ U-Pb age determination and Nd isotopic analysis of perovskites from kimberlites in southern Africa and Somerset Island, Canada. Lithos, 115, 205-222.

Zhang, R.Y., Shu, J.F., Mao, H.K., Liou, J.G., 1999. Magnetite lamellae in olivine and clinohumite from Dabie UHP ultramafic rocks, central China. American Mineralogist, 84, 564-569.

Zurevinski, S.E., 2009. The origin and evolution of North American kimberlites. Ph.D. Thesis. University of Alberta.

Zurevinski, S.E., Mitchell, R.H., 2011. Highly evolved hypabyssal kimberlite sills from Wemindji, Quebec, Canada: insights into the process of flow differentiation in kimberlite